CONTROLLING ACOUSTIC AND ELASTIC WAVES WITH METAMATERIALS: DESIGN ELEMENTS AND THEIR APPLICATIONS

By

XIAOSHI SU

A dissertation submitted to the

Graduate School—New Brunswick

Rutgers, The State University of New Jersey

in partial fulfillment of the requirements

for the degree of

Doctor of Philosophy

Graduate Program in Mechanical and Aerospace Engineering

written under the direction of

Professor Andrew N. Norris

and approved by

_____

_____

_____

_____

New Brunswick, New Jersey

May, 2017

ABSTRACT OF THE DISSERTATION

Controlling Acoustic and Elastic Waves with Metamaterials: Design Elements and Their Applications

By XIAOSHI SU

Dissertation Director:

Professor Andrew N. Norris

The purpose of this dissertation is to model, simulate and design metamaterials for underwater sound and elastic wave control. Water-based acoustic metamaterials usually suffer from low transmission due to the impedance mismatch with water; elastic metamaterials also suffer from this issue not only because of the impedance mismatch to the host medium, but also due to the multiple wave types existing simultaneously at the interface between the inclusions and the background matrix. This dissertation focuses on the theoretical modeling and computational design of broadband high transmission metamaterial devices.

Several related topics are discussed. (1) A semi-analytical method for band diagram computation of three dimensional (3D) lattices is developed in this dissertation. It has significant applications in 3D pentamode metamaterial design. (2) Acoustic transmission through gratings of parallel plates displaying anisotropic inertia is also investigated. It is found that broadband impedance matching and total acoustic transmission can be achieved if the plane wave is incident at the so-called intromission angle $\pm\theta_i$. (3) Elastic wave transmission through aligned parallel plates are studied theoretically by considering the coupling between different types of waves in elastic half-spaces and in the plates. The results are applied in the design and optimization of elastic metamaterials. (4) Elastic waves in

fluid-saturated anisotropic double porosity medium of cubic symmetry is also investigated as an extension to Biot's theory of poroelasticity. A third dilatational wave is predicted in a double porosity fluid-saturated gyroid structure and demonstrated using finite element (FEM) simulations.

The second part of the dissertation focuses on several novel devices for manipulating acoustic and elastic waves. Metallic metamaterial unit cells of the hexagonal lattice type are employed to mimic the *quasi-static* acoustic properties of water, and to provide a certain range of index for gradient index (GRIN) metamaterial design. The advantage of such a metamaterial element is that it has in-plane isotropy and only allows one propagating mode within the frequency range of interest. (5) A flat GRIN lens is designed by tuning the unit cells to obey a modified hyperbolic secant index profile, such that a normally incident plane wave transmits through the lens efficiently and focuses at a single point. The side lobe suppression and aberration reduction abilities of the GRIN lens are demonstrated in both simulations and in underwater experiments (carried out by colleagues at the University of Texas at Austin). (6) An elastic shell based metamaterial element, which provides a wider range of index at the *quasi-static* regime, is adopted in the design of a conformal lens for converting a monopole source to highly directional plane wave beams. The required bulk modulus and density distributions are derived using conformal transformation acoustics mapping from a unit circle to a triangle. The mapping function is adjustable which allows energy radiating preferentially into different directions. Two collimation devices are designed using fluid-saturated shells and demonstrated using full wave FEM simulations. (7) A novel class of elastic metamaterial composed of "effective plates" are introduced to design high transmission devices for elastic waves. Several devices for focusing SV-wave, splitting P- and SV-waves, and asymmetric transmission are designed and demonstrated using full wave FEM simulations.

Acknowledgments

Throughout the past a few years as a Ph.D. student, I have received tremendous help from my advisor, mentors, colleagues, collaborators and friends. I would like to acknowledge with deep gratitude, the extraordinary effort and support of people without whom this dissertation work would not have been accomplished.

First and foremost, I would like to gratefully thank my advisor, Dr. Andrew Norris, for his extraordinary guidance and expertise. He taught me the knowledge of wave propagation, static/dynamic homogenization, the concepts of metamaterials as well as their design approaches. He always has the patience to discuss about new scientific discoveries and help me overcome the issues I had in my research. I am sincerely indebted to him for his encouragement and support. This dissertation contains most of the results in our previously published work Refs. [1, 2] and accepted paper Ref. [3] as well as several other pending publications.

I would also like to thank my dissertation committee members, Dr. William Bottega, Dr. Liping Liu and Dr. Alexey Titovich, for reviewing this manuscript. I took courses on Mechanics of Materials with Dr. Bottega and Dynamics of Solids and Structures with Dr. Liu. I benefited a lot from these courses and still use the basic knowledge I learned from them everyday in my research. I would also thank all my instructors at Rutgers, I would not have become the researcher I am today if it was not for them.

The efforts by our collaborators should also be acknowledged. Dr. Michael Haberman and Dr. Preston Wilson, as well as their student Colby Cushing, from University of Texas at Austin conducted the underwater test to demonstrate the gradient index lens presented in this dissertation. This work has been improved a lot through the communications before and during the test.

I would also sincerely thank everyone who was a member in our research group at

Rutgers. Dr. Feruza Amirkulova, Dr. Adam Nagy and Dr. Alexey Titovich have always been helpful to me. They always generously share the new findings with me, and teach me the knowledge that I could never learn elsewhere. Dr. Alfonso Climente from Polytechnic University of Valencia, who visited our group for three months, also shared a lot with me, especially his knowledge in phononics and techniques in COMSOL simulations.

Also, I want to thank all of the people who bring together a group of excellent faculties and students to the Physical Acoustics Summer School (PASS) in Heber City, Utah. The PASS was a special experience, I met and had discussions with people whose names I have seen many times in textbooks and classical papers.

I am eternally grateful to my undergraduate advisor, Dr. Dishan Huang, from Shanghai University, who brought me into the field of wave propagation when I was a junior student. To this day he is still helping and encouraging me to become a better scholar in this research area. I would also thank my friend Rui Cao, who is now a Ph.D. student working on noise control of road-tire interaction at Purdue University, for his willingness to share his knowledge in acoustics with me. He is always available to give me a hand when a I need his help.

Thanks to Prof. Sarbani Vengadasalam from the Graduate Writing Program of Rutgers University for providing course on dissertation writing. Her suggestions on the organization of the dissertation are very helpful.

I would also like to gratefully thank my friends Yanjun Wang, Xiao Lin, Nawei Sun and Wenke Liu. Many thanks to everyone not mentioned for your help.

Last but importantly, this work was supported by Office of Naval Research through MURI Grant NO. N00014-13-1-0631.

Dedication

I dedicate my dissertation work to my parents Jiugeng Su and Jinfang Xia.

I also dedicate my accomplishments to my uncle Yingfei Xia, aunt Yan Jiang, and cousins Mark Xia and Maggie Xia.

Special dedication to my grandparents...

Table of Contents

Abstract ii

Acknowledgments iv

Dedication vi

List of Tables xii

List of Figures xiii

1. Introduction 1

1.1. Brief introduction to metamaterials 1

1.2. Motivation and current objectives 2

1.2.1. Acoustic metamaterials 2

1.2.2. Elastic metamaterials 3

1.3. Outline of the Dissertation accomplishments 3

2. Wave propagation and homogenization in 3D lattices 5

2.1. Description of the problem 6

2.1.1. Description of the structures and parameters 6

2.1.2. Definition of the coordinate system 7

2.2. Dynamic stiffness matrices 8

2.2.1. Solution of the longitudinal wave equation 8

2.2.2. Solution to the flexural wave equation 9

2.2.3. The flexural wave equation and BCs on the rod. 10

Bending in y-direction 10

Bending in z-direction 11
2.2.4. Total force and dynamic stiffness 12
2.3. Analytical dispersion relations 13
2.3.1. Total force and Bloch-Floquet periodic conditions 13
2.3.2. Dispersion relations 13
2.4. Cubic lattice 14
2.4.1. Dispersion relations 14
2.4.2. Numerical Example 17
2.5. Tetrahedral Lattice 19
2.5.1. Dispersion relations 19
2.5.2. Numerical Example 19
2.6. Dynamic homogenization of cubic lattice 23
2.6.1. Wave speeds in anisotropic medium of cubic symmetry 23
Wave propagation in (100) direction. 24
Wave propagation in (110) direction. 24
2.6.2. Dynamic derivation of effective moduli of cubic lattice 25
Wave propagation in (100) direction. 26
Wave propagation in (110) direction. 27
Effective bulk modulus 28
2.6.3. Designing metal water using cubic lattice 29
2.7. Discussion 30

3. Extraordinary acoustic transmission through slanted gratings 31
3.1. Governing equations 32
3.2. Solution for an anisotropic inertial slab 33
3.2.1. Extraordinary acoustic transmission 34
3.3. Single-layer gratings as anisotropic inertial slabs 35
3.3.1. Rigid grating elements 37
3.3.2. Transmission at normal incidence: $\theta_i = 0$ 37

3.3.3. Zigzag structures 38
3.4. Numerical examples and discussion 39
3.4.1. Transmission and reflection through rigid grating elements 39
3.4.2. Full wave simulations of zigzag grating elements 39
3.4.3. Transient simulation of steel plates as grating elements in water . . . 41
3.5. Discussion 43

4. Broadband pentamode gradient index lens for underwater sound 44
4.1. Index gradient 46
4.1.1. Focal distance 46
4.1.2. Hyperbolic secant profile 47
4.1.3. Quadratic profile 48
4.1.4. Reduced aberration profile 48
4.2. Design of unit cells 49
4.3. Simulation results 51
4.4. Discussion 56

5. Directional cylindrical-to-plane wave lens for underwater acoustics . . 57
5.1. Transformation acoustics mapping 59
5.2. Directional collimation 60
5.2.1. Impedance matching condition and far-field behavior 60
5.2.2. Directional collimation using effective medium 62
5.3. Cylindrical-to-plane wave lenses using elastic shells 64
5.3.1. Unit cell design 64
5.3.2. Cylindrical-to-plane wave lens ($\phi = \pi/3$) 66
5.3.3. Bend more energy into one direction ($\phi = \pi/2$) 67
5.4. Discussion 68

6. Bulk elastic wave control using metamaterials with aligned parallel plates 70
6.1. Transmission and reflection at normal incidence 71

6.1.1. Governing equations 71
6.1.2. Transmission and reflection of a normally incident P-wave 73
6.1.3. Transmission and reflection of a normally incident SV-wave 74
6.1.4. Discussion and improved solution for SV-wave 77
6.2. Metamaterial for asymmetric transmission of elastic waves 80
6.2.1. Mode conversion at free boundary 80
6.2.2. Simulation of the asymmetric transsmison 81
6.3. Elastic GRIN lens for focusing SV-wave 82
6.3.1. Diffraction and Huygens-Fresnel principle 82
6.3.2. Simulation of the focusing effect 84
6.4. Elastic prism for splitting SV- and P-waves 84
6.4.1. Wave speeds and refractive index 84
6.4.2. Simulation of the steering effect 87
6.5. Discussion 88

7. Anomalous refraction and asymmetric transmission of SV-wave through elastic metasurfaces 90
7.1. Phase modulation by thickness variation of plates 91
7.1.1. Dispersion relation 91
7.1.2. Phase modulation 92
7.2. Split SV- and P-waves using an elastic metasurface 94
7.3. Asymmetric transmission of SV-wave through elastic metasurfaces 97
7.4. Discussion 98

8. Elastic waves in fluid-saturated cubic double porosity medium 101
8.1. Wave propagation in cubic double porosity media 102
8.1.1. Constitutive relations of the solid-fluid aggregate 102
8.1.2. Dynamic equations of the solid-fluid aggregate 103
8.1.3. Wave equations and speeds 104
8.2. Isotropic single porosity 106

8.2.1. Elastic constants and densities 106
8.2.2. Biot wave speeds 108
8.3. Wave speeds in fluid-saturated gyroid structures 108
8.3.1. Effective properties of the empty gyroid structure 108
8.3.2. Wave speeds in gyroid structure filled by single fluid 111
8.3.3. Wave speeds in gyroid structure filled by two fluids 112
8.4. Discussion 114

9. Concluding remarks 115
9.1. Conclusions on the original contributions 115
9.2. Current and future work 116

Appendix A. Coordinate transformation for cubic lattice 118

Appendix B. Unit circle to triangle mapping 121

References 122

List of Tables

4.1. Geometry of the unit cells. Each type of unit cell corresponds to different values of effective refractive indices as shown in Fig. 4.3(b). 50

5.1. Selected materials for elastic shells. The values h/a are for matching effective density to water. 66

5.2. Selected elastic shells for the GRIN lens ($\phi = \pi/3$). The labels correspond to the numbering in Fig. 5.5. 67

List of Figures

2.1. Geometry of lattices structures. (a) Cubic lattice and (b) diamond lattice. . 7

2.2. Coordinate system transformation 8

2.3. Bending components one each beam/rod. (a) Deflection in $y-$direction and (b) deflection in $z-$direction. 11

2.4. Cubic lattice. (a) The unit cell of a cubic lattice which has six mass points connected to the center mass through beam/rod members. (b) The Irreducible Brillouin Zone. 15

2.5. Dispersion curves of a cubic lattice comprised of square beams ($t = 12.5$ mm). (a) Computed using the semi-analytical method developed in this chapter; (b) computed using COMSOL Multiphysics. The blue lines in (a) are dispersion curves of longitudial wave, the black and red lines are dispersion curves of shear wave, and the green lines indicate represent the flexural resonances of the beams oriented in $y-$ and $z-$directions (deflection in $x-$direction). . . . 18

2.6. Dispersion curve of a cubic lattice comprised of circular rods ($r = 6$ mm). (a) Computed using the semi-analytical method developed in this chapter; (b) computed using COMSOL Multiphysics. The blue lines in (a) are dispersion curves of longitudial wave, the black and red lines are dispersion curves of shear wave, and the green lines indicate represent the flexural resonances of the beams oriented in $y-$ and $z-$directions (deflection in $x-$direction). . . . 20

2.7. Tetrahedral (diamond) lattice. (a) The unit cell of a diamond lattice which has six mass points connected to two center masses through beam/rod members. (b) The Irreducible Brillouin Zone. 21

2.8. Dispersion curves of a diamond lattice comprised of circular rods ($r = 0.5$ mm). (a) Computed using the semi-analytical method developed in this chapter; (b) computed using COMSOL Multiphysics. 22

2.9. Effective bulk modulus versus α. The horizontal solid line represents the bulk modulus of water. 29

3.1. Equivalent homogeneous slab with anisotropic density. 33

3.2. The obliquely aligned single-layer grating. 36

3.3. Zigzag structures comprised of SLGs in series with alternating orientations $\pm\phi$. 38

3.4. Transmission spectrum at frequency $kd = 0.25$ for rigid SLGs with elements oriented at $\phi = 0°$, $30°$ and $60°$. The solid and dashed curves represent $|T|^2$ and $|R|^2$, respectively. 40

3.5. Total pressure plots for zigzag plastic gratings oriented at $\phi = \pm 30°$. The incident angle is taken to be the intromission angle $\theta_i = \cos^{-1}(1 - f)$, where $f = 0.5$. Frequency $kd = 0.5$ for (a) and (c), $kd = 0.25$ for (b) and (d). . . . 41

3.6. Total pressure plots for steel gratings oriented at $\phi = 30°$. The incident angle is taken to be the intromission angle $\theta_i = \cos^{-1}(1 - f)$, where $f = 0.5$. The frequency is $kd = 0.25$. Each plot corresponds to different time frame: (a) $t = 0$, (b) $t = 0.288$ ms, (c) $t = 0.552$ ms and (d) $t = 0.840$ ms. 42

4.1. Schematic view of the GRIN lens. The left part shows that two ray paths incident at symmetric positions intersect at the focal point beyond the lens. The right part shows the index distribution across the lens. 47

4.2. Comparison between the ray trajectories. (a) Strong aberration using the hyperbolic secant profile, (b) Minimized aberration using the modified secant profile. 49

4.3. Layered design. (a) The top view of the lens, (b) the index distribution and discretized indices of the lens, (c) unit cell of the lens and (d) geometric parameters of the unit cell. 50

4.4. Band diagram of the unit cell at the center ($n_{\text{eff}} = 1$). (a) shows the band structure along the $\Gamma - M - K$ path of the first Brillouin zone, (b) shows the lattice structure where $\vec{a}$ and $\vec{b}$ are the basis vectors in the real space, (c) shows the first Brillouin zone of the lattice structure where $\vec{a}^*$ and $\vec{b}^*$ are the basis vectors in the reciprocal space. 51

4.5. Full wave frequency domain simulation results at (a) 10 kHz, (b) 15 kHz, (c) 20 kHz, (d) 25 kHz, (e) 30 kHz and (f) 35 kHz. 52

4.6. Sound pressure level gain (SPL) at 35 kHz. (a) Colormap over the focal plane, (b) SPL across the focal point along the lens face. 53

4.7. Normalized intensity magnitude across the focal point along the lens face at (a) 30 kHz and (b) 35 kHz. 53

4.8. Full wave time domain simulation of normally incident plane wave at 30 kHz. The plots show the pressure variations at each time frame: (a) 0 ms, (b) 0.12 ms, (c) 0.24 ms, (d) 0.36 ms, (e) 0.48 ms and (f) 0.60 ms. 54

4.9. Full wave time domain simulation of a cylindrical source at 30 kHz. The plots show the pressure variations at each time frame: (a) 0 ms, (b) 0.084 ms, (c) 0.168 ms, (d) 0.252 ms, (e) 0.336 ms and (f) 0.420 ms. 55

5.1. Conformal mapping from a circular domain to a triangular domain. 59

5.2. Comparison of far-field radiation behavior for $\phi = \pi/3$ and different values of a where (a) $a = 2.8044$ with impedance matched at the middle of AB face, and (b) $a = 1.2092$ for unchanged perimeter. 61

5.3. $\sqrt{K'/K}$ and ray paths for unchanged area for (a) and (d) $\phi = \pi/3$, (b) and (e) $\phi = \pi/2$, (c) and (f) $\phi = 2\pi/3$. The origins are located at $t = 0$, 0.2351 and 0.4315 in the transformed coordinates, respectively. 62

5.4. Simulated intensity at 3 kHz where (a) $\phi = \pi/3$, (b) $\phi = \pi/2$ and (c) $\phi = 2\pi/3$. 63

5.5. Discretization of the transformed domain ($\phi = \pi/3$). 64

5.6. Effective properties normalized to water for shells using different materials. Each curve represents the effective properties as a function of the ratio h/a from small to large. 65

5.7. Simulated pressure at (a) 12.5 kHz, (b) 15 kHz and (c) 17.5 kHz. 67

5.8. Simulated pressure at 10.5 kHz. 68

6.1. Two-dimensional schematic of aligned parallel gaps. (a) P- and SV-waves transmit through aligned parallel plates. The black arrows represent the direction of propagation, the red arrows represent the direction of particle motion. (b) The geometric parameters and multiple wave types on the plates. 72

6.2. Transmission and reflection spectrum for a normally incident P-wave. The blue line indicates the energy transmission coefficient, the black line indicates the energy reflection coefficients. 75

6.3. Transmission and reflection spectrum for a normally incident SV-wave. The blue line indicates the energy transmission coefficient, the black line indicates the energy reflection coefficients. 77

6.4. Comparison of the analytical solution (solid line) and full FEM simulation results (dashed line) for incident (a) SV-wave and (b) P-wave. 78

6.5. Comparison of the improved analytical solution (solid line) and simulation results (dashed line). 79

6.6. Asymmetric transmission. The horizontal black line represents the free boundary of a half-space, the rectangular white slits represent gaps, lines with arrow indicate the propagation direction. 80

6.7. Amplitude ratio between incident and reflected P-wave of different materials, from Eq. (6.15). 81

6.8. Mode conversion of P-wave at free boundary (bottom of the simulation domain) in brick without slits/gaps. (a) P-wave incidence from left side at non-critical angle $\theta_0 = 70°$. (b) P-wave incidence from left side at critical angle $\theta_0 = \theta_P$ $(= 43.5°)$. 82

6.9. Asymmetric transmission effect at $f = 21.6$ kHz. (a) P-wave incident from the left side with $\theta_0 = \theta_P$ $(= 43.5°)$. (b) SV-wave incident from the right side with $\theta_0 = \theta_S$ $(= 26.9°)$. 83

6.10. GRIN lens of a solid with parallel gaps. (a) Ray pathes showing the focusing effect. (b) Relations of the geometric parameters. 84
6.11. Focusing of SV-wave by GRIN lens with $\beta = -0.048$ at (a) 20 kHz, (b) 30 kHz, (c) 40 kHz and (b) 50 kHz. 85
6.12. Refraction of elastic waves. (a) Propagation directions of P- and SV- waves through the prism. The black arrows indicate the propagation direction, the red arrows indicate the direction of particle motion. (b) Incident and refracted angles. 86
6.13. Diffraction and refraction of (a) SV- and (b) P-waves. 87
6.14. Zero SV-wave refraction at (a) 10 kHz and (b) 20 kHz. 88
6.15. Positive P-wave refraction at (a) 20 kHz and (b) 40 kHz. 89
7.1. Relations between the phase speed and frequency for a 1 cm thick plate. The red curve is calculated using Kirchhoff model, the blue curve is calculated using Timoshenko/Mindlin model, and the black circles are extracted from FEM simulations. 93
7.2. Relations between the phase speed and thickness of the plate at 60 kHz. The blue curve is calculated using Timoshenko/Mindlin model, and the black circles are extracted from FEM simulations. 94
7.3. Anomalous refraction by a metasurface comprised of several unit structures. The black arrows indicate the propagation direction of the wave, the red arrow indicate the direction of particle motion. The blue lines show the phase gradient in each unit structure. 95
7.4. SV- and P-wave splitting at 60 kHz. (a) shows the curl of the displacements to represent SV-waves, (b) shows the trace of the strain to represent P-waves. The black arrows indicated the propagation direction of the waves. 96

7.5. Asymmetric elastic transmission through metasurfaces. The green slab is a gradient metasurface for anomalous refraction, the blue slab is a uniform metasurface has lower effective speed. The black and red arrows idicate the propagation direction where the wave is incident from the left side in (a) and is incident from the right side in (b). 98

7.6. Asymmetric transmission for normally incident SV-waves (a) from the left side, (b) from the right side. The black arrows indicate the propagation direction. 99

8.1. Gyroid structures. (a) A cube comprised of 6×6 unit cells, (b) the Irreducible Brillouin Zone of the structure. 109

8.2. Dispersion curves along the $\Gamma - X$ path of the IBZ for the gyroid structure without fluid. 110

8.3. Dispersion curves along the $\Gamma - X$ path of the IBZ for the gyroid structure saturated by the same fluid. 112

8.4. Dispersion curves along the $\Gamma - X$ path of the IBZ for the gyroid structure saturated by two distinct fluids. 113

Chapter 1

Introduction

1.1 Brief introduction to metamaterials

The term metamaterial (from the Greek prefix *meta*, meaning *beyond*) has been in use for nearly two decades, first introduced by Walser in 2000 [4]. Although there is no official definition for metamaterials, it is widely known that they are artificial macroscopic composites comprised of tuned periodic microstructures that exhibit peculiar properties absent in nature. The first metamaterial related work dates back to 1968 [5]. Veselago described the physics for materials exhibit simultaneously negative permeability and permittivity, but it did not receive much attention probably because these properties were not found in natural materials. In 2000, Smith *et al.* [6] proposed a composite material with double negative parameters and demonstrated experimentally [7]. Meanwhile, Pendry [8] theoretically demonstrated that negative refractive index could make a perfect lens because the imaginary component can be reconstructed in the near field. Since then, numerous articles report super resolution imaging or super lensing in the context of electromagnetics and acoustics.

Many other novel phenomena are found in man-made structures. For instance, Sánchez-Pérez *et al.* [9] found full acoustic band gaps in two dimensional (2D) periodic array of rigid cylinders; Liu *et al.* [10] proposed and fabricated a locally resonant sonic material with negative dynamic mass density. Later on, various sonic and phononic crystals for sound manipulation [11, 12, 13, 14, 15, 16] and acoustic metamaterial with negative dynamic parameters are demonstrated [17, 18, 19, 20, 21]. Transformation optics and transformation acoustics are of particular interest to many researchers. In 2006, Pendry *et al.* [22] derived the transformation for the first cloak for electromagnetic waves. Numerous other regular spatial transformations which also leave the wave equation invariant are proposed to

manipulate electromagnetic wave propagation in many other different ways, such as directional antennas [23], field rotators [24], concentrators [25], beam shifters and splitters [26], just to name a few. Naturally, the transformation based acoustic metamaterials has been proposed starting with cloaking. Cummer *et al.* [27] theoretically analyzed 2D acoustic cloaking with anisotropic mass density, which is then extended to 3D by Chen *et al.* [28]. Then Norris [29] published a theory on acoustic cloaking with anisotropic bulk modulus and suggested to design using pentamode material (PM) proposed by Milton *et al.* [30]. Other transformation based acoustic metamaterials include ground carpet cloaks [31, 32] and cylindrical-to-plane wave lenses [33, 34]. Recent advances in acoustic metamaterials involve unidirectional transmission or sometimes referred as acoustic diode [15, 35, 36, 37], non-reciprocal acoustics [38, 39, 40], topological acoustics [41, 42, 43, 44] and acoustic absorbers [45, 46, 47].

The aim of this dissertation is to design metamaterials for both acoustic and elastic wave control. More specifically, several metamaterial devices are proposed to achieve full control of the transmitted wave for different applications, such as focusing, collimation, beam splitting and asymmetric transmission.

1.2 Motivation and current objectives

1.2.1 Acoustic metamaterials

The gradient index (GRIN) phononic crystal satisfying a hyperbolic secant profile has been demonstrated to be capable of focusing sound inside the lens [14]. Climente *et al.* [48] employed this index gradient to design a sonic crystal and demonstrated the focusing effect outside the lens with low aberration experimentally. Later on, a few researchers claim that their GRIN lens can focus sound outside the lens without aberration. However, this is not true since the ray trajectories are changed outside the lens which yields a cylindrical aberration. The index gradient is derived simply using ray theory with the assumption that the horizontal slowness component between layers is constant. A one dimensional (1D) coordinate stretch is introduced in this dissertation to modify the index gradient for aberration

reduction. To achieve high transmission, it is essential to match the impedance of the metamaterial to the acoustic medium. The main objective here is to design a transparent lens for focusing sound with reduced aberration. Another purpose of the dissertation is to design metamaterial devices for converting monopole to plane wave beams. A conformal transformation acoustics mapping is thus derived for allowing energy radiation preferentially in different directions. The metamaterial devices developed in this dissertation have potential applications in ultrasound medical imaging, energy harvesting and acoustic collimation.

1.2.2 Elastic metamaterials

Elastic metamaterials and phononic crystals are mostly designed for surface waves and plate waves. For instance, cloaking of elastic waves on thin plates was demonstrated by Farhat *et al.* [49] and Stenger *et al.* [50], respectively. The focusing effect of elastic waves has also been achieved by researchers [51, 52, 53]. However, there are few articles report metamaterial control of bulk elastic waves. Another topic of this dissertation is to introduce a new type of metamaterial element for controlling transmitted elastic wave-fronts. The proposed metamaterials include a GRIN lens for focusing SV-wave, a elastic prism for splitting P- and SV-waves, as well as a device for asymmetric transmission. Several metasurface devices are also designed for similar purposes. The design approach in this dissertation provides a novel way to manipulate the propagation of bulk elastic waves, and may have potential applications in structural health monitoring, energy harvesting and seismic wave control.

1.3 Outline of the Dissertation accomplishments

The dissertation is outlined as follows. Wave propagation and homogenization in 3D lattices are studied in Chapter 2. A semi-analytical method for band structure computation is developed using thin beam theory by imposing Bloch-Floquet periodic condition. The acoustic transmission through slanted gratings of anisotropic inertia is investigated in Chapter 3. The main result is that if the plane wave is incident from the so-called intromission angle, the acoustic energy can totally transmit through the gratings. In Chapter 4, a broadband transparent GRIN lens for focusing underwater sound is designed and demonstrated

experimentally. The refractive indices obeys a modified hyperbolic secant index profile such that the cylindrical aberration is minimized. In Chapter 5, two GRIN lenses for converting monopole source to plane wave beams are designed and demonstrated using full wave FEM simulations. The index and material property distributions are derived using a conformal transformation acoustics mapping which takes a unit circle to a triangle. Elastic metamaterials for controlling the transmitted bulk waves are presented in Chapter 6. An analytical model is established to study the transmission and reflection of P- and SV-waves through aligned parallel plates. Metamaterial devices are designed to focus SV-wave, split P- and SV-waves, and achieve asymmetric transmission. In Chapter 7, we further apply this idea into metasurface designs. A novel device for asymmetric transmission of SV-wave is proposed. Finally, the elastic waves in fluid-saturated cubic double porosity medium is investigated in Chapter 8. It is notable that a second slow wave is predicted in the theory developed in this chapter. The conclusions on the accomplished work and an outlook on the future research are presented in Chapter 9.

Chapter 2

Wave propagation and homogenization in 3D lattices

Elastic networks of connected beams, i.e. lattices, exhibit the rich phenomena that are found in periodic elastic structures. The multiple wave types yield complex dispersion properties, described by Bloch-Floquet band diagrams, such as band gaps [54, 55] and anisotropic propagation [56]. At the low frequency homogenization limit, the acoustic properties of the lattice structures can be designed to match the properties of water, while at the high frequency range they may exhibit peculiar properties such as negative refractive index. For instance, Hladky-Hennion *et al.* [16] used a metallic foam-like metal lens to achieve negative refraction and demonstrated experimentally. The properties of the lens is studied by computing the band diagram, thus it is essential to develop a highly efficient method to plot the dispersion curves.

Regarding several methods for solving wave propagation problems in lattices, we note that finite elements methods (FEM) have been specifically designed to treat lattice structures by many researchers [55, 56, 57]. An alternative wave-based approach for determining the Bloch waves in 2D periodic structures was proposed by Leamy [58]. The analytical method considers the explicit waves propagating back and forth on each member, coupled by reflection and transmission matrices at joints. However, FEM based computation usually requires at least six mesh grids per wavelength, while the reflection and transmission matrices require large matrix systems in the latter approach. They all involve large systems to be solved, thus are expensive in computational time. The present method is similar to that of Ref. [58] in that both approaches yield exact dispersion relations within the context of the beam theories employed (Timoshenko beam theory was used in Ref. [58]). However, the present approach is simpler in that it does not require propagation and reflection/transmission matrices for the multiple wave types. Instead, in the present method

the dynamic stiffness matrix relates forces at the two ends of a beam member to the displacements at either end. It is notable that our analysis do not include torsional effects in each beam members. Here we consider beams with large length to thickness ratio so that bending is the dominant effect for producing torsion on the lattice structure. Another reason for neglecting torsional modes is that their micro-effects do not contribute to the static effective medium. This assumption is later confirmed in our examples.

At the *quasi-static* or homogenization limit, a few static homogenization theory for general lattice structures has been developed by several authors, e.g. [59, 60]. Nevertheless, static models ignoring flexural effects do not properly account for the distributed mass on the wave-bearing properties of the structure, and cannot yield the correct *quasi-static* results [61]. We develop further the dynamic stiffness matrix approach, which combines longitudinal and flexural forces, proposed by Martinsson *et al.* [54] and Colquitt *et al.* [61, 62]. In this chapter, we mainly focus on the 3D cubic and tetrahedral unit cell lattices. The formulation is semi-analytical to the extent that all matrix elements are explicit, numerical computation is required only at the final stage. The semi-analytical nature of the solution allows us to extract the low frequency asymptotics, and to find closed-form expressions for the *quasi-static* Christoffel matrix, as demonstrated for cubic lattice.

This chapter is organized as follows. In Sec. 2.1, we describe the structures considered in this chapter, and introduce the parameters as well as the coordinate systems. The solutions to the wave equations on the rods and the dynamic stiffness matrices are presented in Sec. 2.2. We then formulate the dispersion relations in Sec. 2.3. The explicit form of dispersion relations for cubic lattice are derived in Sec. 2.4. The dispersion curves of diamond lattice are computed using a semi-analytical approach in Sec. 2.5. The *quasi-static* effective moduli of cubic lattice is derived in Sec. 2.6. Discussions are presented in Sec. 2.7.

2.1 Description of the problem

2.1.1 Description of the structures and parameters

Two typical examples of the lattice structures $\wp$ considered in this chapter are shown in Fig. 2.1. Every point $\mathbf{a}_i$ is connected with adjacent points $\mathbf{a}_j$ by beams/rods. Each beam/rod

has length l_{ij}, uniform Young's modulus μ_{ij}, density ρ_{ij}, lineal density d_{ij} and bending coefficient λ_{ij}. The mass at each node point is m_i and moment of inertia is I_i. All the properties in any translated cell $\wp + l_1\mathbf{d}_1 + l_2\mathbf{d}_2 + l_3\mathbf{d}_3$ coincide with those in $\wp$.

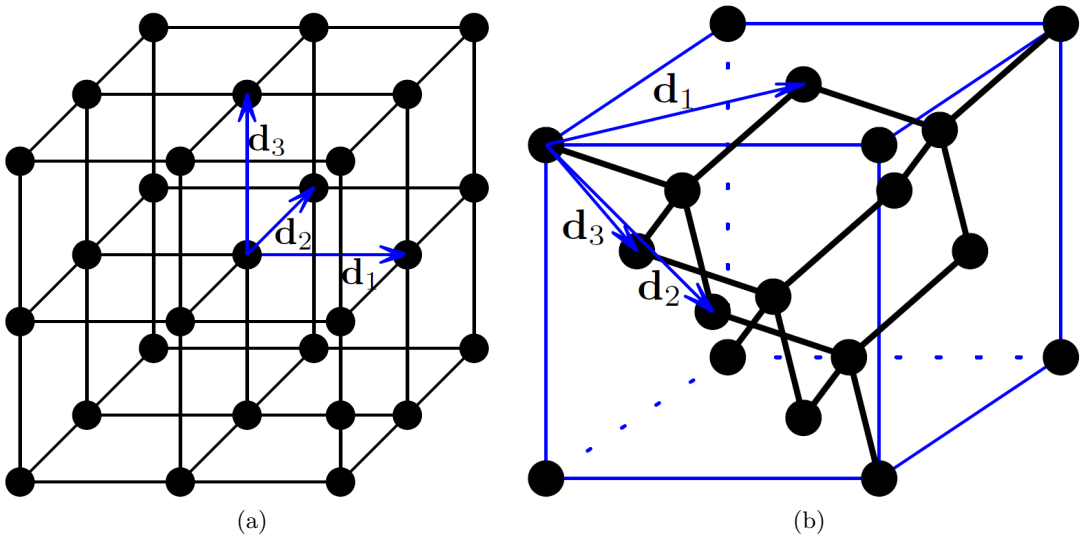

Figure 2.1: Geometry of lattices structures. (a) Cubic lattice and (b) diamond lattice.

2.1.2 Definition of the coordinate system

When considering the force on each rod in a cartesian coordinate system $(x-y-z)$, we use $\mathbf{e}_1$, $\mathbf{e}_2$ and $\mathbf{e}_3$ to denote each direction of displacement, and $\mathbf{e}_1^b$, $\mathbf{e}_2^b$ and $\mathbf{e}_3^b$ to denote each angle of bending. Here we introduce a set of vectors to represent these directions as shown in Fig. 2.2. The vectors are defined as 6-dimensional

$$\mathbf{e}_1 = \begin{pmatrix}1\\0\\0\\0\\0\\0\end{pmatrix}, \mathbf{e}_2 = \begin{pmatrix}0\\1\\0\\0\\0\\0\end{pmatrix}, \mathbf{e}_3 = \begin{pmatrix}0\\0\\1\\0\\0\\0\end{pmatrix}, \mathbf{e}_1^b = \begin{pmatrix}0\\0\\0\\1\\0\\0\end{pmatrix}, \mathbf{e}_2^b = \begin{pmatrix}0\\0\\0\\0\\1\\0\end{pmatrix}, \mathbf{e}_3^b = \begin{pmatrix}0\\0\\0\\0\\0\\1\end{pmatrix}. \tag{2.1}$$

The effective force on each beam/rod can be expressed in terms of the vectors defined on its local coordinate system. By applying the Euler angle coordinate system transformation,

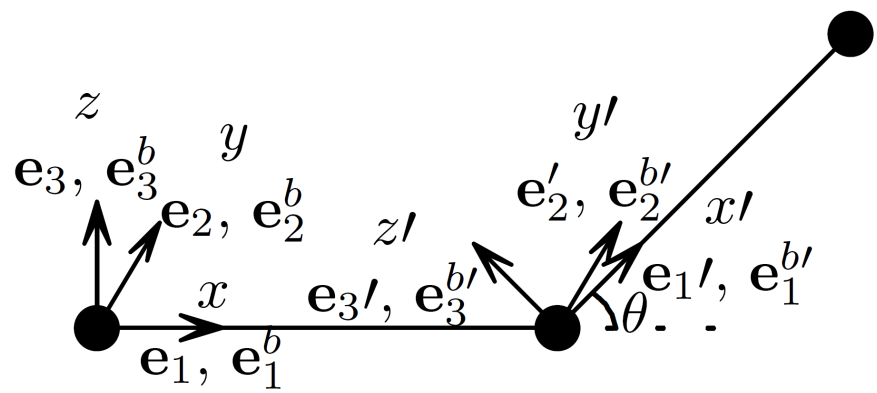

Figure 2.2: Coordinate system transformation

we can relate the effective force on each beam/rod to the inertial coordinate system. Note that the x-axis should be along the beam/rod after the transformation. For example, we take a rotation of angle θ around y-axis as shown in Fig. 2.2, then the local coordinate system can be related to the inertial coordinate system by

$$\begin{pmatrix} i' \\ j' \\ k' \end{pmatrix} = R(\theta) \begin{pmatrix} i \\ j \\ k \end{pmatrix}, \tag{2.2}$$

where $R(\theta)$ is the matrix representation of rotation operator, and $(i, j, k)^T$ and $(i', j', k')^T$ denote the component of $\mathbf{e}$ in the coordinate system before and after transformation. See Appendix.A for detailed discussion of coordinate transformation for cubic lattice.

2.2 Dynamic stiffness matrices

2.2.1 Solution of the longitudinal wave equation

We first consider logitudinal force on the rod $\mathbf{a}_i - \mathbf{a}_j$. Assume that the displacements at $\mathbf{a}_i$ and $\mathbf{a}_j$ are $\mathbf{u}_i$ and $\mathbf{u}_j$, respectively. Let x be the 1D coordinate on the rod. The displacement $u_{ij}(x)$ satisfies the wave equation and boundary conditions:

$$\mu_{ij} \frac{\partial^2}{\partial x^2} u_{ij} = -\omega^2 d_{ij} u_{ij}, \quad u_{ij}(0) = \mathbf{e}_1 \cdot \mathbf{u}_i, \quad u_{ij}(l_{ij}) = \mathbf{e}_1 \cdot \mathbf{u}_j. \tag{2.3}$$

The displacement $u_{ij}(x)$ is the solution of Eq. (2.3). Plugging in the boundary conditions, we obtain

$$u_{ij}(x) = \frac{\mathbf{e}_1 \cdot \mathbf{u}_i \sin(s_{ij}\omega(l_{ij} - x)) + \mathbf{e}_1 \cdot \mathbf{u}_j \sin(s_{ij}\omega x)}{\sin(s_{ij}\omega l_{ij})}, \quad s_{ij} = \sqrt{\frac{\rho_{ij}}{\mu_{ij}}}. \tag{2.4}$$

Then the longitudinal force $\mathbf{f}_{ij}$ acting on the point $\mathbf{a}_i$ is simply related to the strain via Hooke's law. Using Eq. (2.4), we have

$$\mathbf{f}_{ij}^{(1)} = \mu_{ij} \frac{\partial u_{ij}}{\partial x}(0)\mathbf{e}_1 = \frac{\mu_{ij} s_{ij}\omega}{\sin(s_{ij}\omega l_{ij})} \mathbf{e}_1 \mathbf{e}_1^T \big(\mathbf{u}_j - \mathbf{u}_i \cos(s_{ij}\omega l_{ij})\big), \tag{2.5}$$

where the displacements at both ends of the beam/rod are involved.

2.2.2 Solution to the flexural wave equation

The flexural wave on the beam/rod also contribute to the effective total force. Now we consider flexural wave equation on the beam/rod

$$\frac{\partial^4 w}{\partial x^4} - \gamma^4 w = 0, \quad x \in [0, l]. \tag{2.6}$$

The solutions to the flexural wave equation are related to the displacements ($w_{ij}(0)$, $w_{ij}(l)$) and rotations ($w'_{ij}(0)$, $w'_{ij}(l)$) at both ends as

$$\begin{aligned} w(x) = {} & \frac{1}{2(1 - cc_h)} \Big\{ \big[(c - c_h)(\cos\gamma x - \cosh\gamma x) + (s + s_h)(\sin\gamma x - \sinh\gamma x)\big] w(l) \\ & + \frac{1}{\gamma}\big[(s_h - s)(\cos\gamma x - \cosh\gamma x) + (c - c_h)(\sin\gamma x - \sinh\gamma x)\big] w'(l) \\ & + \big[(1 - cc_h + ss_h)\cos\gamma x + (1 - cc_h - ss_h)\cosh\gamma x + (cs_h + sc_h)(\sinh\gamma x - \sin\gamma x)\big] w(0) \\ & + \frac{1}{\gamma}\big[(sc_h - cs_h)(\cos\gamma x - \cosh\gamma x) + (1 - cc_h - ss_h)\sin\gamma x + (1 - cc_h + ss_h)\sinh\gamma x\big] w'(0) \Big\}, \end{aligned} \tag{2.7}$$

where $c = \cos\gamma l$, $s = \sin\gamma l$, $c_h = \cosh\gamma l$, $s_h = \sinh\gamma l$. Hence,

$$\begin{pmatrix} w'''(0) \\ -w''(0) \\ -w'''(l) \\ w''(l) \end{pmatrix} = \mathbf{K}(\omega) \begin{pmatrix} w(0) \\ w'(0) \\ w(l) \\ w'(l) \end{pmatrix}, \tag{2.8}$$

where

$$\mathbf{K}(\omega) = \frac{1}{1-cc_h}\begin{pmatrix} \gamma^3(cs_h+sc_h) & \gamma^2 ss_h & -\gamma^3(s+s_h) & \gamma^2(c_h-c) \\ \gamma^2 ss_h & \gamma(sc_h-cs_h) & \gamma^2(c-c_h) & \gamma(s_h-s) \\ -\gamma^3(s+s_h) & \gamma^2(c-c_h) & \gamma^3(cs_h+sc_h) & -\gamma^2 ss_h \\ \gamma^2(c_h-c) & \gamma(s_h-s) & -\gamma^3 ss_h & \gamma(sc_h-cs_h) \end{pmatrix}. \tag{2.9}$$

We may rewrite $\mathbf{K}(\omega)$ as

$$\mathbf{K} = \begin{pmatrix} \mathbf{K}_1 & \mathbf{K}_2 \\ \mathbf{K}_2^T & \mathbf{K}_3 \end{pmatrix}, \tag{2.10}$$

where $\mathbf{K}$ is the "traditional" form of the Euler-Bernoulli dynamic stiffness matrix. In particular

$$\begin{aligned} \mathbf{K}_1 &= \begin{pmatrix} 12 & 6 \\ 6 & 4 \end{pmatrix} + \frac{\gamma^4}{35}\begin{pmatrix} -13 & -\frac{11}{6} \\ -\frac{11}{6} & -\frac{1}{3} \end{pmatrix} + \mathrm{O}(\gamma^8) \quad (l=1), \\ \mathbf{K}_2 &= \begin{pmatrix} -12 & 6 \\ -6 & 2 \end{pmatrix} + \frac{\gamma^4}{70}\begin{pmatrix} -9 & \frac{13}{6} \\ -\frac{13}{6} & \frac{1}{2} \end{pmatrix} + \mathrm{O}(\gamma^8) \quad (l=1). \end{aligned} \tag{2.11}$$

2.2.3 The flexural wave equation and BCs on the rod.

Different from the 2D lattices, the 3D model has two bending components in the direction of y and z as shown in Fig. 2.3. They represent the shear effect with different polarizations at the *quasi-static* regime, so that they both need to be considered in the model. We will treat these two bending components separately in the following.

Bending in y-direction

The flexural wave equation and boundary conditions in y-directions are:

$$-\lambda_{ij}\frac{\partial^4 w_y}{\partial x^4} = -\omega^2 d_{ij} w_y, \tag{2.12}$$

$$w_y(0) = \mathbf{e}_2 \cdot \mathbf{u}_i, \quad w_y(l) = \mathbf{e}_2 \cdot \mathbf{u}_j, \quad w_y'(0) = \mathbf{e}_3^b \cdot \mathbf{u}_i, \quad w_y'(l) = \mathbf{e}_3^b \cdot \mathbf{u}_j.$$

We define all the displacements in right-handed coordinate system, and define the positive direction by the right hand rule. Note that $w_y'(0)$ and $w_y'(l)$ both have positive sign. The

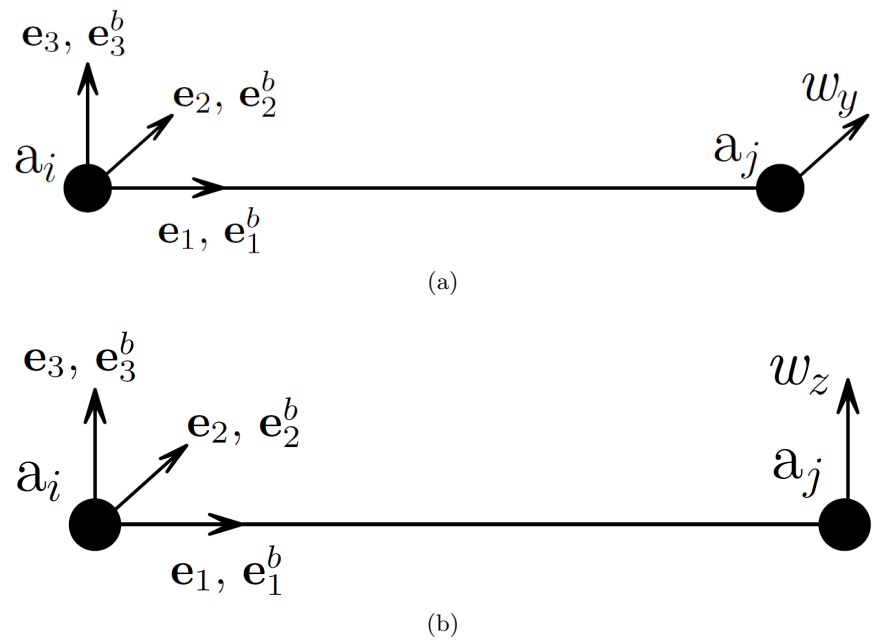

Figure 2.3: Bending components one each beam/rod. (a) Deflection in $y-$direction and (b) deflection in $z-$direction.

force at point $\mathbf{a}_i$ due to bending is related to the shear force and bending moment on the beam/rod through the stiffness matrices as defined in Eq. (2.11), we have

$$\begin{aligned}\mathbf{f}_{ij}^{(2)} = -\lambda_{ij}\frac{\partial^3 w_y}{\partial x^3}\mathbf{e}_2 + \lambda_{ij}\frac{\partial^2 w_y}{\partial x^2}\mathbf{e}_3^b = &-\lambda_{ij}\big(\mathbf{e}_2,\ \mathbf{e}_3^b\big)\mathbf{K}_1\big(\mathbf{e}_2,\ \mathbf{e}_3^b\big)^T\cdot\mathbf{u}_i \\ &-\lambda_{ij}\big(\mathbf{e}_2,\ \mathbf{e}_3^b\big)\mathbf{K}_2\big(\mathbf{e}_2,\ \mathbf{e}_3^b\big)^T\cdot\mathbf{u}_j.\end{aligned} \tag{2.13}$$

The component in $\mathbf{e}_2$ direction in Eq. (2.13) is shear force and has a negative sign, and the $\mathbf{e}_3^b$ component is bending moment.

Bending in z-direction

Similarly, the flexural wave equation and boundary conditions in z-directions are:

$$-\lambda_{ij}\frac{\partial^4 w_z}{\partial x^4} = -\omega^2 d_{ij} w_z, \tag{2.14}$$

$$w_z(0) = \mathbf{e}_3\cdot\mathbf{u}_i,\ \ w_z(l) = \mathbf{e}_3\cdot\mathbf{u}_j,\ \ \ w_z'(0) = -\mathbf{e}_2^b\cdot\mathbf{u}_i,\ \ \ w_z'(l) = -\mathbf{e}_2^b\cdot\mathbf{u}_j,$$

Since we define all displacements in positive direction, $w_z'(0)$ and $w_z'(l)$ both have negative sign by the right hand rule. The force at point $\mathbf{a}_i$ due to bending is related to the

shear force and bending moment on the beam/rod through the stiffness matrices as defined in Eq. (2.11), we have

$$\mathbf{f}_{ij}^{(3)} = -\lambda_{ij}\frac{\partial^3 w_z}{\partial x^3}\mathbf{e}_3 - \lambda_{ij}\frac{\partial^2 w_z}{\partial x^2}\mathbf{e}_2^b = -\lambda_{ij}\big(\mathbf{e}_3,\, -\mathbf{e}_2^b\big)\mathbf{K}_1\big(\mathbf{e}_3,\, -\mathbf{e}_2^b\big)^T \cdot \mathbf{u}_i \\ -\lambda_{ij}\big(\mathbf{e}_3,\, -\mathbf{e}_2^b\big)\mathbf{K}_2\big(\mathbf{e}_3,\, -\mathbf{e}_2^b\big)^T \cdot \mathbf{u}_j. \tag{2.15}$$

The component in $\mathbf{e}_3$ direction is shear force and has a negative sign. The $\mathbf{e}_2^b$ component is bending moment, and has a negative sign by the right hand rule.

2.2.4 Total force and dynamic stiffness

The total force at point $\mathbf{a}_i$ is the superposition of longitudinal force at $x = 0$ and effective force due to bending components in $y-$ and $z-$ directions at $x = 0$

$$\mathbf{f}_{ij} = \mathbf{f}_{ij}^{(1)}(0) + \mathbf{f}_{ij}^{(2)}(0) + \mathbf{f}_{ij}^{(3)}(0). \tag{2.16}$$

Now we introduce some new parameters to simplify the notations

$$\begin{aligned} &\tilde{s}_{ij} = \omega s_{ij} l_{ij}, \quad \tilde{\mu}_{ij} = \mu_{ij}/l_{ij}, \\ &\gamma_{ij} = \big(\omega^2 d_{ij}/l_{ij}\big)^{1/4}\ (\equiv \gamma), \quad \tilde{\gamma}_{ij} = \gamma_{ij} l_{ij}, \\ \Rightarrow\ &c = \cos\tilde{\gamma}_{ij}, \quad s = \sin\tilde{\gamma}_{ij}, \quad c_h = \cosh\tilde{\gamma}_{ij}, \quad s_h = \sinh\tilde{\gamma}_{ij}, \end{aligned} \tag{2.17}$$

and define the frequency dependent effective force matrices

$$\begin{aligned} \mathbf{P}_{ij}^{(1)} &= \tilde{\mu}_{ij}\tilde{s}_{ij}\cot\tilde{s}_{ij}\mathbf{e}_1\mathbf{e}_1^T + \lambda_{ij}\big(\mathbf{e}_2,\, \mathbf{e}_3^b\big)\mathbf{K}_1\big(\mathbf{e}_2,\, \mathbf{e}_3^b\big)^T + \lambda_{ij}\big(\mathbf{e}_3,\, -\mathbf{e}_2^b\big)\mathbf{K}_1\big(\mathbf{e}_3,\, -\mathbf{e}_2^b\big)^T, \\ \mathbf{P}_{ij}^{(2)} &= \tilde{\mu}_{ij}\tilde{s}_{ij}\csc\tilde{s}_{ij}\mathbf{e}_1\mathbf{e}_1^T - \lambda_{ij}\big(\mathbf{e}_2,\, \mathbf{e}_3^b\big)\mathbf{K}_2\big(\mathbf{e}_2,\, \mathbf{e}_3^b\big)^T - \lambda_{ij}\big(\mathbf{e}_3,\, -\mathbf{e}_2^b\big)\mathbf{K}_2\big(\mathbf{e}_3,\, -\mathbf{e}_2^b\big)^T, \\ \mathbf{P}_{ij}^{(3)} &= \tilde{\mu}_{ij}\tilde{s}_{ij}\cot\tilde{s}_{ij}\mathbf{e}_1\mathbf{e}_1^T + \lambda_{ij}\big(\mathbf{e}_2,\, \mathbf{e}_3^b\big)\mathbf{K}_4\big(\mathbf{e}_2,\, \mathbf{e}_3^b\big)^T + \lambda_{ij}\big(\mathbf{e}_3,\, -\mathbf{e}_2^b\big)\mathbf{K}_4\big(\mathbf{e}_3,\, -\mathbf{e}_2^b\big)^T. \end{aligned} \tag{2.18}$$

The force at point $\mathbf{a}_i$ can be rewritten as

$$\mathbf{f}_{ij} = \mathbf{P}_{ij}^{(2)}\mathbf{u}_j - \mathbf{P}_{ij}^{(1)}\mathbf{u}_i, \tag{2.19}$$

which relates the displacements at u_i and u_j, i.e. the displacements at both ends of the beam/rod.

2.3 Analytical dispersion relations

2.3.1 Total force and Bloch-Floquet periodic conditions

The equilibrium equation at point $\boldsymbol{a}_i$ is formulated by adding the effective forces in each beam/rod connected to $\boldsymbol{a}_i$, and relate to the mass and acceleration at $\boldsymbol{a}_i$, we have

$$\sum_{j\in N_i} \mathbf{f}_{ij} = -\omega^2 \mathbf{M}_i \mathbf{u}_i, \quad \mathbf{M}_i = \mathrm{diag}(m_i, m_i, m_i, I_i, I_i, I_i), \tag{2.20}$$

where N_i is the set of points connected with $\mathbf{a}_i$.

In the general 3D case, there are two points $\mathbf{a}_1$ and $\mathbf{a}_2$ inside unite cell $\wp$ spanned on vectors $\mathbf{d}_1$, $\mathbf{d}_2$ and $\mathbf{d}_3$, and four links from each of them. Applying the Floquet periodicy conditions

$$\begin{aligned} \mathbf{u}_j &= \exp(i\mathbf{k}\cdot\mathbf{g}_j)\mathbf{u}_1, \quad \mathbf{g}_j = \mathbf{a}_j - \mathbf{a}_1, \quad j \in N_2 \\ \mathbf{u}_j &= \exp(i\mathbf{k}\cdot\mathbf{g}_j)\mathbf{u}_2, \quad \mathbf{g}_j = \mathbf{a}_j - \mathbf{a}_2, \quad j \in N_1 \end{aligned} \tag{2.21}$$

into Eqs. (2.19) and (2.20) leads to

$$\begin{aligned} \sum_{j\in\mathcal{N}_1} \left(\mathbf{P}_{1j}^{(2)} \exp(i\mathbf{k}\cdot\mathbf{g}_j)\, \mathbf{u}_2 - \mathbf{P}_{1j}^{(1)}\mathbf{u}_1\right) &= -\omega^2 \mathbf{M}_1 \mathbf{u}_1, \\ \sum_{j\in\mathcal{N}_2} \left(\mathbf{P}_{2j}^{(2)} \exp(i\mathbf{k}\cdot\mathbf{g}_j)\, \mathbf{u}_1 - \mathbf{P}_{2j}^{(1)}\mathbf{u}_2\right) &= -\omega^2 \mathbf{M}_2 \mathbf{u}_2. \end{aligned} \tag{2.22}$$

Note that we have shown how to calculate $\mathbf{P}_{ij}$ for each of the rod, then we can express each of them in the inertial coordinate by substituting the old $\mathbf{e}$ by the new one, shown in Sec. 2.1.2, and finally compute the summation.

2.3.2 Dispersion relations

It is possible to express the second equation of Eq. (2.22) in terms of a sum over neighboring links of $\boldsymbol{a}_1$. Introducing matrices

$$\mathbf{H}_1 = \sum_{j\in\mathcal{N}_1} \mathbf{P}_{1j}^{(1)}, \quad \mathbf{H}_2 = -\sum_{j\in\mathcal{N}_1} \mathbf{P}_{1j}^{(2)} \exp(i\mathbf{k}\cdot\mathbf{g}_j), \quad \mathbf{H}_3 = \sum_{j\in\mathcal{N}_1} \mathbf{P}_{1j}^{(3)} \tag{2.23}$$

and using the identities $\mathbf{K}_2^T = \mathbf{J}\mathbf{K}_2\mathbf{J}$, $\mathbf{K}_3 = \mathbf{J}\mathbf{K}_1\mathbf{J}$ where $\mathbf{J} = \begin{pmatrix} 1 & 0 \\ 0 & -1 \end{pmatrix}$, which imply

$$\sum_{j\in\mathcal{N}_2} \mathbf{P}_{2j}^{(1)} = \sum_{j\in\mathcal{N}_1} \mathbf{P}_{1j}^{(3)}, \quad \sum_{j\in\mathcal{N}_2} \mathbf{P}_{2j}^{(2)} e^{i\mathbf{k}\cdot\mathbf{g}_j} = \Big(\sum_{j\in\mathcal{N}_1} \mathbf{P}_{1j}^{(2)} e^{i\mathbf{k}\cdot\mathbf{g}_j}\Big)^+, \tag{2.24}$$

where + denotes the Hermitian conjugation. Equation (2.22) can be rewritten in the form

$$\mathbf{H}\mathbf{u} = \omega^2 \mathbf{M}\mathbf{u} \tag{2.25}$$

with

$$\mathbf{u} = \begin{pmatrix} \mathbf{u}_1 \\ \mathbf{u}_2 \end{pmatrix}, \quad \mathbf{M} = \mathrm{diag}(\mathbf{M}_1, \mathbf{M}_2), \quad \mathbf{H} \equiv \mathbf{H}(\omega, \mathbf{k}) = \begin{pmatrix} \mathbf{H}_1 & \mathbf{H}_2 \\ \mathbf{H}_2^+ & \mathbf{H}_3 \end{pmatrix}. \tag{2.26}$$

Then dispersion curves $\omega_n(\mathbf{k})$ can be found from the equation

$$\det(\mathbf{H}(\omega, \mathbf{k}) - \omega^2 \mathbf{M}) = 0. \tag{2.27}$$

Note that the matrices $\mathbf{H}_1$ and $\mathbf{H}_3$ are real symmetric, so that the matrix $\mathbf{H}$ is Hermitian, in turn guaranteeing that the dispersion relation Eq. (2.27) is real valued for real ω, $\mathbf{k}$. It is also notable that the theory captures the low frequency properties accurately, although the torsional effect is not considered in theory. We will see in the following that the torsional modes do not exist in the *quasi-static* regime.

2.4 Cubic lattice

2.4.1 Dispersion relations

Consider the cubic lattice in Fig. 2.4 in which there is only one center mass point, then the Floquet periodicity condition reduce to

$$\mathbf{u}_j = \exp(i\mathbf{k} \cdot \mathbf{g}_j)\mathbf{u}_0, \quad \mathbf{g}_j = \mathbf{a}_j - \mathbf{a}_0, \tag{2.28}$$

which relates each joint to the center mass. The equations of motion of $\mathbf{a}_0$ is also reduced to the equilibrium of one mass point and written as

$$\sum_{j=1,2,3,4,5,6} \big(\mathbf{P}_{0j}^{(1)} - \mathbf{P}_{0j}^{(2)} \mathbf{e}^{i\mathbf{k}\cdot\mathbf{g}_j}\big)\mathbf{u}_0 = \omega^2 \mathbf{M}_0 \mathbf{u}_0. \tag{2.29}$$

In the theory we derived above, the cubic lattice under consideration is allowed to have beams/rods of different properties. We have with obvious notation K_{11}^{0j}, etc., and noting that $K_{12}^{0j} = K_{21}^{0j}$, $K_{23}^{0j} = -K_{14}^{0j}$. The effective force on each beam/rod are expressed as

$$\begin{aligned} \mathbf{P}_{0j}^{(1)} &= \tilde{\mu}_{0j} \tilde{s}_{0j} \cot \tilde{s}_{0j} \mathbf{J}_j + \lambda_{0j} \Big[K_{11}^{0j} \mathbf{L}_1 + K_{22}^{0j} \mathbf{L}_2 + K_{12}^{0j} \mathbf{L}_3 \Big], \\ \mathbf{P}_{0j}^{(2)} &= \tilde{\mu}_{0j} \tilde{s}_{0j} \cot \tilde{s}_{0j} \mathbf{J}_j - \lambda_{0j} \Big[K_{13}^{0j} \mathbf{L}_1 + K_{24}^{0j} \mathbf{L}_2 + K_{14}^{0j} \mathbf{L}_4 \Big]. \end{aligned} \tag{2.30}$$

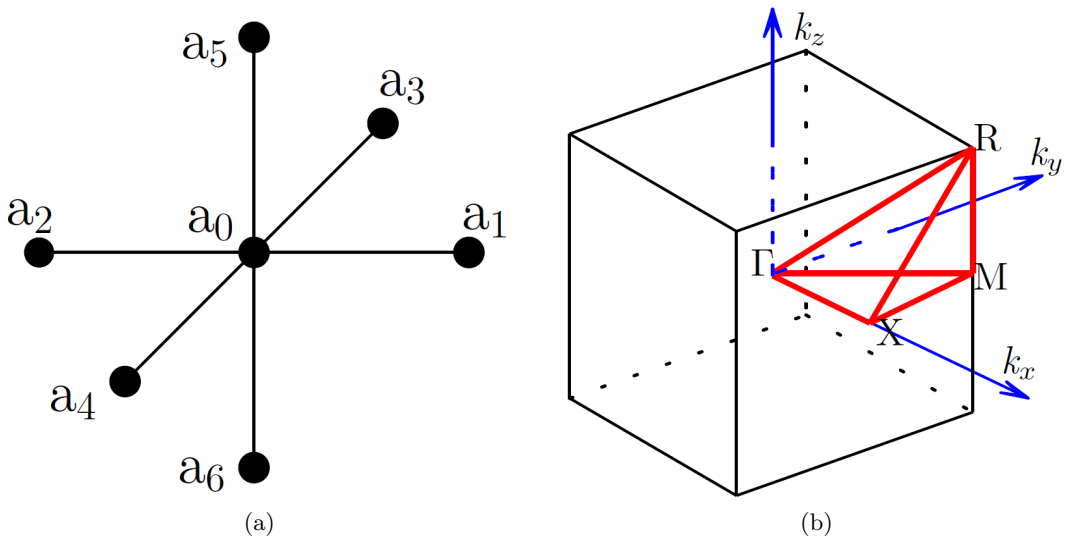

Figure 2.4: Cubic lattice. (a) The unit cell of a cubic lattice which has six mass points connected to the center mass through beam/rod members. (b) The Irreducible Brillouin Zone.

See Appendix. A for explicit details of coordinate transformation and matrix separations of $\mathbf{J}_{..}$ and $\mathbf{L}_{..}$.

By definition of lattice periodicity, we have

$$\tilde{\mu}_{01} = \tilde{\mu}_{02} = \tilde{\mu}_1, \quad \tilde{\mu}_{03} = \tilde{\mu}_{04} = \tilde{\mu}_2, \quad \tilde{\mu}_{05} = \tilde{\mu}_{06} = \tilde{\mu}_3,$$

$$\tilde{s}_{01} = \tilde{s}_{02} = \tilde{s}_1, \quad \tilde{s}_{03} = \tilde{s}_{04} = \tilde{s}_2, \quad \tilde{s}_{05} = \tilde{s}_{06} = \tilde{s}_3,$$

$$\tilde{\lambda}_{01} = \tilde{\lambda}_{02} = \tilde{\lambda}_1, \quad \tilde{\lambda}_{03} = \tilde{\lambda}_{04} = \tilde{\lambda}_2, \quad \tilde{\lambda}_{05} = \tilde{\lambda}_{06} = \tilde{\lambda}_3,$$

and the same for $K^{0j}_{..}$. Equation (2.29) becomes,

$$\omega^2 \mathbf{M}_0 \mathbf{u}_0 = \left\{ \begin{bmatrix} \tilde{\mu}_1 \tilde{s}_1 (\cot \tilde{s}_1 - \csc \tilde{s}_1 \cos \tilde{k}_x) & 0 & 0 & 0 & 0 & 0 \\ 0 & \tilde{\mu}_2 \tilde{s}_2 (\cot \tilde{s}_2 - \csc \tilde{s}_2 \cos \tilde{k}_y) & 0 & 0 & 0 & 0 \\ 0 & 0 & \tilde{\mu}_3 \tilde{s}_3 (\cot \tilde{s}_3 - \csc \tilde{s}_3 \cos \tilde{k}_z) & 0 & 0 & 0 \\ 0 & 0 & 0 & 0 & 0 & 0 \\ 0 & 0 & 0 & 0 & 0 & 0 \\ 0 & 0 & 0 & 0 & 0 & 0 \end{bmatrix} + \right.$$
$$\left. \begin{bmatrix} A_1 & 0 & 0 & 0 & i\lambda_3 K^{(3)}_{14} \sin \tilde{k}_z & -i\lambda_2 K^{(2)}_{14} \sin \tilde{k}_y \\ 0 & A_2 & 0 & -i\lambda_3 K^{(3)}_{14} \sin \tilde{k}_z & 0 & i\lambda_1 K^{(1)}_{14} \sin \tilde{k}_x \\ 0 & 0 & A_3 & i\lambda_2 K^{(2)}_{14} \sin \tilde{k}_y & -i\lambda_1 K^{(1)}_{14} \sin \tilde{k}_x & 0 \\ 0 & i\lambda_3 K^{(3)}_{14} \sin \tilde{k}_z & -i\lambda_2 K^{(2)}_{14} \sin \tilde{k}_y & A_4 & 0 & 0 \\ -i\lambda_3 K^{(3)}_{14} \sin \tilde{k}_z & 0 & i\lambda_1 K^{(1)}_{14} \sin \tilde{k}_x & 0 & A_5 & 0 \\ i\lambda_2 K^{(2)}_{14} \sin \tilde{k}_y & -i\lambda_1 K^{(1)}_{14} \sin \tilde{k}_x & 0 & 0 & 0 & A_6 \end{bmatrix} \right\} 2\mathbf{u}_0, \tag{2.31}$$

where

$$\tilde{k}_x = l_1 k_x, \quad \tilde{k}_y = l_2 k_y, \quad \tilde{k}_z = l_2 k_z. \tag{2.32}$$

$$
\begin{aligned}
A_1 &= \lambda_2(K_{11}^{(2)} + K_{13}^{(2)}\cos\tilde{k}_y) + \lambda_3(K_{11}^{(3)} + K_{13}^{(3)}\cos\tilde{k}_z),\\
A_2 &= \lambda_3(K_{11}^{(3)} + K_{13}^{(3)}\cos\tilde{k}_z) + \lambda_1(K_{11}^{(1)} + K_{13}^{(1)}\cos\tilde{k}_x),\\
A_3 &= \lambda_1(K_{11}^{(1)} + K_{13}^{(1)}\cos\tilde{k}_x) + \lambda_2(K_{11}^{(2)} + K_{13}^{(2)}\cos\tilde{k}_y),\\
A_4 &= \lambda_2(K_{22}^{(2)} + K_{24}^{(2)}\cos\tilde{k}_y) + \lambda_3(K_{22}^{(3)} + K_{24}^{(3)}\cos\tilde{k}_z),\\
A_5 &= \lambda_3(K_{22}^{(3)} + K_{24}^{(3)}\cos\tilde{k}_z) + \lambda_1(K_{22}^{(1)} + K_{24}^{(1)}\cos\tilde{k}_x),\\
A_6 &= \lambda_1(K_{22}^{(1)} + K_{24}^{(1)}\cos\tilde{k}_x) + \lambda_2(K_{22}^{(2)} + K_{24}^{(2)}\cos\tilde{k}_y).
\end{aligned}
\tag{2.33}
$$

Equation (2.31) is the equation of motion of a general cubic lattice, the full band diagram can be computed numerically by considering a eigenvalue problem of this equation. However, it is possible to compute the dispersion relations analytically when the structure is comprised of beams/rods of the same length and properties. This can be done by splitting the dispersion relations into pure longitudinal and flexural ones.

Assuming uniform properties for simplicity, we take all members to have the same properties $\tilde{\mu}_{ij} = \tilde{\mu}$, $\tilde{s}_{ij} = \tilde{s}$, $\lambda_{ij} = \lambda$, and $K_{ij}^{(1,2,3)} = K_{ij}$. Assuming a plane wave traveling in the direction of $\tilde{k}_x$ which coincide with the symmetry line $\Gamma - \mathrm{X}$ of the Irreducible Brillouin Zone as shown in Fig. 2.4(b). Let $\tilde{k}_y = \tilde{k}_z = 0$, and consider the first pure-longitudinal solution $\mathbf{u}_0 = (1,0,0,0,0,0)^T$ of (2.31), we have $\tilde{k}_x$ in terms of ω as

$$
\cos\tilde{k}_x = \cos\tilde{s} + \frac{\sin\tilde{s}}{\tilde{s}}\Big(2\frac{\lambda}{\tilde{\mu}}(K_{11} + K_{13}) - \frac{m_0\omega^2}{2\tilde{\mu}}\Big). \tag{2.34}
$$

Similarly, the flexural solution $\mathbf{u}_0 = (0,1,l,0,\alpha,\beta)^T$ reduce the 6×6 equation of motion matrix to a 4×4 one:

$$
\omega^2 \begin{pmatrix} m_0 & 0 & 0 & 0\\ 0 & m_0 & 0 & 0\\ 0 & 0 & I_0 & 0\\ 0 & 0 & 0 & I_0 \end{pmatrix} \boldsymbol{v}_0 = \begin{pmatrix} B & 0 & 0 & D\\ 0 & B & -D & 0\\ 0 & D & C & 0\\ -D & 0 & 0 & C \end{pmatrix} 2\boldsymbol{v}_0, \quad \boldsymbol{v}_0 = \begin{pmatrix} 1\\ l\\ \alpha\\ \beta \end{pmatrix}, \tag{2.35}
$$

where

$$
\begin{aligned}
B &= \tilde{\mu}\tilde{s}(\cot\tilde{s} - \csc\tilde{s}) + \lambda[2K_{11} + K_{13}(\cos\tilde{k}_x + 1)],\\
C &= \lambda[2K_{22} + K_{24}(\cos\tilde{k}_x + 1)],\\
D &= i\lambda K_{14}\sin\tilde{k}_x.
\end{aligned}
\tag{2.36}
$$

Then the dispersion relation is reduced to the determinant of a 4×4 matrix, we have

$$\begin{vmatrix} B - \frac{1}{2}m_0\omega^2 & 0 & 0 & D \\ 0 & B - \frac{1}{2}m_0\omega^2 & -D & 0 \\ 0 & D & C - \frac{1}{2}I_0\omega^2 & 0 \\ -D & 0 & 0 & C - \frac{1}{2}I_0\omega^2 \end{vmatrix} = 0. \tag{2.37}$$

The explicit form of the flexural dispersion relation is

$$\begin{aligned} &\Big(\lambda\big(2K_{11} + K_{13}(\cos\tilde{k}_x + 1)\big) + \tilde{\mu}\tilde{s}(\cot\tilde{s} - \csc\tilde{s}) - \frac{1}{2}m_0\omega^2\Big) \\ &\times \Big(\lambda\big(2K_{22} + K_{24}(\cos\tilde{k}_x + 1)\big) - \frac{1}{2}I_0\omega^2\Big) - \big(\lambda K_{14}\sin\tilde{k}_x\big)^2 = 0. \end{aligned} \tag{2.38}$$

In addition, this model also exhibits pure flexural resonances. These modes are independent of k_x and thus non-propagating (i.e. their group velocities are equal to zero). In this case, they correspond to the generalized displacement $\mathbf{u}_0 = (0, 0, 0, 1, 0, 0)^T$ which represents flexural resonances of the beams oriented in the $y-$ and $z-$directions (deflection in $x-$direction). The mode is a solution of Eq. (2.31) at resonance frequencies that satisfy

$$2\lambda(K_{22} + K_{24}) - \omega^2 I_0 = 0, \tag{2.39}$$

In our case with $I_0 = 0$, Eq. (2.39) reduces to

$$\Big(\sin\frac{\gamma l}{2}\cosh\frac{\gamma l}{2} + \cos\frac{\gamma l}{2}\sinh\frac{\gamma l}{2}\Big)\sin\frac{\gamma l}{2} = 0, \tag{2.40}$$

where γ is the flexural wavenumber of Euler beam theory. The first two lowest solutions of Eq. (2.40) are $\gamma l = 1.5000\pi$ and 2π.

2.4.2 Numerical Example

Consider a cubic lattice of 12.5 mm $\times$12.5 mm cross-section, and the length of each beam is 250 mm. The material has density $\rho = 2.7 \times 10^3$ kg/m^3, Poisson's ratio $\nu = 0.33$ and Young's modulus $E = 70$ GPa. The beams are simply connected to each other without any thickness variations or additional mass at the joints. We neglect the additional mass terms m_0 and I_0 so that the model can be easily compared with numerical simulations. The FEM simulation was done in COMSOL Multiphysics with Floquet periodic conditions imposed on the boundaries. The dispersion curves are computed by ranging k_x from 0 to

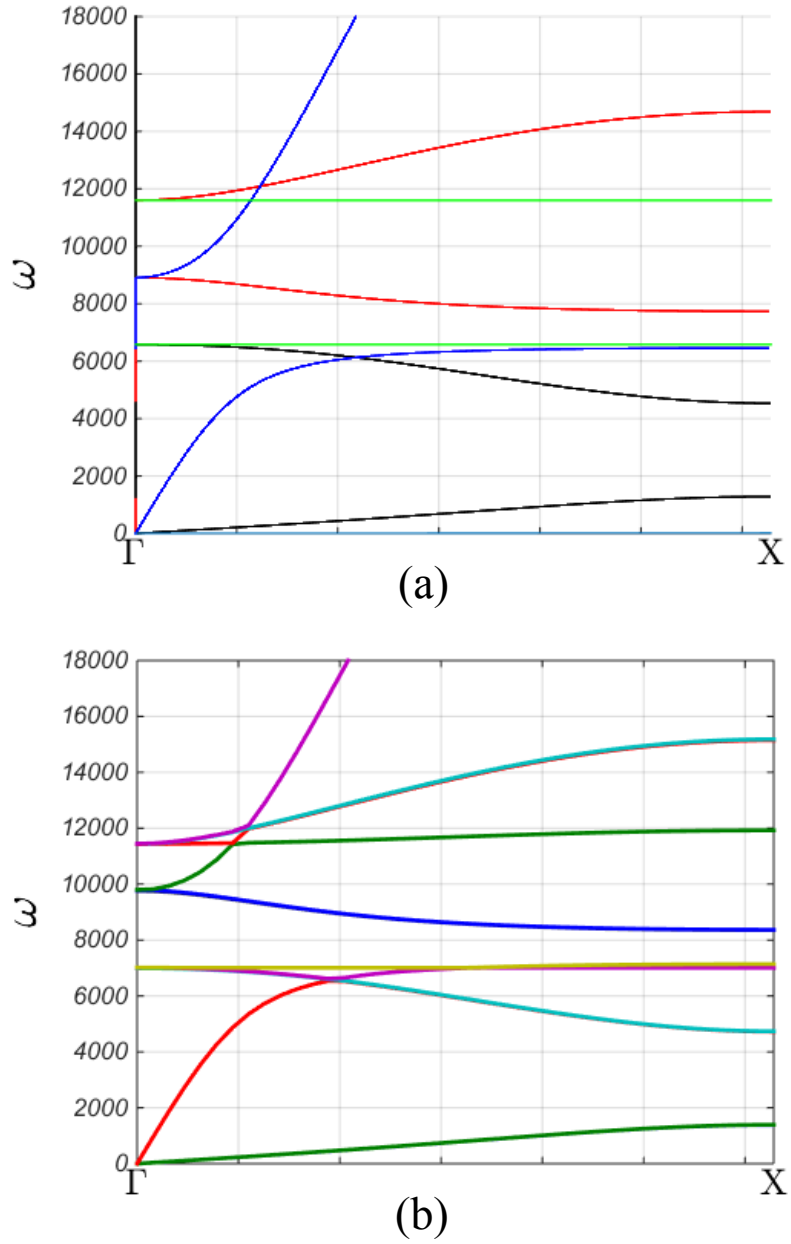

Figure 2.5: Dispersion curves of a cubic lattice comprised of square beams ($t = 12.5$ mm). (a) Computed using the semi-analytical method developed in this chapter; (b) computed using COMSOL Multiphysics. The blue lines in (a) are dispersion curves of longitudial wave, the black and red lines are dispersion curves of shear wave, and the green lines indicate represent the flexural resonances of the beams oriented in $y-$ and $z-$directions (deflection in $x-$direction).

π/l to calculate the eigenfrequencies, where π/l is half the side length of the first Irreducible Brillouin Zone. The dispersion curves are shown in Fig. 2.5. For comparison, we consider another example which changes the beam to a rod of radius $r = 6$ mm. The center mass is also assumed to be zero for simplicity. The dispersion curves are shown in Fig. 2.6.

The analytical results in Figs. 2.5 and 2.6 match well simulation results. This simplified model predicts all the eigenmodes to a remarkable degree of approximation. This agrees with our assumption that neglecting torsional modes do not affect the low frequency effective properties.

2.5 Tetrahedral Lattice

2.5.1 Dispersion relations

In this section, we consider an example of tetrahedral lattice (or diamond lattice). The unit cell of the diamond lattice is shown in Fig. 2.7a, and the Irreducible Brillouin Zone is shown in Fig. 2.7b. The dispersion relation Eq. (2.27) can be established by constructing the matrix $\mathbf{H}$ about two joints a_1 and a_2, which yields a 12 by 12 matrix system. Since $\mathbf{k} = \mathbf{k}_1 + \mathbf{k}_2 + \mathbf{k}_3 = k_1\mathbf{d}_1 + k_2\mathbf{d}_2 + k_3\mathbf{d}_3$, we can pick different combinations of k_1, k_2 and k_3 and vary the values of wave numbers to compute the dispersion curves for the diamond lattice. The system contains large matrix and various unknowns, we will need a highly efficient numerical method instead of extracting the explicit form of dispersion relations using symbolic computations.

2.5.2 Numerical Example

We consider an example for which all members are rods of radius t and have the same uniform properties. The numerical computations are based on assuming an incident wave traveling in the direction along the symmetry line of the Irreducible Brillouin Zone $\Gamma - \mathrm{L}$. In this case, we have $k_1 = k_2 = k_3$ which restricts the path of the wave vectors. The system is solved by finding the smallest eigenvalue of a positive definite matrix, and plotting the corresponding wave number and frequency of the discretized grid where the smallest eigenvalue is smaller than ϵ (a small value).

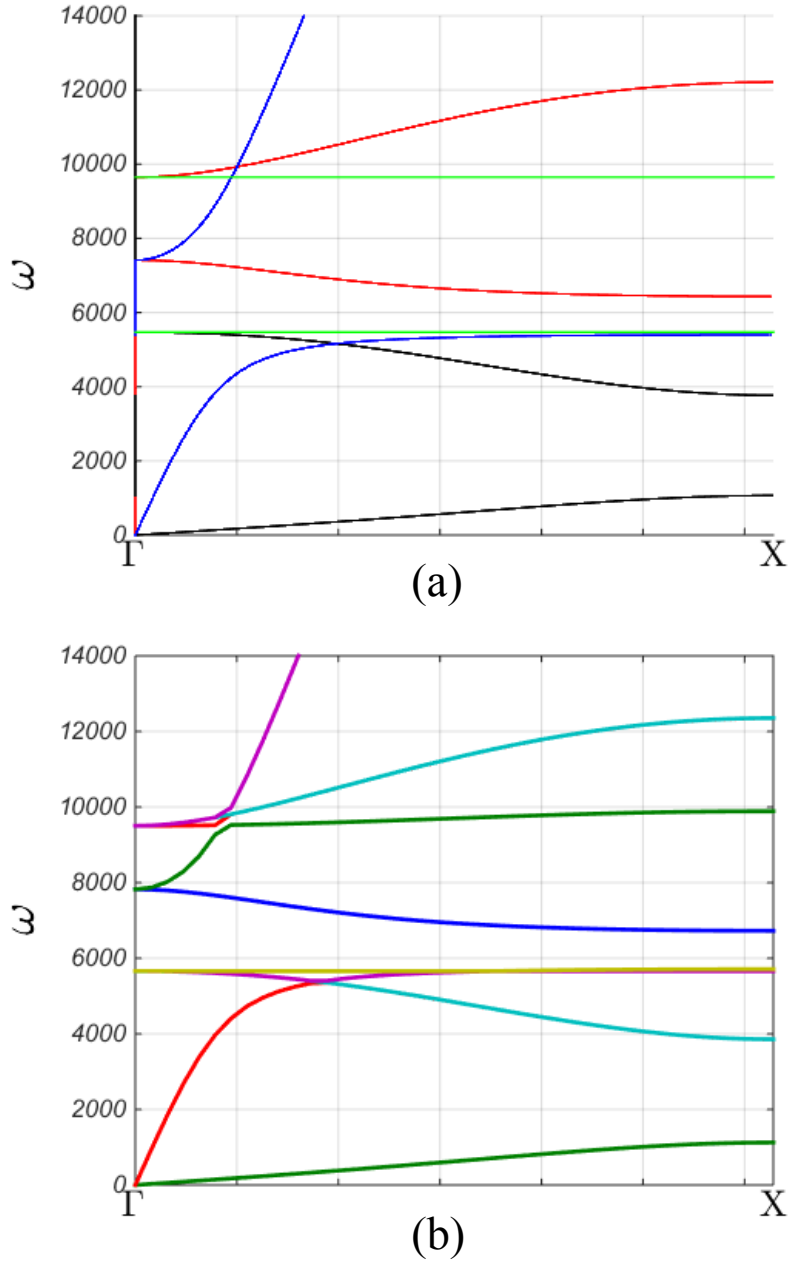

Figure 2.6: Dispersion curve of a cubic lattice comprised of circular rods ($r = 6$ mm). (a) Computed using the semi-analytical method developed in this chapter; (b) computed using COMSOL Multiphysics. The blue lines in (a) are dispersion curves of longitudial wave, the black and red lines are dispersion curves of shear wave, and the green lines indicate represent the flexural resonances of the beams oriented in $y-$ and $z-$directions (deflection in $x-$direction).

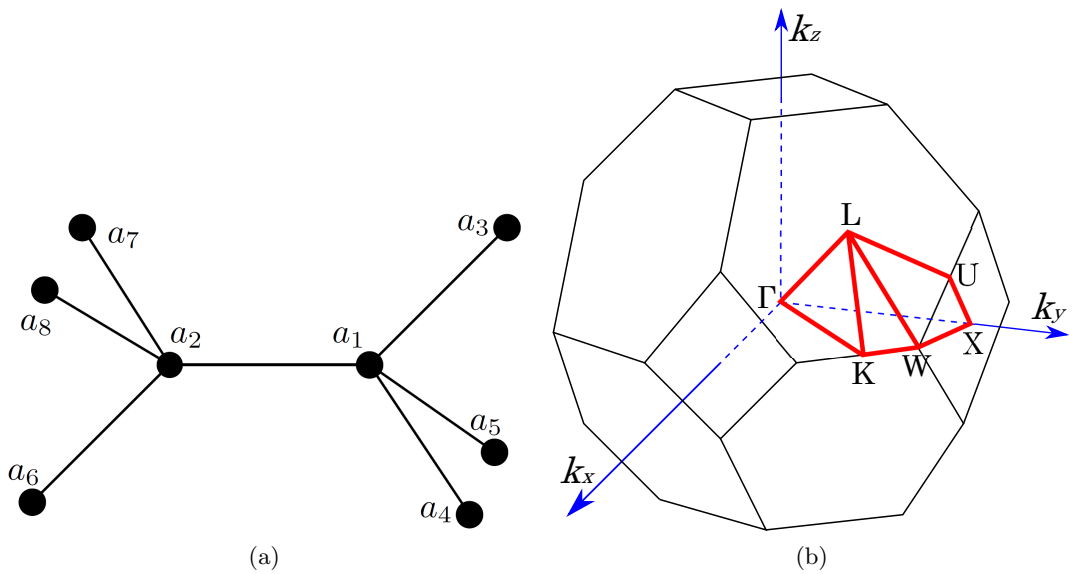

Figure 2.7: Tetrahedral (diamond) lattice. (a) The unit cell of a diamond lattice which has six mass points connected to two center masses through beam/rod members. (b) The Irreducible Brillouin Zone.

The three-dimensional diamond lattice under consideration is composed of rods with $r = 0.5$ mm circular cross-section. The length of each rod is 10 mm. The material has density $\rho = 2.7 \times 10^3$ kg/m^3, and Young's modulus $E = 70$ GPa. The center mass is taken as zero since the junction is small compared to the rods in our numerical example. For comparison, numerical simulations were done in COMSOL by imposing Floquet periodicity condition on the cross-sections of the rods and ranging the wave vector $\boldsymbol{k}$ along the symmetry line $\Gamma - \mathrm{L}$. The dispersion curves are shown in Fig. 2.8. The theoretical dispersion curves were obtained by finding the smallest eigenvalue of a positive definite matrix, and plotting the corresponding wave number and frequency of the discretized grid where the smallest eigenvalue is smaller than ε (a small value). Figure 2.8 shows that the dispersion curves computed by the present simplified theory agree well with those found using FEM. In this example, the tetrahedral lattice displays a broad frequency range with one-wave behavior: 5 to 20 kHz. The compressional wave is nearly non-dispersive, and isotropic in the homogenization regime on account of the symmetry of the lattice. This type of lattice network has potential applications in 3D acoustic metamaterial design.

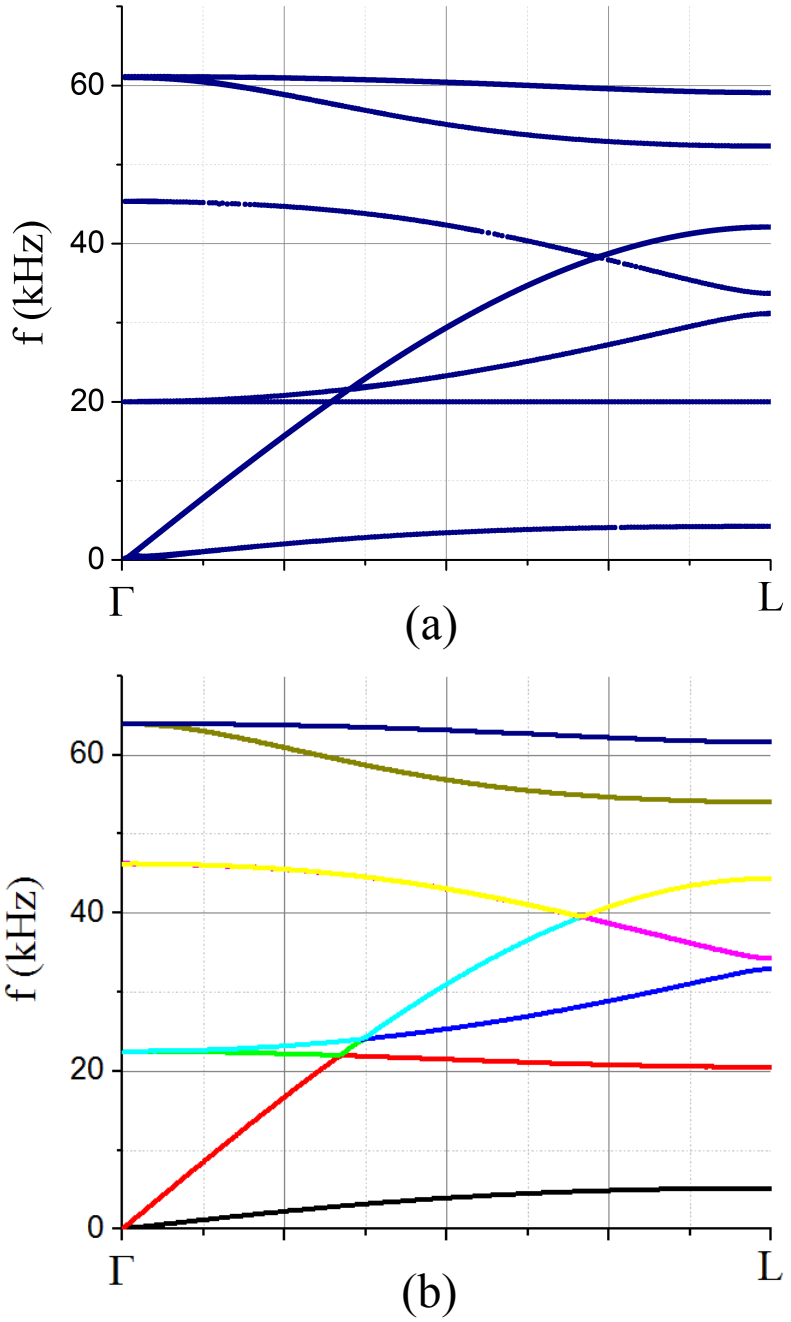

Figure 2.8: Dispersion curves of a diamond lattice comprised of circular rods ($r = 0.5$ mm). (a) Computed using the semi-analytical method developed in this chapter; (b) computed using COMSOL Multiphysics.

2.6 Dynamic homogenization of cubic lattice

2.6.1 Wave speeds in anisotropic medium of cubic symmetry

The dynamic homogenization is done by taking low frequency asymptotics of the dispersion relations and comparing with the Christoffel wave speeds in terms of the elastic moduli. Before calculating the effective moduli of cubic lattice structure, we first review wave propagation in anisotropic media. Since the cubic lattice is a cubic material, we only cover the case of cubic symmetry. The elastic constants of a cubic material in matrix form is

$$\mathbf{C} = \begin{pmatrix} C_{11} & C_{12} & C_{12} & 0 & 0 & 0 \\ C_{12} & C_{11} & C_{12} & 0 & 0 & 0 \\ C_{12} & C_{12} & C_{11} & 0 & 0 & 0 \\ 0 & 0 & 0 & C_{66} & 0 & 0 \\ 0 & 0 & 0 & 0 & C_{66} & 0 \\ 0 & 0 & 0 & 0 & 0 & C_{66} \end{pmatrix}, \tag{2.41}$$

where C_{11}, C_{12}, and C_{66} are independent of each other.

Using index notation, the well-known Christoffel equation of motion is given by Eq. (7.1.3b) in Ref. [63] as

$$\left(C_{ijkl} n_j n_l - \rho c^2 \delta_{ik}\right) \mathbf{p}_k = 0, \tag{2.42}$$

where δ_{ik} is kronecker delta, c is the wave speed, and $\mathbf{p}_k$ are the eigenvectors (displacements) corresponding to the eigenvalues which are roots of

$$\det\left(C_{ijkl} n_j n_l - \rho c^2 \delta_{ik}\right) = 0. \tag{2.43}$$

Specifically, for elastic medium of cubic symmetry Eq. 2.43 has the form

$$\begin{vmatrix} \Gamma_{11} - \rho c^2 & \Gamma_{12} & \Gamma_{13} \\ \Gamma_{12} & \Gamma_{22} - \rho c^2 & \Gamma_{23} \\ \Gamma_{13} & \Gamma_{23} & \Gamma_{33} - \rho c^2 \end{vmatrix} = 0, \tag{2.44}$$

where

$$\begin{aligned}
\Gamma_{11} &= n_1^2 C_{11} + n_2^2 C_{66} + n_3^2 C_{66}, \\
\Gamma_{22} &= n_1^2 C_{66} + n_2^2 C_{11} + n_3^2 C_{66}, \\
\Gamma_{33} &= n_1^2 C_{66} + n_2^2 C_{66} + n_3^2 C_{11}, \\
\Gamma_{12} &= n_1 n_2 (C_{12} + C_{66}).
\end{aligned} \tag{2.45}$$

The combinations of the parameters n_1, n_2 and n_3 are used to indicate the direction of wave propagation. For evaluating the three elastic constants of a cubic material, it is sufficient to consider only two directions ((100) and (110)) as we explain in the following.

Wave propagation in (100) **direction.**

We now derive the wave speeds along one of the three principal axes of the cubic material. In this case, we have $n_1 = 1$ and $n_2 = n_3 = 0$. Plugging these values into Eq. (2.45) then into Eq. (2.44), we have

$$\begin{vmatrix} C_{11} - \rho c^2 & 0 & 0 \\ 0 & C_{66} - \rho c^2 & 0 \\ 0 & 0 & C_{66} - \rho c^2 \end{vmatrix} = 0, \tag{2.46}$$

which can be simplified as

$$(C_{11} - \rho c^2)(C_{66} - \rho c^2)^2 = 0, \tag{2.47}$$

then the eigenvalues, i.e. wave speeds, are

$$\begin{aligned}
c_1 &= \sqrt{\frac{C_{11}}{\rho}}, \\
c_2 = c_3 &= \sqrt{\frac{C_{66}}{\rho}},
\end{aligned} \tag{2.48}$$

where c_1 is the pure longitudinal wave speed in (100) direction; c_2 and c_3 are speeds of pure shear wave with different polarizations.

Wave propagation in (110) **direction.**

Next, we derive the wave speeds along the in-plane diagonal direction. Similarly, we have $n_1 = n_2 = 1/\sqrt{2}$ and $n_3 = 0$. Plugging these values into Eq. (2.45) then into Eq. (2.44),

we have

$$\begin{vmatrix} \frac{1}{2}(C_{11}+C_{66})-\rho c^2 & \frac{1}{2}(C_{12}+C_{66}) & 0 \\ \frac{1}{2}(C_{12}+C_{66}) & \frac{1}{2}(C_{11}+C_{66})-\rho c^2 & 0 \\ 0 & 0 & C_{66}-\rho c^2 \end{vmatrix} = 0, \tag{2.49}$$

this equation can be rewritten as

$$[(C_{11}+C_{66}-2\rho c^2)^2-(C_{12}+C_{66})^2](C_{66}-\rho c^2)=0, \tag{2.50}$$

then the eigenvalues are

$$\begin{aligned} c_1' &= \sqrt{\frac{C_{11}+C_{12}+2C_{66}}{2\rho}}, \\ c_2' &= \sqrt{\frac{C_{11}-C_{12}}{2\rho}}, \\ c_3' &= \sqrt{\frac{C_{66}}{\rho}}, \end{aligned} \tag{2.51}$$

where c_1' is pure longitudinal wave speed in (110) direction, while c_2' and c_3' are speeds of pure shear wave in $(1\bar{1}0)$ and (001) direction, respectively. This is more complicated than the (100) case since there are different shear wave speeds corresponding to different polarizations involved.

2.6.2 Dynamic derivation of effective moduli of cubic lattice

The wave speeds in solids are expressed in terms of the elastic moduli as we discussed above. Then we can relate the low frequency asymptotics of the dispersion relations of the cubic lattice to the wave speeds. The dispersion relations are frequency ω as a function of wave number $\mathbf{k}$, therefore the low frequency asymptotics have the form

$$c(\mathbf{d}) = \lim_{k\to 0}\frac{\omega(\mathbf{k})}{k}, \quad \mathbf{k}=k\mathbf{d}, \quad |\mathbf{d}|=1. \tag{2.52}$$

Then the elastic moduli can be retrieved by relating the wave speeds derived using these two methods. The calculation of the low frequency asymptotics are simply the Taylor series expansion of the dispersion relations at $k=0$. By canceling the high order terms of k, we can obtain explicit forms of wave speeds in terms of the solid material properties and geometric parameters.

Wave propagation in (100) **direction.**

The equations of motion of cubic lattice are derived in Sec. 2.4, as well as the dispersion relations for (100) case. Here we use Eqs. (2.34) and (2.38) to derive the low frequency wave speeds. Using Eq. (2.11) and neglecting high order derivatives, the Taylor series expansion of the longitudinal mode Eq. (2.34) is

$$(1-\frac{\tilde{k}^2}{2}+\cdots)=(1-\frac{\tilde{s}^2}{2}+\cdots)+(1-\frac{\tilde{s}^2}{6}+\cdots)\frac{1}{2\tilde{\mu}}\Big(4\lambda(-\frac{\gamma^4 l}{2}-\cdots)-m_0\omega^2\Big). \tag{2.53}$$

Since $\tilde{k}=\tilde{k}_x$, we can expand this equation and substitute ω by $c_1 k$. Then rearrange the equation and write the longitudinal wave speed in (100) direction as

$$c_1=\sqrt{\frac{EAl}{3\rho Al+m_0}}. \tag{2.54}$$

As a check of this expression, we use the same geometry and material properties used in the example in Sec. 2.4. The wave speed calculated using Eq. (2.54) is $c_1 = 2915.53$ m/s. For comparison, we pick a point at low frequency range, e.g., $(0.004068, 11.86)$, the wave speed calculated from the band structure is $c_1 = 2915.44$ m/s. It is clear that these two results match very well.

Now we consider the flexural mode in (100) direction. Following similar procedure, the Taylor series expansion of Eq. (2.38) is

$$\begin{aligned}\Big[\lambda\big(2(\frac{12}{l^3}-\frac{13l}{35}\gamma^4-\cdots)+(-\frac{12}{l^3}-\frac{9l}{70}\gamma^4-\cdots)(2-\frac{\tilde{k}^2}{2}+\cdots)\big)+\tilde{\mu}(-\frac{\tilde{s}^2}{2}+\cdots)\\ -\frac{1}{2}m_0\omega^2\Big]\big(2\lambda(\frac{4}{l}-\cdots+\frac{2}{l}+\cdots)-0\big)-\big(\lambda(\frac{6}{l^2}+\cdots)(\tilde{k}-\cdots)\big)^2=0.\end{aligned} \tag{2.55}$$

We expand this equation and substitute ω by $c_2 k$. Then rearrange the equation and write the shear wave speed in (100) direction as

$$c_2=\sqrt{\frac{6EI}{3\rho Al^2+m_0 l}}. \tag{2.56}$$

The shear wave speed calculated using Eq. (2.56) is $c_2 = 103.08$ m/s. Taking the point $(0.01437, 1.481)$ on the dispersion curve, the shear wave speed evaluated at this point is $c_2 = 103.06$ m/s which agrees to our prediction.

Comparing Eqs. (2.54) and (2.56) with Eq. (2.48), we have the effective moduli

$$\begin{aligned} C_{11} &= \frac{EAl\rho_{\text{eff}}}{3\rho Al + m_0}, \\ C_{66} &= \frac{6EI\rho_{\text{eff}}}{3\rho Al^2 + m_0 l}, \end{aligned} \tag{2.57}$$

where E and ρ are the Young's modulus and density of the material respectively, ρ_{eff} is the effective density of the lattice structure, m_0 is the center mass, A, r and l are the cross-section area, radius and full length of the beam/rod, respectively. The moment of inertia I depends on the shape of beam/rod.

Wave propagation in (110) **direction.**

The elastic constants C_{11} and C_{66} are derived in last section. There is only one more elastic constant to be investigated, therefore we only need to consider the longitudinal mode propagating in (110) direction since C_{12} appears in the expression for c_1' in Eq. (2.51). In this case, we have $\tilde{\mathbf{k}} = \tilde{k}_x \mathbf{d}_1 + \tilde{k}_y \mathbf{d}_2$ and $\tilde{k}_z = 0$. Setting $\tilde{k}_x = \tilde{k}_y = \frac{1}{\sqrt{2}}\tilde{k}$ and considering the pure-longitudinal solution $\mathbf{u}_0 = (1, 1, 0, 0, 0, 0)^T$ to Eq. (2.31), we have

$$\begin{vmatrix} \tilde{\mu}\tilde{s}(\cot\tilde{s} - \csc\tilde{s}\cos\tilde{k}_x) + A_1 - \frac{1}{2}m_0\omega^2 & 0 \\ 0 & \tilde{\mu}\tilde{s}(\cot\tilde{s} - \csc\tilde{s}\cos\tilde{k}_y) + A_2 - \frac{1}{2}m_0\omega^2 \end{vmatrix} = 0, \tag{2.58}$$

which yields two identical solutions. Substituting $\tilde{k}_x$ and $\tilde{k}_y$ by $\frac{1}{\sqrt{2}}\tilde{k}$, the longitudinal dispersion relation can be written as

$$\tilde{\mu}\tilde{s}\big(\cot\tilde{s} - \csc\tilde{s}\cos(\frac{1}{\sqrt{2}}\tilde{k})\big) + \lambda(K_{11} + K_{13}) + \lambda\big(K_{11} + K_{13}\cos(\frac{1}{\sqrt{2}}\tilde{k})\big) - \frac{1}{2}m_0\omega^2 = 0. \tag{2.59}$$

The Taylor series expansion of this equation at $k = 0$ is

$$\begin{aligned} &\tilde{\mu}\big[(1 - \frac{\tilde{s}^2}{2} + \cdots) - (1 - \frac{\tilde{k}^2}{4} + \cdots)\big] + \lambda\big[(\frac{12}{l^3} - \frac{13l}{35}\gamma^4 - \cdots) + (-\frac{12}{l^3} - \frac{9l}{70}\gamma^4 - \cdots)\big] \\ &\quad + \lambda\big[(\frac{12}{l^3} - \frac{13l}{35}\gamma^4 - \cdots) + (-\frac{12}{l^3} - \frac{9l}{70}\gamma^4 - \cdots)(1 - \frac{\tilde{k}^2}{4} + \cdots)\big] - \frac{1}{2}m_0\omega^2 = 0. \end{aligned} \tag{2.60}$$

Expanding this equation and substituting ω by $c_1'k$, we can rearrange each term and write the longitudinal wave speed in (110) direction as

$$c_1' = \sqrt{\frac{EAl^2 + 12EI}{6\rho Al^2 + 2m_0 l}}, \tag{2.61}$$

which corresponds to the c_1' in Eq. (2.51). Using Eq. (2.57), we have

$$C_{12} = 0. \tag{2.62}$$

$C_{12} = 0$ indicates that Poisson's ratio $\nu_{12} = 0$ which can be interpreted as applying a displacement in (100) direction does not cause deformation in (010) direction.

Effective bulk modulus

Since we have obtained all the three elastic constants, there is no need to consider wave propagation in (111) direction. In anisotropic media of cubic symmetry, the effective bulk modulus is

$$\kappa_{\text{eff}} = \frac{C_{11} + 2C_{12}}{3} = \frac{EAl\rho_{\text{eff}}}{9\rho Al + 3m_0}. \tag{2.63}$$

The approximate total mass of the cubic lattice is $m \approx 3\rho Al + m_0$ (if $l \gg r$), i.e. the center mass and the mass of rods without considering the intersection of them. Hence, the effective density is

$$\rho_{\text{eff}} \approx \frac{3\rho Al + m_0}{l^3}. \tag{2.64}$$

Then the elastic constants reduce to

$$\begin{aligned} C_{11} &= \frac{EA}{l^2}, \\ C_{12} &= 0, \\ C_{66} &= \frac{6EI}{l^4}, \end{aligned} \tag{2.65}$$

the bulk modulus reduce to

$$\kappa_{\text{eff}} = \frac{EA}{3l^2}, \tag{2.66}$$

where I is the area moment of inertia (for a beam $I = bt^3/12$ and for a rod $I = \pi r^4/4$). In particular, the bulk modulus of a cubic lattice comprised of rods is

$$\kappa_{\text{eff}} = \frac{E\pi r^2}{12R^2}, \tag{2.67}$$

where R is half length of the rod. The expression for the effective bulk modulus agrees to Ref. [64]. For convenience, we introduce a new parameter α defined as the ratio of R to r, i.e. $\alpha = R/r$, to show the tendency of bulk modulus. Figure 2.9 gives prediction of effective bulk modulus versus α. The ratio α suggests that 1080 carbon steel is a proper choice for matching properties to water since thin beam theory is used in our model.

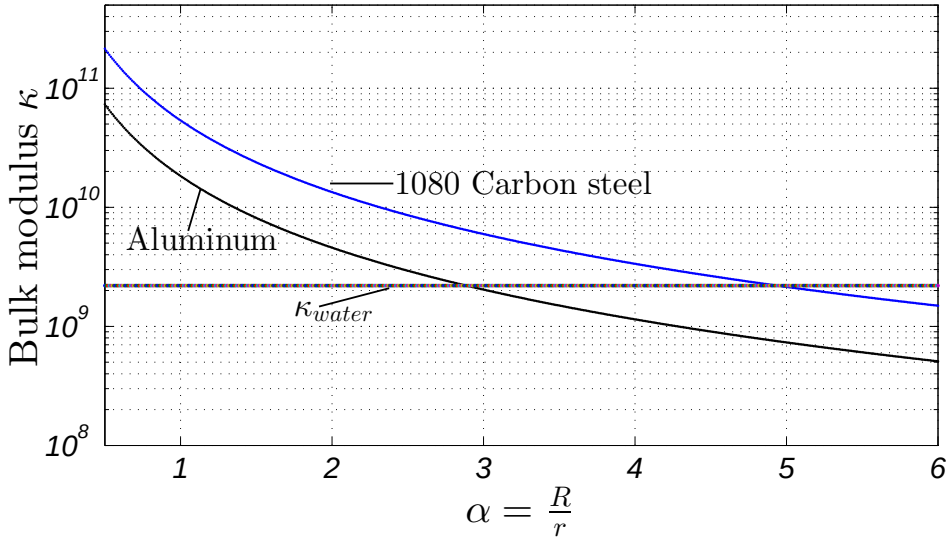

Figure 2.9: Effective bulk modulus versus α. The horizontal solid line represents the bulk modulus of water.

2.6.3 Designing metal water using cubic lattice

Our goal here is to tune the effective bulk modulus and density similar to water, so that the sound speed and impedance are matched to water. The bulk modulus of water is $\kappa_{\text{water}} = 2.2$ GPa, density is $\rho_{\text{water}} = 1.0 \times 10^3$ kg/m^3. Figure 2.9 shows that the ratio α is relatively bigger when 1080 carbon steel is used as the material. For this reason, we use 1080 carbon steel with Young's modulus $E = 205$ GPa, density $\rho = 7.87 \times 10^3$ kg/m^3 as the material for both center mass and rods. Setting $\kappa_{\text{eff}} = \kappa_{\text{water}}$ and applying Eq. 2.67, we have

$$\alpha = \frac{R}{r} = 4.93912. \tag{2.68}$$

The radius of the rod is chosen as $r = 4$ mm, then the length of the rod is $l = 39.5$ mm. Equation (2.64) indicates that the additional center mass is

$$m_0 = \rho_{\text{water}} l^3 - 3\rho A l = 14.7525\ g. \tag{2.69}$$

Note that by adding more mass to the joints, the stiffness of the lattice is also increased. The results derived in this section may help with designing the initial parameter set, then FEM based homogenization methods can be employed to optimize the structure.

2.7 Discussion

To the author's knowledge, this chapter is the first theoretical work studying the band diagrams using beam theories for 3D lattices. Dynamic modeling of and 3D lattices can be accurately modeled using a low order model with minimal degrees of freedom described by thin beam members. The dispersion relations for cubic lattice has been derived analytically by imposing the Bloch-Floquet periodicity condition, yielding an Hermitian eigenvalue problem for the unknown frequencies. Numerical methods were used to compute the band diagrams for tetrahedral lattice. The semi-analytical approach allowed us to extract the low frequency asymptotics. In particular, the closed-form explicit expressions for the Christoffel matrix in the *quasi-static* regime for cubic lattice was presented. Numerical comparisons of wave dispersion diagrams with FEM simulations indicate that the beam model provides good accuracy for lower modes. The semi-analytical nature of the present model makes it the natural extension of purely static methods for periodic lattice structures, e.g. [65]. In summary, our beam model provides a novel and fast approach to calculate the band-diagrams for 3D lattices. This semi-analytical method may prove useful in designing phononic crystals and pentamode structures.

Chapter 3

Extraordinary acoustic transmission through slanted gratings

Acoustic metamaterial devices usually suffer from low transmission due to impedance mismatch between the exterior acoustic medium and the metamaterial slab, especially the space-coiling or labyrinthine structures [66, 67, 68]. The zigzag channels are designed to achieve phase delay for various applications. However, the folded channel also brings impedance mismatch which significantly affects the performance of the devices. Researchers have been trying to improve the transmission for these devices in the past a few years [69, 70]. It is found that the impedance of the unit cells can be matched to the exterior medium under certain conditions [71]. In this chapter, we will focus on the acoustic transmission through slanted gratings, as well as zigzag structures, and provide a prediction of the so-called intromission angle $\pm\theta_i$ for total acoustic transmission.

Total transmission through 1D grating with narrow apertures can be achieved by taking advantage of Fabry-Pérot resonance [72]. However, it is only a narrow band effect because the enhancement is induced by resonance. Broadband extraordinary optical transmission (EOT) has been recently proposed [73] and realized [74] based on a Brewster angle effect that results from the effective low-frequency properties of the grating. Broadband extraordinary acoustic transmission (EAT) can be achieved with similar idea. The physics behind EAT is, as explained by D'Aguanno *et al.* [75], broadband impedance matching. The grating has low frequency effective properties easily estimated for rigid grating elements, which allows to achieve the desired intromission angle by tuning the grating porosity [75]. Maurel *et al.* [76] also provide a clear analysis of this problem as impedance matching but by means of acoustic fluids with anisotropic inertia. In this chapter, we take a step further to analyze the obliquely oriented gratings and provide explicit formula for intromission angle. We show that total transmission is achieved at incidence angles $\pm\theta_i$ with a relative phase shift. This

broadband EAT phenomenon holds for any slab thickness as long as the slab unit structure is subwavelength. The results derived in this chapter not only work for slanted gratings, but also work for the zigzag structure similar to that in Ref. [69], since the zigzag elements can be considered as slanted grating elements with alternating orientations. A few new simulation examples are presented to demonstrate the theoretical development.

This chapter is organized as follows. The governing equations of acoustic transmission through a slab of anisotropic inertia are presented in Sec. 3.1. The solutions of transmission and reflection coefficients are derived in Sec. 3.2. In Sec. 3.3, the results from previous section is employed to predict the intromission angle of a slanted single-layer grating (SLG). The results are then simplified and applied to various cases. Numerical examples are shown in Sec. 3.4 to demonstrate the theoretical results.

3.1 Governing equations

We consider acoustic transmission through a slab with anisotropic inertia as shown in Fig. 3.1. The blue region is the equivalent uniform anisotropic layer, the surrounding acoustic medium has density ρ and sound speed c with bulk modulus $K = \rho c^2$. The equation of continuity and equation of motion can be written in terms of scalar pressure p and vector velocity $\boldsymbol{v}$ as

$$\begin{aligned} \boldsymbol{v} &= (i\omega\rho)^{-1}\nabla p, \\ p &= (i\omega)^{-1}K\nabla\cdot\boldsymbol{v}, \end{aligned} \tag{3.1}$$

where the time harmonic dependence $e^{-i\omega t}$ is assumed to be understood. The acoustic pressure in the exterior acoustic medium is

$$p = p_0\, e^{ik\sin\theta\, x_2} \times \begin{cases} \left(e^{ik\cos\theta\, x_1} + Re^{-ik\cos\theta\, x_1}\right) & x_1 \le 0, \\ Te^{ik\cos\theta(x_1-b)} & x_1 \ge b, \end{cases} \tag{3.2}$$

where $k = \omega/c$ is the wavenumber, p_0 is a constant. The acoustic impedance is defined as

$$Z_\theta = \frac{\rho c}{\cos\theta}. \tag{3.3}$$

The single-layer two-dimensional anisotropic slab of thickness b has bulk modulus K_s and anisotropic density represented by a 2×2 symmetric tensor ($\boldsymbol{\rho} = \boldsymbol{\rho}^T$) with elements

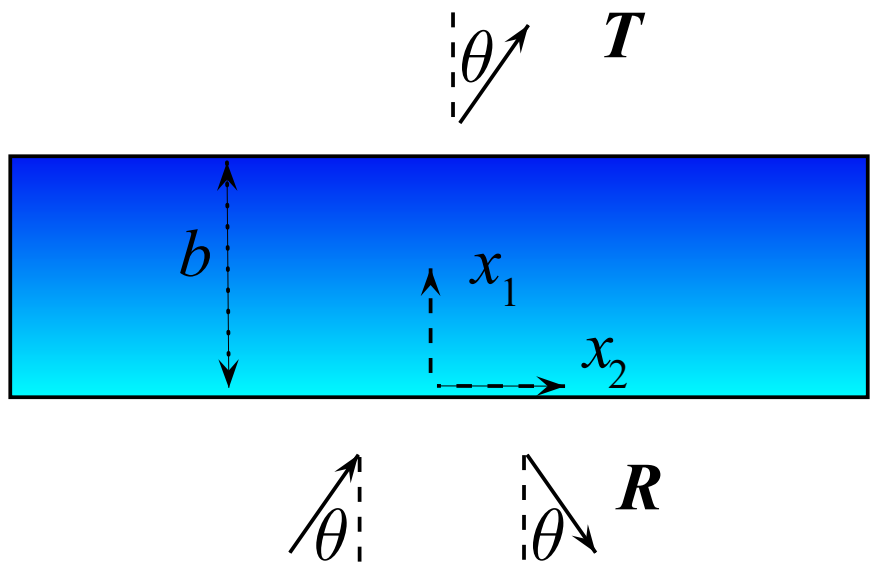

Figure 3.1: Equivalent homogeneous slab with anisotropic density.

ρ_{ij}, $i, j = 1, 2$. The equation of continuity and equation of motion within the slab are

$$\begin{aligned} \boldsymbol{v} &= (i\omega\boldsymbol{\rho})^{-1}\nabla p, \\ p &= (i\omega)^{-1}K_s\nabla\cdot\boldsymbol{v}, \end{aligned} \tag{3.4}$$

3.2 Solution for an anisotropic inertial slab

We first define the state vector

$$\boldsymbol{u} = \begin{pmatrix} v_1 \\ -p \end{pmatrix}, \tag{3.5}$$

and consider solutions with constant horizontal phase such that the state vector $\boldsymbol{u}$ has the form

$$\boldsymbol{u}(x_1,\ x_2) = \boldsymbol{U}(x_1)e^{ik\sin\theta x_2}, \tag{3.6}$$

then $\boldsymbol{U}(x_1)$ satisfies

$$\frac{d\boldsymbol{U}}{dx_1} = i\omega\boldsymbol{A}\boldsymbol{U}, \tag{3.7}$$

where

$$\boldsymbol{A} = \frac{\sin\theta}{c}\frac{\rho_{12}}{\rho_{22}}\boldsymbol{I} - \boldsymbol{B},\ \boldsymbol{B} = \begin{pmatrix} 0 & \frac{1}{K_s} - \frac{\sin^2\theta}{c^2\rho_{22}} \\ \frac{\det\boldsymbol{\rho}}{\rho_{22}} & 0 \end{pmatrix}, \tag{3.8}$$

where $\boldsymbol{I}$ is identity. It is easy to find that the matrix $\boldsymbol{A}$ is independent of ω.

The propagator matrix $\boldsymbol{M}(x)$ is defined for later use as the solution of the differential equation

$$\frac{d\boldsymbol{M}(x)}{dx} = i\omega \boldsymbol{A}\boldsymbol{M}, \text{ with } \boldsymbol{M}(0) = \boldsymbol{I}, \tag{3.9}$$

where $\boldsymbol{M}$ has the property that $\det \boldsymbol{M} = 1$ [77]. The Hermitian conjugate satisfies $\boldsymbol{M}^\dagger = \boldsymbol{J}\boldsymbol{M}^{-1}\boldsymbol{J}$ because of the property $\boldsymbol{A}^T = \boldsymbol{J}\boldsymbol{A}\boldsymbol{J}$, where the 2×2 matrix $\boldsymbol{J}$ has zeros on the diagonal and unity off diagonal. Therefore we have $\boldsymbol{M}^{-1}(x) = \boldsymbol{J}\boldsymbol{M}^\dagger(x)\boldsymbol{J} = \boldsymbol{M}(-x)$.

We assume that the anisotropic slab has uniform properties in $x \in [0,\ b]$, so that

$$\boldsymbol{M}(b) = e^{i\omega b \boldsymbol{A}}. \tag{3.10}$$

Using Eqs. (3.8) and (3.10), we have the explicit propagator matrix

$$\boldsymbol{M}(b) = \Big(\cos\frac{\omega b}{c_\theta}\boldsymbol{I} - \frac{i}{c_\theta}\sin\frac{\omega b}{c_\theta}\boldsymbol{B}\Big)^{ikb\frac{\rho_{12}}{\rho_{22}}\sin\theta}, \tag{3.11}$$

where $c_\theta = (-\det \boldsymbol{B})^{-1/2}$, $c_\theta^{-1}\boldsymbol{B}$ is a square root of the identity.

Equations. (3.2) and (3.6) give

$$\boldsymbol{U}(0-) = p_0 \begin{pmatrix} Z_\theta^{-1}(1-R) \\ -1-R \end{pmatrix}, \ \boldsymbol{U}(b+0) = p_0 T \begin{pmatrix} Z_\theta^{-1} \\ -1 \end{pmatrix}. \tag{3.12}$$

The boundary conditions are continuity of normal velocity v_1 and pressure p at $x_1 = 0$ and $x_1 = b$, i. e. $\boldsymbol{U}(0+) = \boldsymbol{U}(0-)$ and $\boldsymbol{U}(b+0) = \boldsymbol{U}(b-0)$. Hence,

$$T \begin{pmatrix} Z_\theta^{-1} \\ -1 \end{pmatrix} = \begin{pmatrix} M_{11} & M_{12} \\ M_{21} & M_{22} \end{pmatrix} \begin{pmatrix} Z_\theta^{-1}(1-R) \\ -1-R \end{pmatrix}. \tag{3.13}$$

Then we can solve for the transmission and reflection coefficients

$$\begin{aligned} T &= 2(M_{11} + M_{22} + Z_\theta M_{12} + Z_\theta^{-1} M_{21})^{-1}, \\ R &= 1 - (M_{22} + Z_\theta M_{12})T. \end{aligned} \tag{3.14}$$

3.2.1 Extraordinary acoustic transmission

Using explicit solution for $\boldsymbol{M}(b)$ from Eq. (3.11) yield the explicit form of transmission and reflection coefficients

$$\begin{aligned} T &= e^{-ikb\frac{\rho_{12}}{\rho_{22}}\sin\theta}\Big(\cos\frac{\omega b}{c_\theta} - \frac{i}{2}\Big(\frac{Z_\theta}{Z'_\theta} + \frac{Z'_\theta}{Z_\theta}\Big)\sin\frac{\omega b}{c_\theta}\Big)^{-1}, \\ R &= \frac{i}{2}\Big(\frac{Z_\theta}{Z'_\theta} - \frac{Z'_\theta}{Z_\theta}\Big)\sin\frac{\omega b}{c_\theta}\Big(\cos\frac{\omega b}{c_\theta} - \frac{i}{2}\Big(\frac{Z_\theta}{Z'_\theta} + \frac{Z'_\theta}{Z_\theta}\Big)\sin\frac{\omega b}{c_\theta}\Big)^{-1}, \end{aligned} \tag{3.15}$$

where

$$c_\theta = \Big(\frac{\rho_{22}}{\det \boldsymbol{\rho}}\Big)^{\frac{1}{2}}\Big(\frac{1}{K_s} - \frac{\sin^2\theta}{c^2\rho_{22}}\Big)^{-\frac{1}{2}}, \quad Z'_\theta = \Big(\frac{\det \boldsymbol{\rho}}{\rho_{22}}\Big)c_\theta. \tag{3.16}$$

The results discussed in this chapter differ from the results exist in the literature, e.g. Maurel *et al.* [76] only considered a special case in which $\phi = 0$. In other words, the acoustic fluid inside the slab corresponds to $\rho_{11} = \rho_{22}$, $\rho_{12} = 0$. It is easy to show that

$$|T(-\theta)| = |T(\theta)|, \; R(-\theta) = R(\theta). \tag{3.17}$$

From Eq. (3.17), we find that the magnitude of the transmission coefficient is symmetric about $\theta = 0$, while both magnitude and phase of the reflection coefficient are symmetric about $\theta = 0$. Therefore, the asymmetry can be expressed as a function of θ as

$$\frac{T(-\theta)}{T(\theta)} = e^{i2kb\frac{\rho_{12}}{\rho_{22}}\sin\theta}. \tag{3.18}$$

Equation (3.15) implies $|T| = 1$ when the impedance is matched, i.e. $|T(\theta_i)| = 1 \Leftrightarrow Z_\theta = Z'_\theta$. Therefore, the condition for extraordinary acoustic transmission is

$$\rho^2\sin^2\theta_i + (\det\boldsymbol{\rho})\cos^2\theta_i = \frac{K}{K_s}\rho\rho_{22}, \tag{3.19}$$

where θ_i is the intromission angle at which transmission equals to unity. It is clear that the intromission angle is symmetric with respect to the normal of the interface between the exterior medium and the slab, i.e. $|T(\pm\theta_i)| = 1$.

3.3 Single-layer gratings as anisotropic inertial slabs

The single-layer grating considered in this section is depicted in Fig. 3.2. The grating elements have properties bulk modulus K_0 and density ρ_0. The volume fraction of the grating fluid is $f \in [0,\ 1]$. The effective bulk modulus and density tensor are denoted by K_s and $\boldsymbol{\rho}$ respectively. We consider first the symmetric case when $\phi = 0$. The effective properties of the slab are obtained using *quasi-static* homogenization as

$$\begin{aligned} \frac{1}{K_s} &= \frac{f}{K_0} + \frac{1-f}{K}, \; \boldsymbol{\rho} = \begin{pmatrix} \rho_1 & 0 \\ 0 & \rho_2 \end{pmatrix}, \\ \frac{1}{\rho_1} &= \frac{f}{\rho_0} + \frac{1-f}{\rho}, \; \rho_2 = f\rho_0 + (1-f)\rho. \end{aligned} \tag{3.20}$$

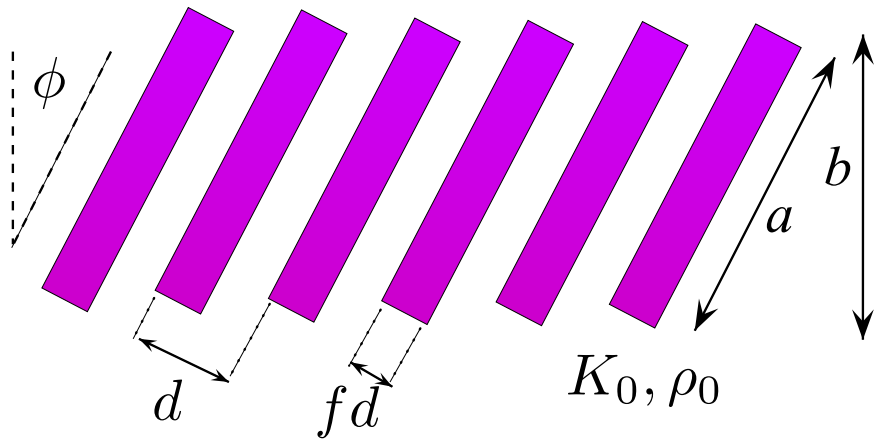

Figure 3.2: The obliquely aligned single-layer grating.

The single-layer grating rotated by an angle ϕ (non-zero) has the same effective bulk modulus K_s as the $\phi = 0$ case. However, the density tensor becomes non-diagonal but still symmetric:

$$\boldsymbol{\rho} = \begin{pmatrix} \rho_{11} & \rho_{12} \\ \rho_{21} & \rho_{22} \end{pmatrix}, \quad \begin{aligned} \rho_{11} &= \rho_1 \cos^2\phi + \rho_2 \sin^2\phi, \\ \rho_{22} &= \rho_1 \sin^2\phi + \rho_2 \cos^2\phi, \\ \rho_{12} &= (\rho_1 - \rho_2)\sin\phi\cos\phi \ \big(= \rho_{21}\big). \end{aligned} \tag{3.21}$$

Note that $\rho_{11},\ \rho_{22} > 0$. It is hard to tell whether ρ_{12} is positive or negative from Eq. (3.21), we rewrite it as

$$\rho_{12} = -\frac{f(1-f)(\rho-\rho_0)^2}{f\rho + (1-f)\rho_0}\sin\phi\cos\phi. \tag{3.22}$$

Equation (3.22) implies

$$\begin{cases} \rho_{12} < 0 & \text{if } \phi > 0, \\ \rho_{12} > 0 & \text{if } \phi < 0, \\ \rho_{12} = 0 & \text{if } \phi = 0. \end{cases} \tag{3.23}$$

An interesting phenomena is that $\det \boldsymbol{\rho} = \rho_1\rho_2$ and $\mathrm{tr}\boldsymbol{\rho} = \rho_1 + \rho_2$ regardless of the rotation angle ϕ. The relation between the transmission coefficients for incidence at $\pm\theta$ becomes

$$\frac{T(-\theta)}{T(\theta)} = e^{-i2ka\sin\phi\sin\theta\left(\frac{\rho_2-\rho_1}{\rho_2+\rho_1\tan^2\phi}\right)}. \tag{3.24}$$

Using the explicit form of the density tensor, $|T(\theta_i)| = 1$ leads to

$$\cos^2(\theta_i) = \frac{\left(\frac{\rho_2-\rho_1}{\rho}\cos^2\phi + \frac{\rho_1}{\rho}\right)\frac{K}{K_s} - 1}{\frac{\rho_1\rho_2}{\rho^2} - 1}. \tag{3.25}$$

This relation for intromission angle shows the explicit dependence on the orientation angle ϕ. In particular, this implies that $\partial\theta_i/\partial\phi > 0$ since $\rho_-\rho_1 > 0$ and $\rho_1\rho_2 > \rho^2$ for $\rho_0 \neq \rho$.

Now we consider the behavior for several limiting cases, such as rigid grating elements. The case of orientation angle $\phi = 0$ was investigated by Maurel *et al.* [76], but they do not provide a simple full-transmission condition analogous to Eq. (3.25) with $\phi = 0$.

3.3.1 Rigid grating elements

We assume that the grating element is much stiffer than the background medium, then in the limit $K/K_0 \to 0$ Eq. (3.25) becomes

$$\cos^2\theta_i = \frac{(1-f)\frac{\rho_{22}}{\rho} - 1}{\frac{\rho_1\rho_2}{\rho^2} - 1}. \tag{3.26}$$

If the rigid grating is much denser than the fluid, i.e. $\rho/\rho_0 \to 0$, then the dual limits yield a simple condition

$$\cos\theta_i = (1-f)\cos\phi. \tag{3.27}$$

This rigid limit case is of particular interest because it can be realized if the the background medium is air.

In this limiting case we have $c_\theta = c\cos\phi$, the transmission coefficient simplifies to

$$T(\theta) = e^{ika\sin\phi\sin\theta}/\big(\cos ka - \frac{i}{2}(\frac{\cos\theta}{\cos\theta_i} + \frac{\cos\theta_i}{\cos\theta})\sin ka\big). \tag{3.28}$$

Therefore,

$$|T(\theta)| = \cos\gamma, \quad |R(\theta)| = \sin\gamma, \quad \gamma = \tan^{-1}\big(\frac{1}{2}(\frac{\cos\theta}{\cos\theta_i} - \frac{\cos\theta_i}{\cos\theta})\sin ka\big) \tag{3.29}$$

and the relative phase of the transmitted waves for $\pm\theta$ is

$$\frac{T(-\theta)}{T(\theta)} = e^{-i2ka\sin\phi\sin\theta}. \tag{3.30}$$

3.3.2 Transmission at normal incidence: $\theta_i = 0$

Now, we consider the case of normal incidence. The total transmission condition $|T(0)| = 1$ requires

$$\frac{K}{K_0} = \frac{\rho_0^2 - (1-f)^2(\rho_0-\rho)^2\cos^2\phi}{\rho\rho_0 - f(1-f)(\rho_0-\rho)^2\cos^2\phi} \leq \frac{\rho_0}{\rho}. \tag{3.31}$$

This identity indicates a particularly interesting phenomenon that the required impedance ratio $\sqrt{K\rho/K_0\rho_0}$ depends on the density ratio and the geometric parameters f and ϕ, rather than on the relative bulk moduli. If any one of the three conditions $f = 1$, $\phi = \pi/2$ or $\rho_0 = \rho$ holds then Eq. (3.31) reduces to the expected one-dimensional impedance matching condition $K_0\rho_0 = K\rho$. However, when $f \neq 1$ and $\rho \neq \rho$, Eq. (3.31) indicates that the grating material must have higher impedance than the background fluid.

If we require that the total transmission at $\theta_i = 0$ corresponds to the element orientation angle $\phi = 0$, then Eq. (3.31) reduces to

$$\frac{K}{K_0} = \frac{\rho_0^2 - (1-f)^2(\rho_0 - \rho)^2}{\rho\rho_0 - f(1-f)(\rho_0 - \rho)^2}. \tag{3.32}$$

Next vary ϕ, with Eq. (3.32) satisfied, then Eq. (3.25) becomes

$$\sin\theta_i = \sqrt{\frac{(1-f)\rho_0}{f\rho + (1-f)\rho_0}\left(\frac{\rho_0 - \rho}{\rho_0 + \rho}\right)}\sin\phi. \tag{3.33}$$

This formula suggests an active model for changing the angular receptivity of the slab by rotating the elements of the single-layer grating.

3.3.3 Zigzag structures

A more general model, as shown in Fig. 3.3, is comprised of SLGs connected to each other in series with grating elements oriented at ϕ or $-\phi$. The only difference between adjacent

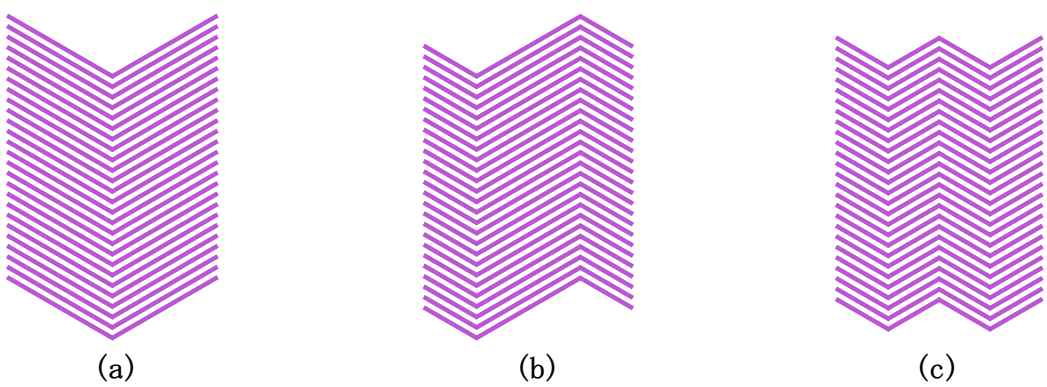

Figure 3.3: Zigzag structures comprised of SLGs in series with alternating orientations $\pm\phi$.

layers is that the effective density ρ_{12} changes sign. The thicknesses of the layers with orientation $\pm\phi$ are denoted by $b_\pm$, so that the total thickness is $b = b_+ + b_-$. Then the

transmission coefficient is written as

$$T = e^{-ik(b_+ + b_-)\frac{\rho_{12}}{\rho_{22}}\sin\theta}\Big(\cos\frac{\omega b}{c_\theta} - \frac{i}{2}\Big(\frac{Z_\theta}{Z'_\theta} + \frac{Z'_\theta}{Z_\theta}\Big)\sin\frac{\omega b}{c_\theta}\Big)^{-1}. \tag{3.34}$$

It is notable that all the examples in Fig. 3.3 have $b_+ = b_-$ and therefore $T(-\theta) = T(\theta)$ in each case.

3.4 Numerical examples and discussion

In this section, we show a few full wave simulation results to demonstrate the theory developed in this chapter. Different from the examples shown in Ref. [1], we will present the steady state FEM simulation of more complicated zigzag grating elements, as well as the transient simulation of underwater sound transmit through metallic gratings. The examples presented here use non-dimensional parameters, in particular the frequency is defined by kd. The grating elements has thickness a and length d, and therefore the total slab thickness is $b = a\cos\phi$, see Fig. 3.2. The steady state simulations were conducted with COMSOL Multiphysics using Floquet periodic boundary conditions to simulate wave transmission through an infinitely periodic structure. The transient simulations were done by computing at each time frame.

3.4.1 Transmission and reflection through rigid grating elements

We first consider three examples of rigid grating elments oriented at $\phi = 0°$, $30°$ and $60°$. The computed transmission and reflection coefficients for the three slanted gratings are showns in Fig. 3.4. The intromission angles were all chosen to be $\theta_i = 60°$, then the volume fraction f can be calculated using $(1-f)\cos\phi = 1/2$. It is easy to observe that the transmission spectrum does not change much as long as the relation between θ_i, ϕ and f is satisfied.

3.4.2 Full wave simulations of zigzag grating elements

In the previous example, the grating elements were assumed to be rigid. Now we consider more complicated zigzag gratings. As noted above, a plane wave incident at intromission angle θ_i can achieve total transmission through gratings comprised of alternating oriented

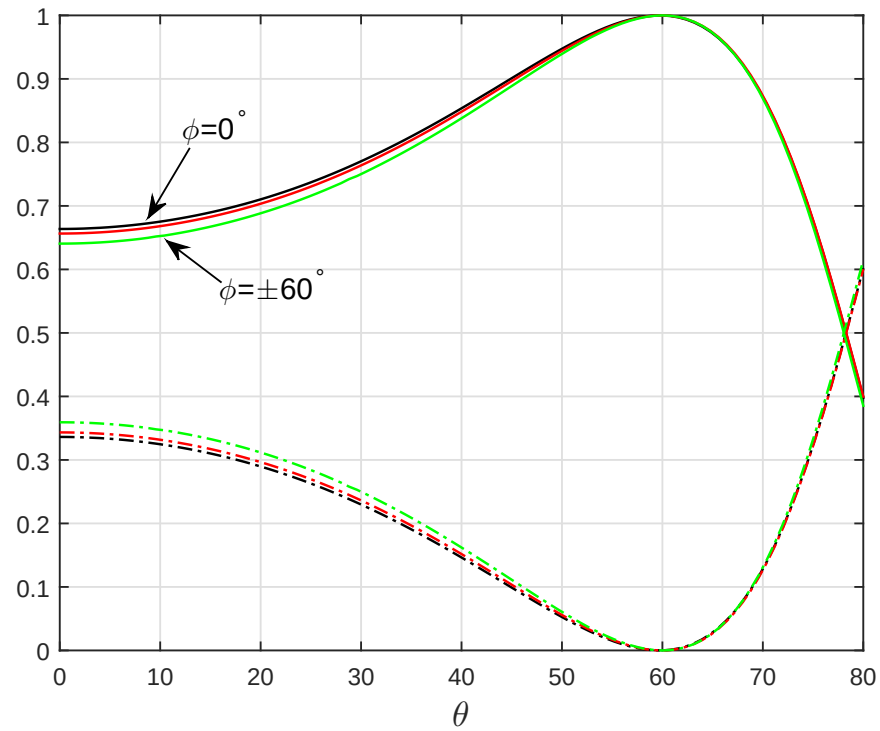

Figure 3.4: Transmission spectrum at frequency $kd = 0.25$ for rigid SLGs with elements oriented at $\phi = 0°$, $30°$ and $60°$. The solid and dashed curves represent $|T|^2$ and $|R|^2$, respectively.

elements. The background fluid is air with $\rho = 1.225$ kg/m^3 and $c = 346$ m/s, the grating elements are acrylic with $\rho_0 = 1190$ kg/m^3, $E_0 = 3.2$ GPa and $\nu_0 = 0.35$. The high contrast in material properties enables us to treat the grating elements as rigid, and therefore predict the intromission angle using Eq. (3.27). The zigzag plastic grating elements are oriented at alternating directions $\phi = \pm 30°$. The incident angle is taken to be the intromission angle $\theta_i = \cos^{-1}(1 - f)$, where $f = 0.5$. Full wave simulations were conducted in COMSOL Multiphysics to demonstrate our predictions. As shown in Fig. 3.5, a plane wave incident at $\phi = 60°$ from the left side achieves extraordinary transmission through the zigzag gratings. It is notable that the transmission is always close to unity as long as the wavelength is greater than periodicity of the grating elements.

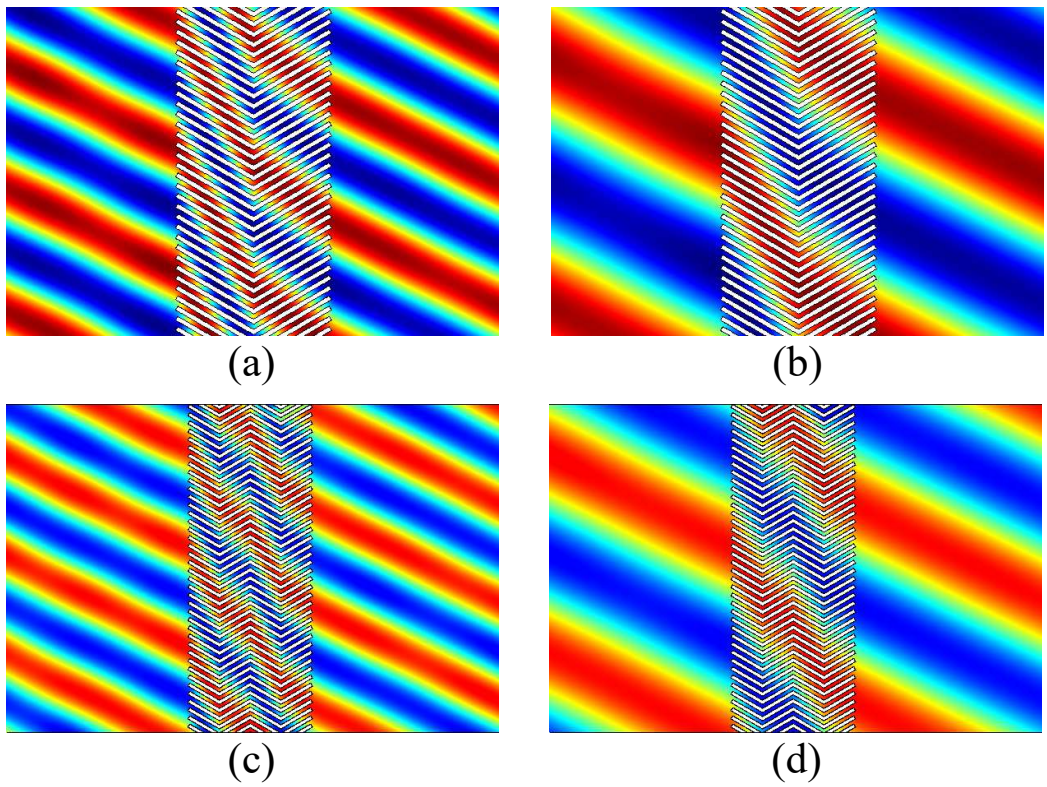

Figure 3.5: Total pressure plots for zigzag plastic gratings oriented at $\phi = \pm 30°$. The incident angle is taken to be the intromission angle $\theta_i = \cos^{-1}(1 - f)$, where $f = 0.5$. Frequency $kd = 0.5$ for (a) and (c), $kd = 0.25$ for (b) and (d).

3.4.3 Transient simulation of steel plates as grating elements in water

In previous example, the plastic grating elements in air were assumed to be rigid. Now we consider the scenario where background fluid is water with $\rho = 1000$ kg/m^3 and $c = 1500$ m/s. We will still using Eq. (3.27) to predict the intromission angle, thus we need a rather rigid and dense material for the grating elements. The properties of steel are $\rho_0 = 7800$ kg/m^3, $E_0 = 205$ GPa and $\nu_0 = 0.32$. The relatively high contrast in material properties might enable us to treat the grating elements as rigid, and therefore predict the intromission angle using Eq. (3.27). The grating elements are oriented at $\phi = 30°$. The incident angle is taken to be the intromission angle $\theta_i = \cos^{-1}(1 - f)$, where $f = 0.5$. The frequency is $kd = 0.25$. Transient simulations were conducted in COMSOL Multiphysics to demonstrated our predictions. As shown in Fig. 3.6, the amplitude of reflected wave is much smaller than the transmitted wave. We can conclude that a plane wave incident at $\phi = 60°$ from the left side achieves extraordinary transmission through the slanted grating comprised of steel plates.

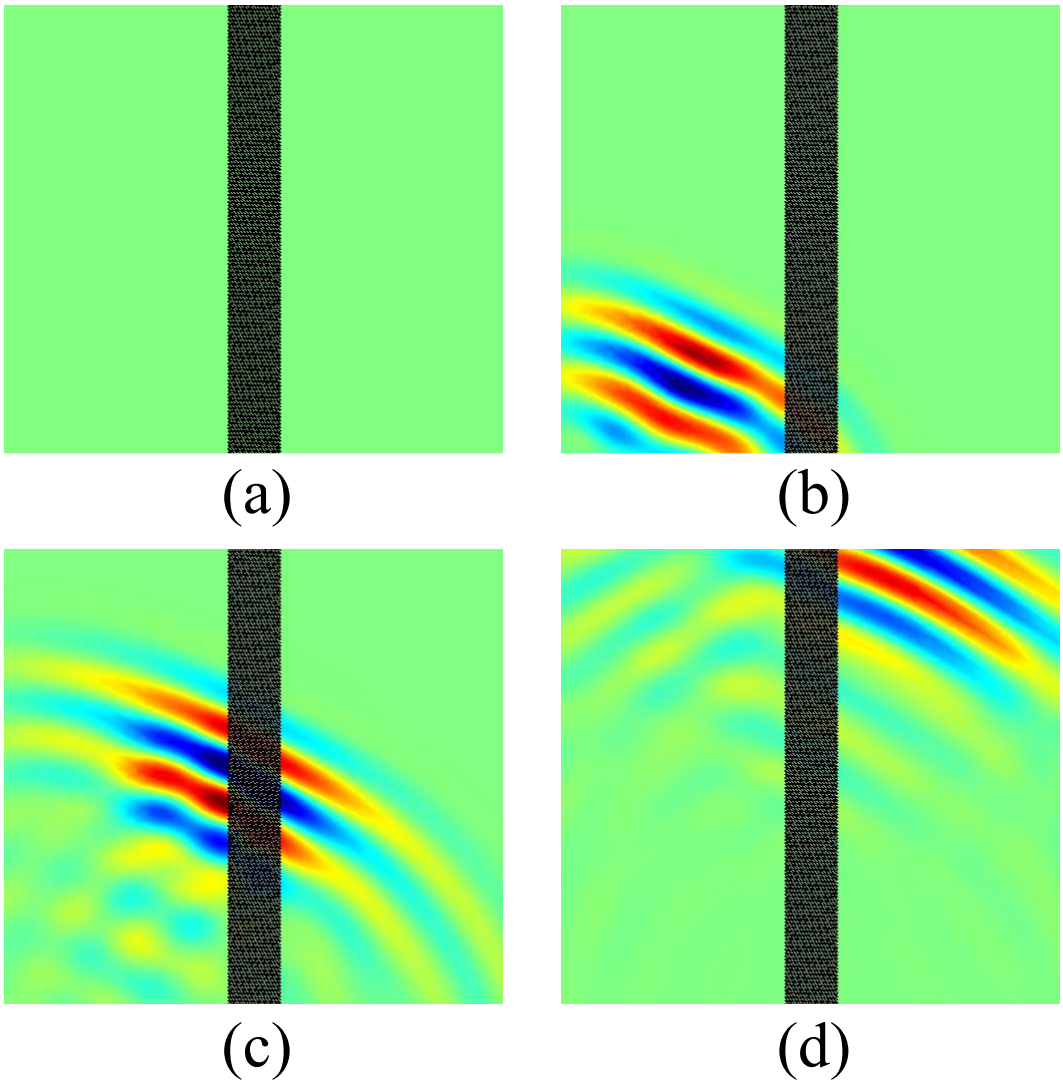

Figure 3.6: Total pressure plots for steel gratings oriented at $\phi = 30°$. The incident angle is taken to be the intromission angle $\theta_i = \cos^{-1}(1 - f)$, where $f = 0.5$. The frequency is $kd = 0.25$. Each plot corresponds to different time frame: (a) $t = 0$, (b) $t = 0.288$ ms, (c) $t = 0.552$ ms and (d) $t = 0.840$ ms.

3.5 Discussion

This chapter deals with acoustic transmission through slanted gratings. The gratings are treated as acoustic fluids of anisotropic inertia, so that the intromission angle is derived using a broadband impedance matching method. The main result here is Eq. (3.25) which predicts the intromission angle of the most general case. The results in this chapter may have significant applications in acoustic grating and Fresnel lens design. It might also help improve the performance of acoustic metamaterials, especially the transmissive devices. The present model might also be applied in the design of angle dependence acoustic devices, such as directional filters.

Chapter 4

Broadband pentamode gradient index lens for underwater sound

The quality of focused sound through a conventional Fresnel lens is usually limited by spherical/cylindrical aberration. Recent advances in acoustic metasurface design made it possible to manipulate the transmitted wavefront in an arbitrary way by achieving phase delay using space coiling structures [68, 66, 78, 79, 67]. The aberration of the focused sound can be reduced by carefully tuning the phase of the transmitted wave and doing a simple ray tracing. However, this diffraction based design approach usually suffers from unbalanced impedance [80] which is crucial to the prediction of focal position and destructive interference for canceling out side lobes, thus requires more sophisticated modeling in the design [81]. Many efforts have been made to achieve extraordinary transmission [70, 69], but the underlying physics is to tune the structure to achieve certain phase gradient of the transmitted wave at a particular frequency which limits the bandwidth of operation. Another disadvantage of the metasurface design is that the device only works at the steady state [80]. In other words, it can not focus a pulse to the focal spot. Apart from the aforementioned disadvantages, the space coiling structure is not applicable for underwater devices because of the low contrast between bulk modulus of common materials and water. Both the fluid phase and the solid phase are connected to the background fluid, the existence of the Biot fast and slow compressional waves [82, 83] might cause strong aberration and induce more side lobes, while the shear mode will cause undesired scattering. Thus, we need to employee an alternative method in our design to overcome these issues.

Hyperbolic secant index profile has been widely used GRIN lens designs [84]. Lin *et al.* [14] showed that the frequency independent analytical ray trajectories intersect at the same point, and demonstrated that it can be used in phononic crystal design to focus sound

inside the device without aberration. Climente *et al.* [48] adopted this approach in sonic crystal design, and experimentally demonstrated the broadband focusing effect beyond the lens with low aberration. Many other designs used the same index profile to focus airborne sound [85, 86, 87] and underwater sound [88]. Most of the designs are based on variation of the filling fraction to achieve different refractive indices which usually cause significant impedance mismatch. Although transmission is not a big concern in many applications, it is determinant in the focusing capability of the GRIN lens. The focal distance is derived from ray tracing which is a transient solution. Nevertheless, the focusing effect observed in the full wave simulations and experiments are both steady state response which can be altered due to impedance mismatch. One exception is that Martin *et al.* [89] modified the index distribution to reduce aberration and achieved high transmission by using hollow aluminum shells in water matrix. However, the idea of adjusting filling fraction introduces anisotropy and limits the range of effective properties which restrict the focal spot to be far from the lens.

In this chapter, we utilize the two dimensional (2D) version of the pentamode material (PM) [30, 90] to achieve a wide range of refractive index, and introduce a new modification of index profile for further aberration reduction. The advantage of PMs is that they can be designed to match acoustic impedance to water and minimize shear modulus which is undesired in acoustic designs. They are thus are very promising in underwater applications. For instance, Hladky-Hennion *et al.* [16] tuned the effective acoustic properties to water and experimentally demonstrated negative refraction at the longitudinal compressional mode. The structure is versatile such that it can be designed to achieve strong anisotropy [91], therefore is also a good choice for acoustic cloaking [29, 92]. In our design, the unit cells are transversely isotropic with index varying along the incidence plane. The modification of the index profile is done by using a one dimensional coordinate transformation, the aberration reduction can be clearly observed from ray trajectories. The unit cells of the GRIN lens are designed using a static homogenization technique based on FEM [93] according to the modified index profile with a range from 0.5 to 1. Moreover, all the unit cells are impedance matched to water which is the key to obtain optimal focusing effect. The GRIN lens is fabricated by cutting centimeter scale hollow microstructures on aluminum plates

using waterjet, then stacking and sealing them together. The interior of the compact solid matrix lens is filled with air, only the exterior faces are connected to water. The GRIN lens is experimentally demonstrated to be capable of focusing underwater sound with high efficiency from 25 kHz to 40 kHz. The present design has potential applications in ultrasound imaging and underwater sensing where the water environment is important. The successful demonstration of our GRIN lens also shed light on the realization of pentamode acoustic cloak [29, 92].

This chapter is outlined as follows. In Sec. 4.1, we review and compare a few index gradient profiles, and propose a modified profile to reduce aberration. Then we design the lens using 2D pentamode unit cells following the reduced aberration profile in Sec. 4.2. The frequency and transient domain simulations results are presented in Sec. 4.3. Section 4.4 concludes this chapter.

4.1 Index gradient

4.1.1 Focal distance

The 2D GRIN lens presented in this chapter is designed as depicted in Fig. 4.1 with index profile symmetric with respect to the x-axis ($y = 0$). Assuming that the refractive index n is a function only of y, the trajectories of a normally incident plane wave can be derived by solving a ray equation for $y = y(x)$ based on the fact that the component of slowness along the interface between each layer is constant:

$$\frac{n\big(y(x)\big)}{\sqrt{1 + y'^2(x)}} = n(y_0) \tag{4.1}$$

where $y_0 = y(0)$ is the incident position on the y-axis at the left side of the lens, $x = 0$. The focal distance from the right hand boundary of the GRIN lens at $x = t$ is [48, Eq. (3)]

$$d = \frac{y(t)}{y'(t)}\sqrt{n^{-2}(y_t) + \big(n^{-2}(y_0) - 1\big)y'^2(t)} \tag{4.2}$$

where y_t is the value of $y(t)$ on the ray at the emergence point. The value of $y'^2(t)$ follows from Eq. (4.1), from which we deduce the simpler expression

$$d = y_t\sqrt{\frac{1}{n^2(y_t) - n^2(y_0)} - 1}. \tag{4.3}$$

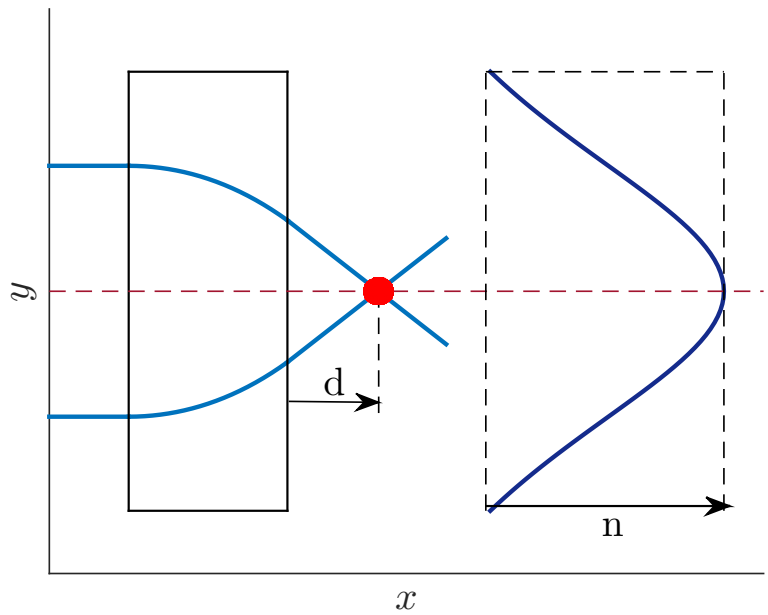

Figure 4.1: Schematic view of the GRIN lens. The left part shows that two ray paths incident at symmetric positions intersect at the focal point beyond the lens. The right part shows the index distribution across the lens.

4.1.2 Hyperbolic secant profile

We first consider a hyperbolic secant index profile $n(y)$, which is often used to design for low aberration [14]:

$$n(y) = n_0 \operatorname{sech}(\alpha y), \tag{4.4}$$

where α is a constant, n_0 is the refractive index at $y = 0$. The ray trajectory can then be expressed as

$$y(x) = \frac{1}{\alpha} \sinh^{-1}[\sinh(\alpha y_0) \cos(\alpha x)], \tag{4.5}$$

and the focal distance for this particular index function becomes

$$d = \frac{y_t}{n_0} \sqrt{\frac{1}{\tanh^2(\alpha y_0) - \tanh^2(\alpha y_t)} - n_0^2}. \tag{4.6}$$

However, the index profile will introduce aberration if our aim is to focus sound outside the lens. Therefore, we need to consider other possible index profiles and seek modifications to reduce aberration.

4.1.3 Quadratic profile

Alternatively, consider the quadratic index profile [89]

$$n(y) = n_0\sqrt{1-(\alpha y)^2}, \tag{4.7}$$

for which the rays are

$$y(x) = y_0\sqrt{2}\sin\left(\frac{\pi}{4} - \frac{n_0\,\alpha x}{n(y_0)}\right). \tag{4.8}$$

The rays incident from different y_0 do not intersect at the same point, therefore this index profile also introduce aberration.

4.1.4 Reduced aberration profile

Martin *et al.* [89] noted that the above mentioned two profiles have opposite aberration tendencies, and proposed a combination of the two profiles which shows reduced aberration. Nevertheless, in our model we are interested in a wide range in index, from unity to about 0.5 due to the restrictions of the unit cell design employed in this chapter. This requires αy_0 to exceed unity, which rules out the use of the quadratic profile. Alternatively, we propose stretching the $y-$coordinate of the hyperbolic secant profile as follows:

$$\begin{aligned} n(y) &= n_0\,\mathrm{sech}\big(g(\alpha y)\big) \quad \text{where} \\ g(z) &= z/\big(1+\beta_1 z^2 + \beta_2 z^4\big). \end{aligned} \tag{4.9}$$

The objective is to make d of Eq. (4.3) independent of y_0 as far as possible.

For small αy_0 we have from both Eqs. (4.5) and (4.8) that $y(x) \approx y_0\cos\alpha x$, and hence for all three profiles

$$d \to d_0 \equiv \frac{1}{n_0\alpha}\cot\alpha t \quad \text{as } \alpha y_0 \to 0. \tag{4.10}$$

Note that d_0 is independent of y_0 as expected. This is the value of the focal distance that the modified profile Eq. (4.9) attempts to achieve for all values of y_0 in the device by choosing proper values of the non-dimensional parameters β_1 and β_2. As a demonstration, we plot the ray trajectories using the hyperbolic secant profile and our modified secant profile with index ranging from 0.5 to 1. As shown in Fig. 4.2, the focal points form a line when the hyperbolic secant profile is used, while the rays intersect at the same point when

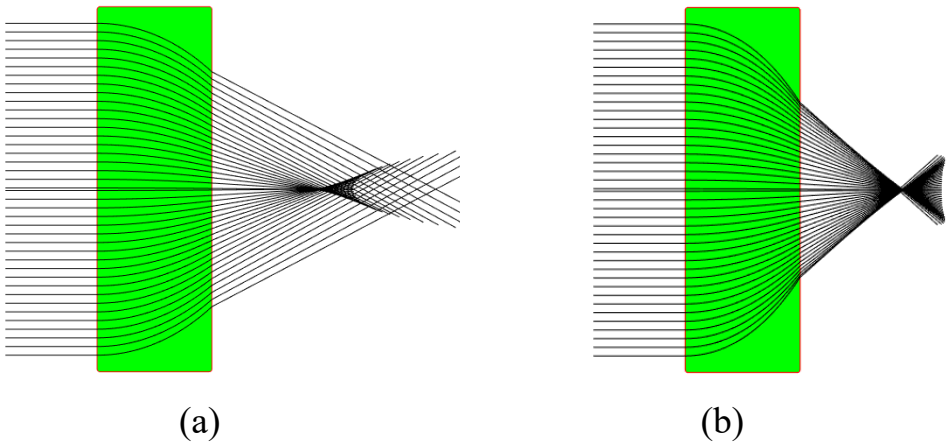

Figure 4.2: Comparison between the ray trajectories. (a) Strong aberration using the hyperbolic secant profile, (b) Minimized aberration using the modified secant profile.

the modified profile is used. This suggests that we can design the GRIN lens according to the modified profile.

4.2 Design of unit cells

The flat GRIN lens is designed using six types of unit cells corresponding to the discrete values selected from the modified hyperbolic index profile. Figures 4.3(a) and 4.3(b) show the spatial distribution of refractive indices of the lens. The unit cell structure is the regular hexagonal lattice which has in-plane isotropy at the *quasi-static regime* [94]. Using Voigt notation, the 2D pentamode elasticity requires $C_{11}C_{22} \approx C_{12}^2$ and $C_{66} \approx 0$ minimize the shear modulus. With these requirements satisfied, then the main goal is to tune the effective C_{11} and mass density at the homogenization limit to achieve the required refractive index and match the impedance to water simultaneously. The material properties of water are taken as bulk modulus $\kappa_0 = 2.25$ GPa and density $\rho_0 = 1000$ kg/m^3. The material of the lens slab is aluminum with Young's modulus $E = 70$ GPa, density $\rho = 2700$ kg/m^3 and Poisson's ratio $\nu = 0.33$. The geometric parameters of each unit cell, as shown in Fig. 4.3(d), are predicted using foam mechanics [95] and iterated using a homogenization technique based on FEM [93]. The geometric parameters of the six types of unit cells are listed in Table 4.1. Note that big value of the radius r at the joints increases the effective shear modulus, but $r = 0.420$ mm is the limit of the machining method we are using.

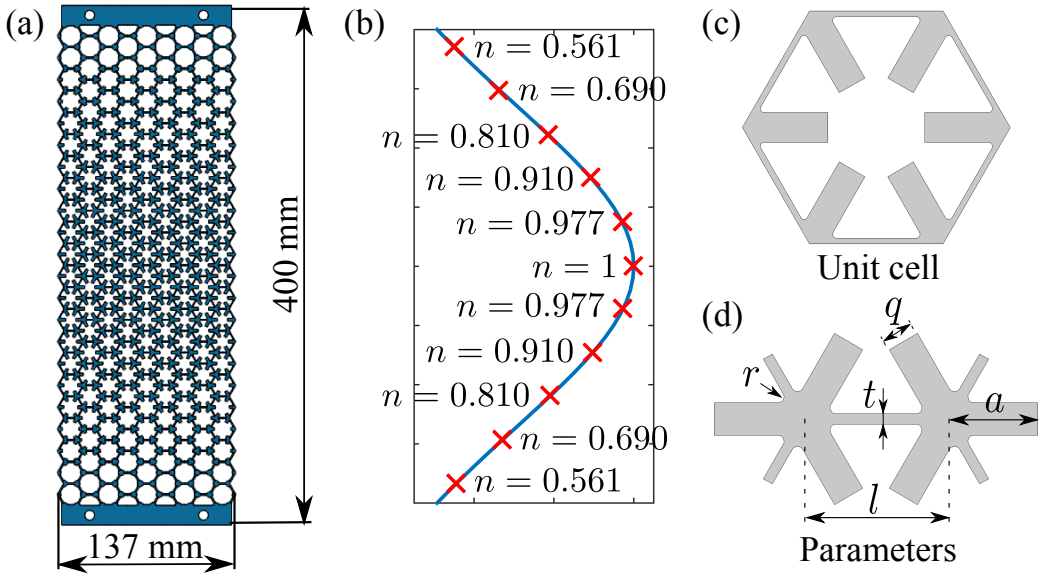

Figure 4.3: Layered design. (a) The top view of the lens, (b) the index distribution and discretized indices of the lens, (c) unit cell of the lens and (d) geometric parameters of the unit cell.

Table 4.1: Geometry of the unit cells. Each type of unit cell corresponds to different values of effective refractive indices as shown in Fig. 4.3(b).

n_{eff}	l (mm)	t (mm)	a (mm)	q (mm)	r (mm)
1.000	9.708	0.693	6.025	2.184	0.420
0.977	9.708	0.708	5.844	2.184	0.420
0.910	9.708	0.761	5.295	2.184	0.420
0.810	9.708	0.851	4.451	2.184	0.420
0.690	9.708	0.994	3.397	2.184	0.420
0.561	9.708	1.213	2.177	2.184	0.420

The GRIN lens is comprised of the six types of unit cells, the minimum cut off frequency is limited by the thinnest unit cell, i.e. $n_{\text{eff}} = 1$, therefore it is essential to examine its band structure. The band diagram as shown in Fig. 4.4 is calculated using Bloch-Floquet analysis in COMSOL Multiphysics. The directional band gap along the incident direction occurs near 40 kHz, this sets the upper limit of the lens. The lens is designed following a index gradient which limits the low frequency focusing capability due to the high frequency approximation nature of the ray theory. It is notable that although the bending modes exist at low frequency range, they do not cause much scattering due to sufficient shear modulus which prevents the structure from flexure [96]. We expect the lens to be capable of focusing underwater sound over a broadband from 10 to 40 kHz.

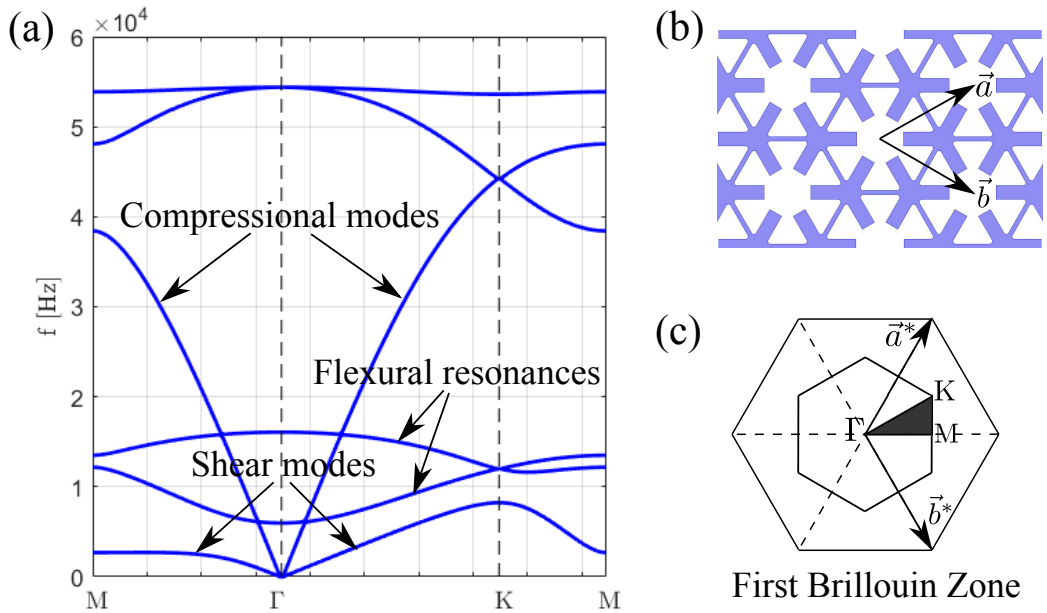

Figure 4.4: Band diagram of the unit cell at the center ($n_{\text{eff}} = 1$). (a) shows the band structure along the $\Gamma - M - K$ path of the first Brillouin zone, (b) shows the lattice structure where $\vec{a}$ and $\vec{b}$ are the basis vectors in the real space, (c) shows the first Brillouin zone of the lattice structure where $\vec{a}^*$ and $\vec{b}^*$ are the basis vectors in the reciprocal space.

4.3 Simulation results

The lens is formed by combining all the designed unit cells together following the reduced aberration profile. The width of the lens is 40 cm, and the thickness is 13.7 cm. The material of the lens is aluminum as we described in previous section. The GRIN is permeated with air and immersed in water, so that only structural wave is allowed in the lens. Full wave simulations were done to demonstrate the broadband focusing effect using COMSOL Multiphysics. Figure 4.5 shows the normalized intensity magnitude plots from 10 to 35 kHz, where blue color represents small value and red color represents big value. The plane Gaussian beam is incident from the left side, the focal point lies on the right side of the lens. It is clear that the lens works over a broad range of frequency. There are some discrepancies of the focal distance at low and high frequency range. The low frequency focusing capability is limited due the high frequency approximation nature of the index gradient, while the high frequency is limited because the longitudinal wave becomes more dispersive. The best operation frequency of the lens is near 20 kHz, and its cutoff frequency

is near 40 kHz as predicted from band diagram.

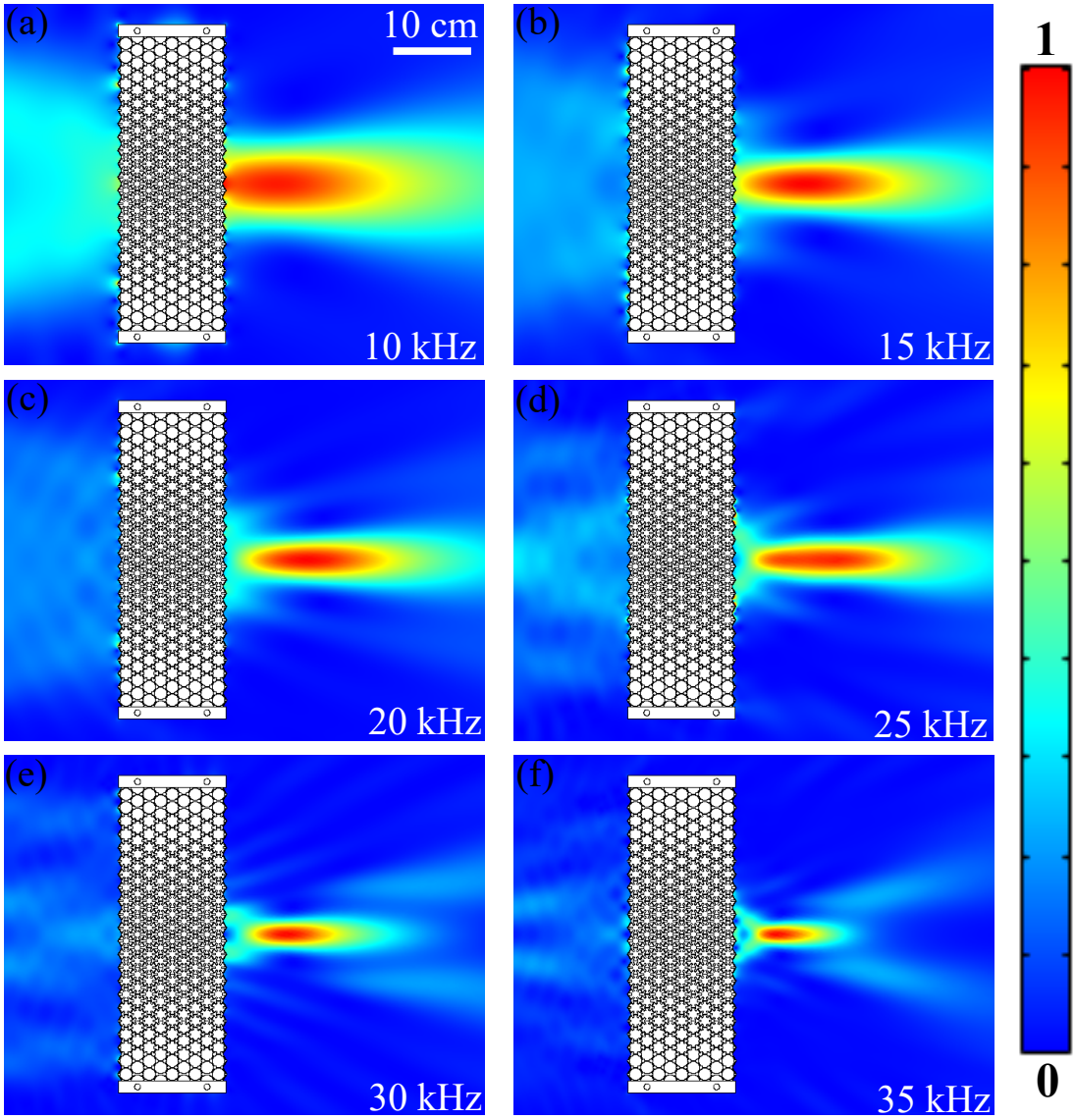

Figure 4.5: Full wave frequency domain simulation results at (a) 10 kHz, (b) 15 kHz, (c) 20 kHz, (d) 25 kHz, (e) 30 kHz and (f) 35 kHz.

This GRIN lens is aberration free because it is designed to be impedance matched to water, so that it is back-scattering free and therefore works as predicted. It is necessary to demonstrate the high energy transmission of the lens. Figure 4.6 shows the sound pressure level gain (SPL) over the focal plane at 35 kHz. The results are calculated by subtracting the simulated SPL with the lens from the simulated SPL without the lens. The maximum gain at 35 kHz is about 10 dB, which indicates that most of the energy are focused at the focal point, i.e. the transmission is high. We can safely conclude that this lens has minimal

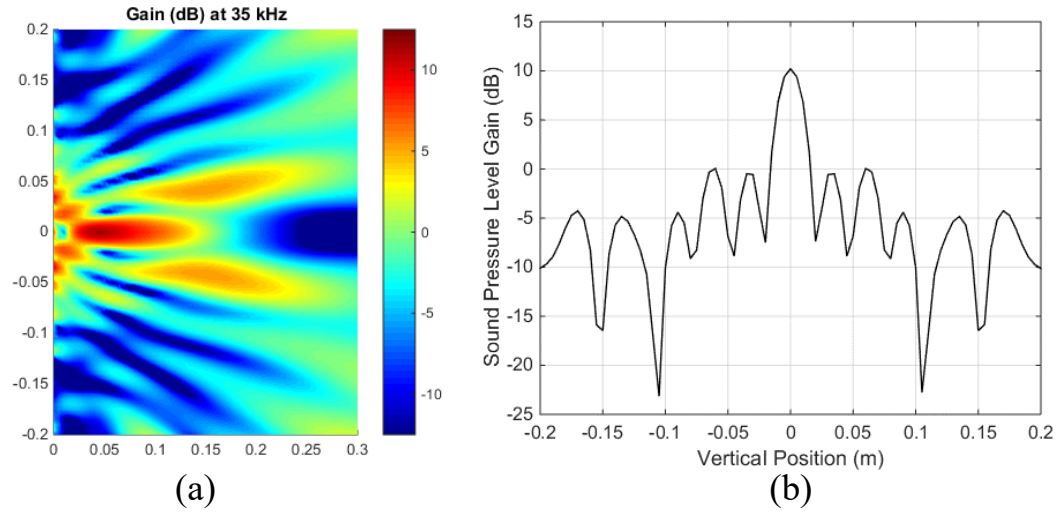

Figure 4.6: Sound pressure level gain (SPL) at 35 kHz. (a) Colormap over the focal plane, (b) SPL across the focal point along the lens face.

aberration.

The GRIN lens has minimal side lobes comparing to conventional diffractive lens. Diffractive acoustic lenses are usually designed by tuning the impedance of each channel to achieve certain phase delay. However, the transmitted amplitudes are different so that it is hard to cancel out the side lobes caused by aperture diffraction. The main advantage of the GRIN lens is that it redirects the ray paths inside the lens, and reduces the diffraction aperture to a minimal size at the exiting face of the lens. As shown in Fig. 4.7, the width of the intensity profile at half of its maximum is only 0.6λ at 30 kHz and 0.47λ at 35 kHz. It is

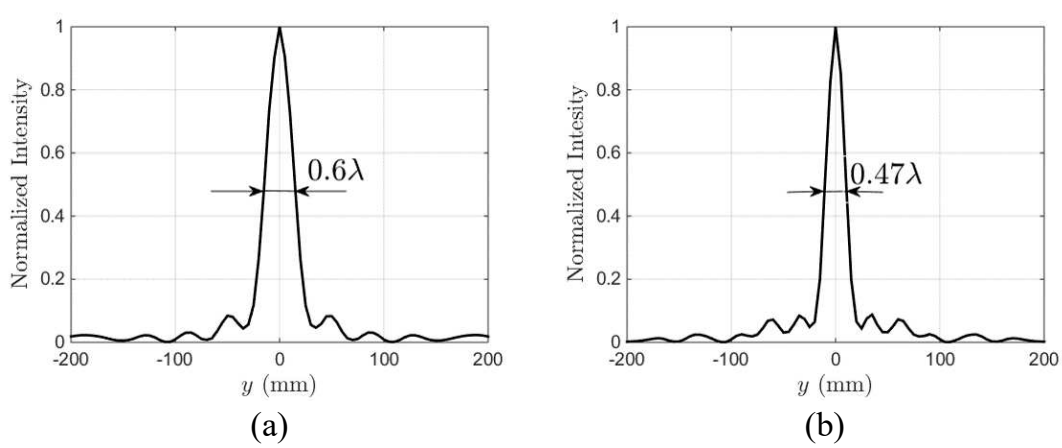

Figure 4.7: Normalized intensity magnitude across the focal point along the lens face at (a) 30 kHz and (b) 35 kHz.

clear that the intensity magnitudes of the side lobes are all below 1/10 of the maximum value so that our GRIN lens is side lobe free.

The bulk GRIN lens not only works at the steady state, but also is capable of focusing a pulse. Figure 4.8 shows the simulated pressure variations at each time frame. Two cycles

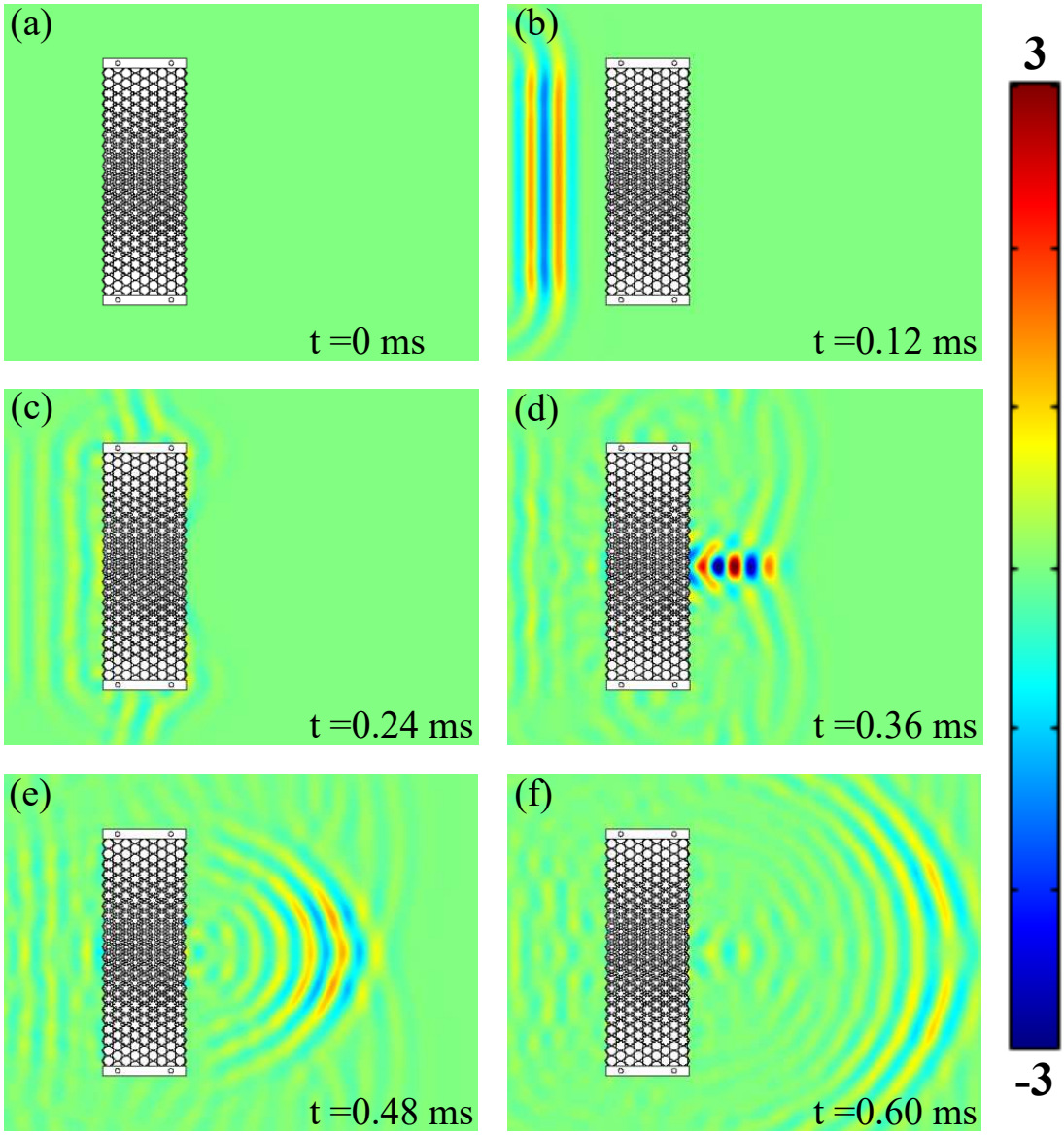

Figure 4.8: Full wave time domain simulation of normally incident plane wave at 30 kHz. The plots show the pressure variations at each time frame: (a) 0 ms, (b) 0.12 ms, (c) 0.24 ms, (d) 0.36 ms, (e) 0.48 ms and (f) 0.60 ms.

of a plane wave pulse is incident from the left side at the central frequency of 30 kHz. The waves focus at the right side of the lens and start to spread out when $t = 0.36$ ms. It is also clear that the reflection from the water-lens interface is negligible. Based on reciprocity,

the GRIN has anther feature that it is capable of collimating cylindrical sources, if located at the focal point, to plane wave beams. Here we demonstrate the collimation effect using transient domain FEM simulation as shown in Fig. 4.9. The distance from the source to the

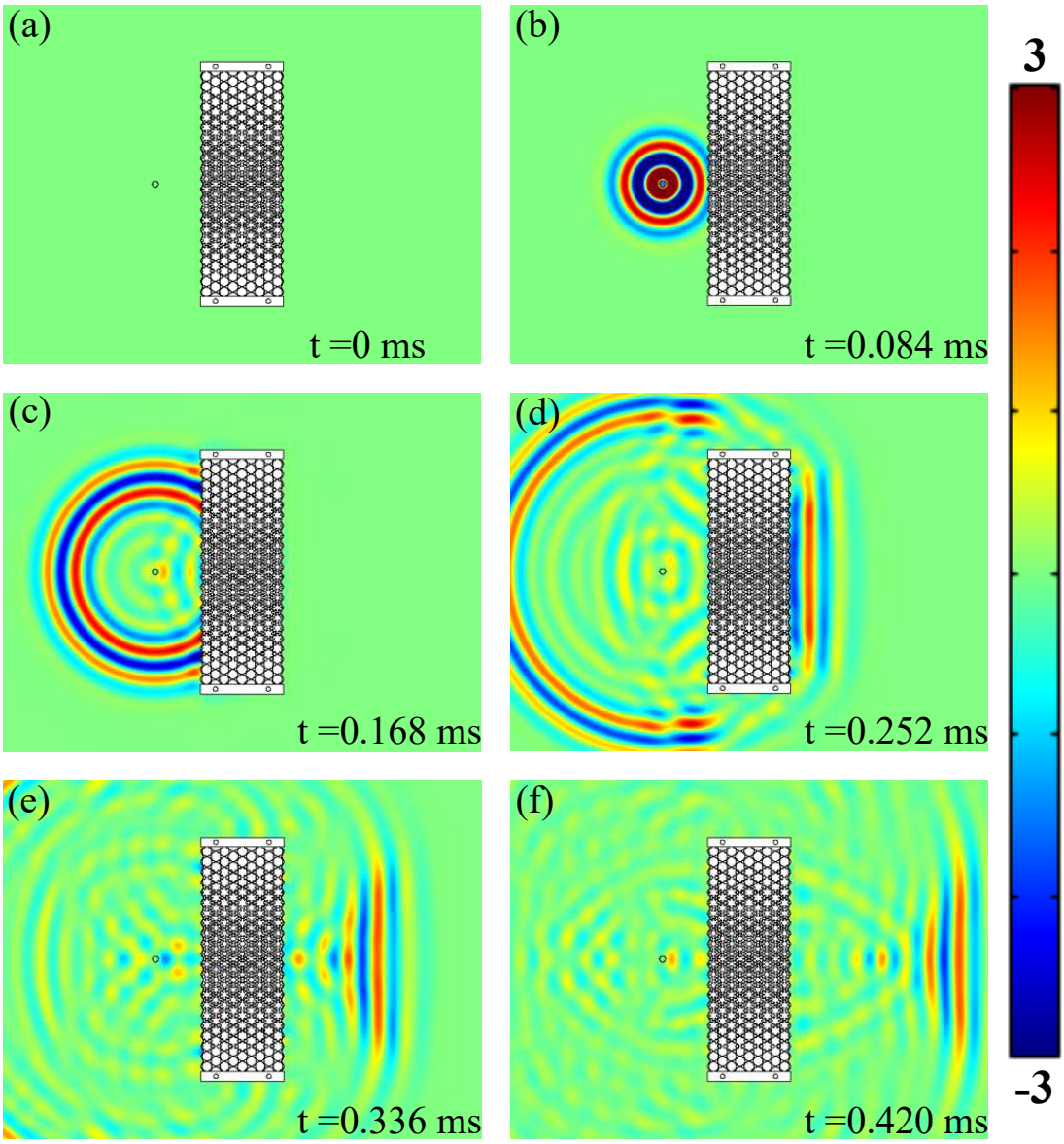

Figure 4.9: Full wave time domain simulation of a cylindrical source at 30 kHz. The plots show the pressure variations at each time frame: (a) 0 ms, (b) 0.084 ms, (c) 0.168 ms, (d) 0.252 ms, (e) 0.336 ms and (f) 0.420 ms.

lens equals to the focal distance. Two cycles of a cylindrical wave radiate from the source and then be transformed into a plane wave beam when they exit from the right side of the lens.

4.4 Discussion

To summarize, we have designed and fabricated a pentamode GRIN lens according to the modified secant index profile. The modified hyperbolic secant profile aims to reduce aberration and suppress side lobes. The gradient index (GRIN) lens is comprised of transversely isotropic hexagonal microstructures with tunable *quasi-static* bulk modulus and mass density. In addition, the unit cells are impedance-matched to water and have in-plane shear modulus negligible compared to the effective bulk modulus. Moreover, the physics behind the GRIN lens makes it possible to focus sound at both steady state and transient domain. The flat GRIN lens is fabricated by cutting rectangular centimeter scale hollow microstructures in aluminum plates, which are then stacked and sealed from the exterior water. Broadband focusing effects are observed within the homogenization regime of the lattice in finite element (FEM) simulations ($10 - 40$ kHz). Underwater measurements have been done by our collaborators at the University of Texas at Austin, though the results are not compared in this dissertation. There are some discrepancies between the simulation and the experimental results. The mismatch of the focal distance in simulation and experiments is due to the machining accuracy of the waterjet and the assembling method which altered the refractive index. This issue can be resolved by using more sophisticated fabrication method such as wire EDM or 3D metal printing. The design method can also be easily extended to the design of anisotropic metamaterials such as directional screens and acoustic cloaks.

Chapter 5

Directional cylindrical-to-plane wave lens for underwater acoustics

The first transformation based metamaterial device was proposed a decade ago when Pendry *et al.* [22] derived a cloak based on the invariance of Maxwell's equations under coordinate change. While subsequent applications of transformation optics (TO) and transformation acoustics (TA) have proven to be very successful in the design of cloaking devices (for reviews see e.g. [97] and [98]) the concepts underlying TO and TA are by no means limited to cloaking of waves, which involves a singular transformation, i.e. the mapping of a point into a finite volume. While the singular transformation is a limiting case, there are many regular spatial transformations of interest which also leave the wave equation invariant and provide the ability to manipulate electromagnetic and acoustic wave motion in many other unprecedented ways. Such transformation based applications for electromagnetic (EM) waves include directional antennas [23], field rotators [24], concentrators [25], beam shifters and splitters [26], just to name a few.

Along similar lines, transformation acoustics has been proposed in the design of acoustic metamaterials, starting naturally with cloaking. Cummer *et al.* [27] theoretically analyzed 2D acoustic cloaking with anisotropic mass density. This concept was applied to 3D by Chen *et al.* [28]. Later on, Norris [29] published a theory on acoustic cloaking with anisotropic bulk modulus and suggested to design using pentamode material (PM), which is first proposed by Milton *et al.* [30]. TA has then been extended to numerous applications, such as carpet cloaking [31] which is later experimentally realized by Popa *et al.* [32]. The cylindrical-to-plane wave lens based on conformal transformation also attracted much attention [99, 33]. Titovich *et al.* [100] proposed a feasible design using elastic shell metamaterial elements

and demonstrated the collomation effect experimentally [34]. However, these cylindrical-to-plane wave lenses all divide energy equally into four lobes. In this chapter, we map the circular domain to a triangle to reduce the number of lobes from four to three, and introduce an adjustable parameter in the mapping to make the lens more directional.

The strong interaction between the waves in the structures and the surrounding medium brings more complexity to the design of metamaterial devices for underwater purposes. Nevertheless, the low contrast between the acoustic properties of water and natural materials makes it possible to manipulate the effective properties of the metamaterial. For example, PMs can be tuned to mimic the behavior of water [90] and used for acoustic cloaking [92]. PMs have also been successfully applied in the design of an elasto-mechanical unfeelability cloak [101] and acoustic negative refraction lens [16]. However, the required material properties for our GRIN lenses go beyond the range we can achieve using single natural material, which rules out the use of PMs. Using elastic shells as the design units is another possible approach [100, 102, 34, 103, 104, 105], because they can be tuned to achieve effective acoustic properties similar to water. For instance, Martin *et al.* [89] designed and tested a GRIN lens made of hollow aluminum shells to overcome the impedance mismatch issue in their previous work [88].

The TA mapping from a circular region to a triangular shape used in our design is conformal, which guarantees that the material properties in the transformed domain are isotropic [106]. The approach of immersing empty elastic shells in a water matrix is adopted in our design. The cylindrical shells are chosen for their *quasi-static* effective properties (density and bulk modulus), which depend upon the shell material and the thickness to radius ratio. By selecting a range of metals and polymers for the shell materials and variety of tube thicknesses, a considerable range in properties is possible. We designed two GRIN lenses by carefully choosing appropriate shells. Full wave simulations show that the first lens radiates the energy of a source located at the lens center equally in three directions, whereas in the second lens half of the source energy is radiated through one of the three faces.

The outline of this chapter is as follows. The mapping and material properties in the transformed triangular domain are discussed in Sec. 5.1. A few examples of the bulk modulus

distribution are shown in Sec. 5.2. The collimation effect is also analyzed in Sec. 5.2 by showing the ray trajectories and demonstrated by using effective medium simulations. The design procedures of the GRIN lenses are described in Sec. 5.3 as well as the simulation results. Conclusions are presented in Sec. 5.4.

5.1 Transformation acoustics mapping

The GRIN lens design is based on the transformation of a unit circle in the complex z-plane to an equilateral triangle with vertices A and B at $(1/2 \pm i\sqrt{3}/2)a$ in the t-plane as shown in Fig. 5.1. The precise form of the mapping function Eq. (B.4) is derived in the Appendix B.

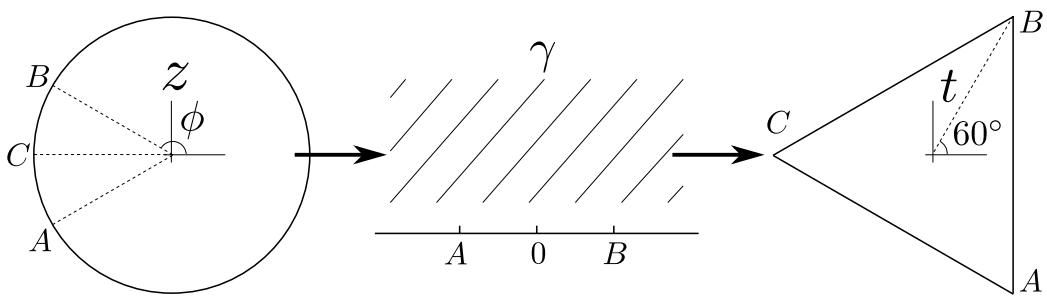

Figure 5.1: Conformal mapping from a circular domain to a triangular domain.

We consider a background acoustic medium of density ρ and bulk modulus K in which the governing equation is

$$\nabla^2 p + \frac{\omega^2}{c^2} p = 0, \tag{5.1}$$

where $c = \sqrt{K/\rho}$ is the sound speed, ω is the radial frequency with time harmonic dependence $e^{-i\omega t}$ assumed. Then the TA mapping maps the acoustic equation into the transformed domain and yields a new distribution of material properties. The density in the transformed domain is denoted by ρ', the bulk modulus is denoted by K'. The TA mapping that gives parameter distribution in the transformed domain has been studied thoroughly by [106], here we directly use the results of the special case of conformal mapping. The transformed density and bulk modulus are

$$\rho' = \rho, \quad K' = |dt/dz|^2 K, \tag{5.2}$$

which are functions of the derivative of the mapping function. The transformed wave speed and impedance are therefore $c' = |dt/dz|c$ and $Z' = |dt/dz|Z$ where $c = \sqrt{K/\rho}$ and $Z = \sqrt{K\rho}$ are the original values. The derivative of the mapping function, i.e. Eq. (B.4), is

$$\frac{dt}{dz} = \frac{\sqrt{3}a}{2G(1)} \sin\phi \Big((z+1)(z-e^{i\phi})(z-e^{-i\phi}) \sin\frac{\phi}{2} \Big)^{-2/3} \tag{5.3}$$

where $G(1)$ is defined in the Appendix B.

5.2 Directional collimation

5.2.1 Impedance matching condition and far-field behavior

A particularly significant value for the transformed bulk modulus is the value at $z = 1$, $K_{\min} = K'(z = 1)$, which is the lowest value of K' in the triangle, and sets a lower limit on the required bulk modulus,

$$K_{\min} = 3\Big(\frac{a \cot\frac{\phi}{2}}{4G(1)} \Big)^2 K. \tag{5.4}$$

For instance, $K_{\min}$ is $0.1271\, a^2 K$, $0.0424\, a^2 K$ and $0.0141\, a^2 K$ for $\phi = \pi/3$, $\pi/2$ and $2\pi/3$, respectively. The mapping leads to unbounded bulk modulus at three vertices of the triangle, however, in practice these are cutoff at finite values.

Conformal tansformation based acoustic antennas usually suffer from impedance mismatch at the boundary which causes internal resonance and reduces the transmission. It is obvious that the mapped bulk modulus range depends on the value of a, i.e. the distance from the origin to the vertices of the triangle. This provides a simple way to achieve better performance by matching the impedance at the center of AB face. Letting $K'(z = 1) = K$, we have

$$a = \frac{4}{3}\sqrt{3}G(1) \tan\frac{\phi}{2}. \tag{5.5}$$

The ray densities near the center of AB face tend to be uniform if Eq. (5.5) is satisfied, eg. $a = 2.8044$ for $\phi = \pi/3$. This impedance matching condition also provides a nice feature that the pressure distribution along AB face is similar to a Gaussian beam. Figure 5.2 shows the comparison between two lenses with the same $\phi = \pi/3$ but different values of a. The lenses have the same dimensions, and the simulations are done at the same frequency.

For acoustic sources of maximum dimension $D \gg \lambda$, the Fraunhofer near-field distance can be approximately taken as [107, p. 165]

$$d_f = \frac{D^2}{4\lambda}. \tag{5.6}$$

It is known that sound waves start to spread out beyond this distance. However, we can achieve better far-field behavior by matching impedance at the center of AB face. Figure 5.2 clearly shows that the spreading region is extended to $d = 2.5d_f$ for the lens designed with Eq. (5.5) satisfied due to the Gaussian-like pressure distribution.

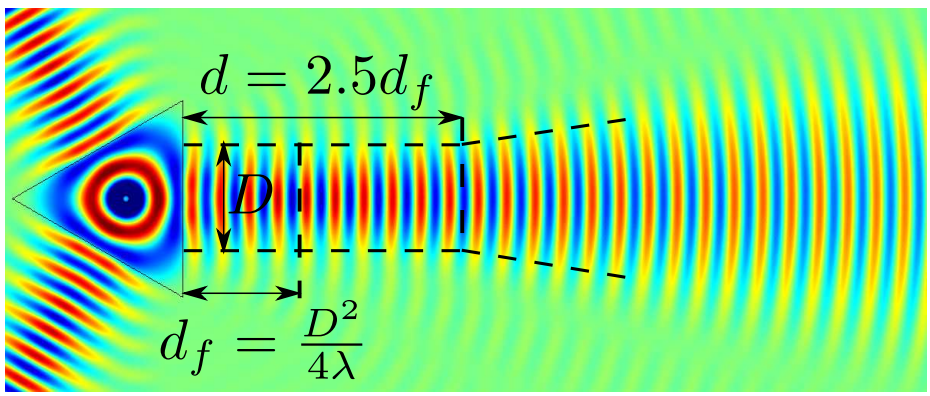

(a)

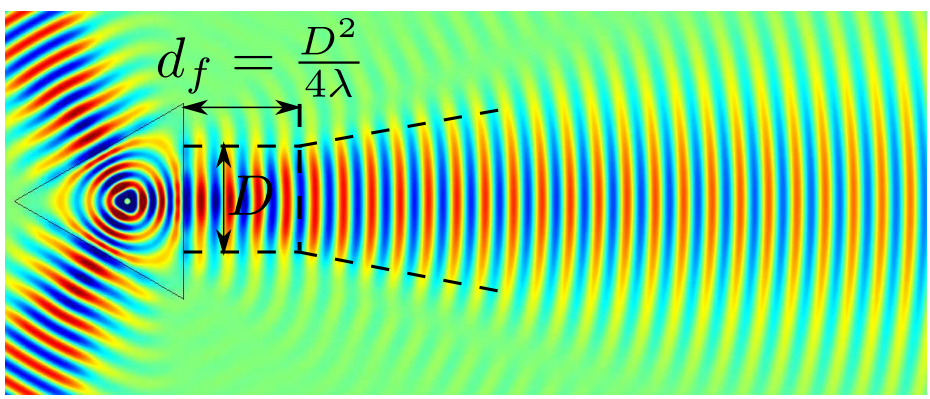

(b)

Figure 5.2: Comparison of far-field radiation behavior for $\phi = \pi/3$ and different values of a where (a) $a = 2.8044$ with impedance matched at the middle of AB face, and (b) $a = 1.2092$ for unchanged perimeter.

It is also notable that the impedance at the source location is within a reasonable range. We are interested in placing the monopole source in water matrix, this implies a impedance

matching condition at the source location. Letting $K'(z=0)=K$, we have

$$a = \frac{\sqrt{3}G(1)}{3\cos\frac{\phi}{2}\sin^{1/3}\frac{\phi}{2}}. \tag{5.7}$$

If both Eqs. (5.5) and (5.7) are satisfied, then we can achieve optimized values for ϕ and a. However, we are interested in designing for different values of ϕ, there is a bit of compromise between the boundary impedance and source location impedance. The material property range we can achieve is limited which, in turn, affects the selection of the value of a.

5.2.2 Directional collimation using effective medium

We consider water ($\rho = 1000$ kg/m^3, $K = 2.25$ GPa) as the background fluid. It is obvious from Eqs. (5.2) and (5.3) that the value of a changes the range of bulk modulus in the transformed domain. By choosing $a = \sqrt{4\pi/3\sqrt{3}} = 1.5551$ for unchanged area and setting $K'_{\max} = 3.65K$, we can restrict the bulk modulus in an achievable range. When the transformed density is unchanged, both the relative wave speed c'/c and the relative impedance Z'/Z are equal to $\sqrt{K'/K}$. Figure 5.3 shows the color map of the bulk modulus distribution for $\phi = \pi/3$, $\pi/2$ and $2\pi/3$, respectively. The dimensions of the transformed

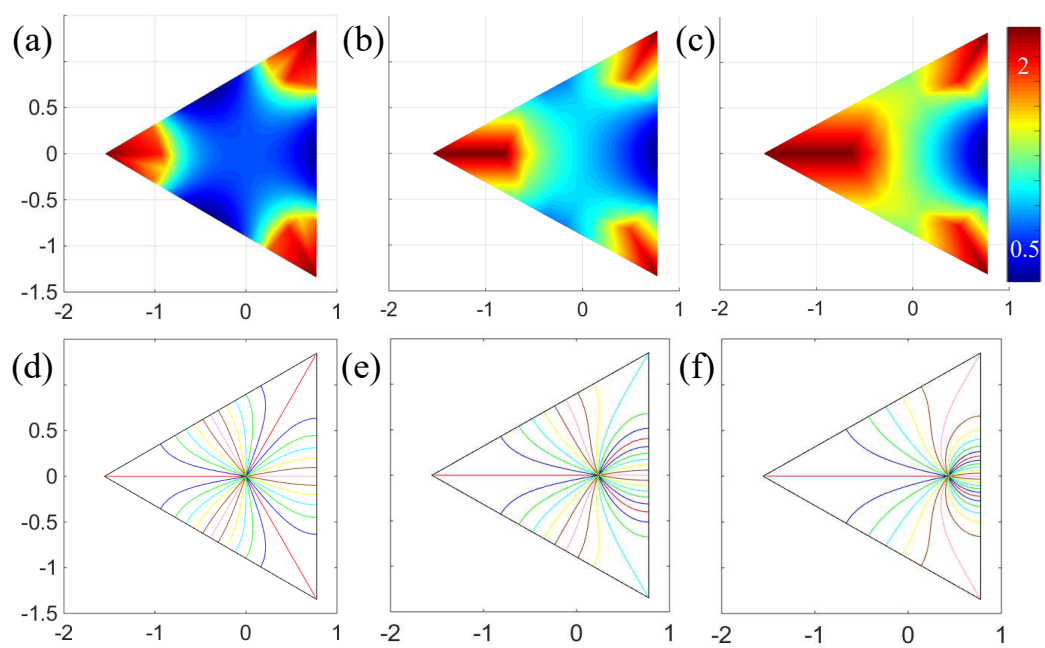

Figure 5.3: $\sqrt{K'/K}$ and ray paths for unchanged area for (a) and (d) $\phi = \pi/3$, (b) and (e) $\phi = \pi/2$, (c) and (f) $\phi = 2\pi/3$. The origins are located at $t = 0$, 0.2351 and 0.4315 in the transformed coordinates, respectively.

domain is not important at this stage since they are scalable to fit the general size of the GRIN lenses.

The conformal TA mapping yields a constant density distribution, the refractive index change merely resulted from the bulk modulus change. The presence of index change bends the directions of rays as shown in Fig. 5.3 for $\phi = \pi/3$, $\pi/2$ and $2\pi/3$ respectively. When the three points A, B and C divide the circumference of the circle equally, the numbers of rays exit from the three faces of the triangular domain are the same. When the arc length between A and B is longer, more rays are bent towards the AB face of the triangle.

With these material distributions, we can design cylindrical-to-plane wave lenses and make them directional, i.e. more energy radiate out from one of the three edges. Full wave simulations were conducted in COMSOL Multiphysics to demonstrate the idea of directional collimation. The background fluid outside the triangular region is water with density $\rho = 1000$ kg/m^3 and bulk modulus $K = 2.25$ GPa. The density of the effective medium in the triangle is the same as water $\rho' = 1000$ kg/m^3, the bulk modulus K' in each case is calculated using the distribution shown in Fig. 5.3. For convenience, the sizes of the triangles have the same number of the dimensions shown in Fig. 5.3 but the units are in meters. The monopole sources are placed at $t = 0$ m, 0.2351 m and 0.4315 m respectively. The collimation effects using effective medium are independent of frequency, here we only show the results at 3 kHz corresponding to different values of ϕ. Figure 5.4 clearly show that more energy radiate across the right face when angle ϕ is larger. Note that when $\phi \neq \pi/3$

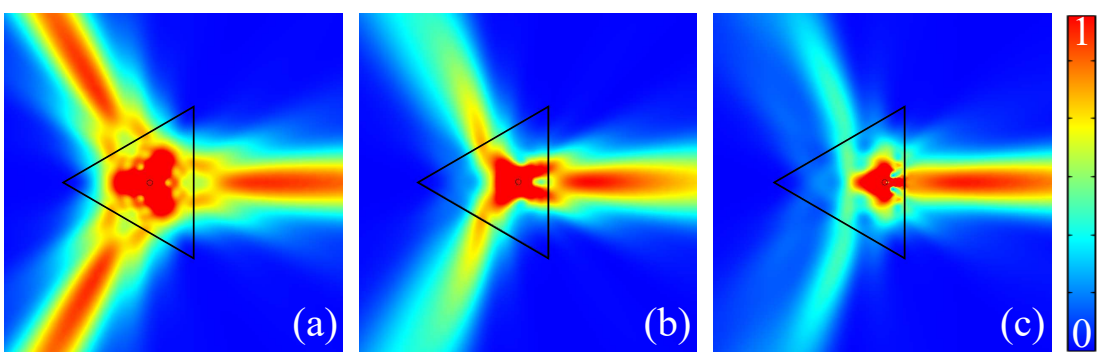

Figure 5.4: Simulated intensity at 3 kHz where (a) $\phi = \pi/3$, (b) $\phi = \pi/2$ and (c) $\phi = 2\pi/3$.

waves transmit through each face are still planar, but only the plane wave beam travel to the right propagate along the normal of the face.

5.3 Cylindrical-to-plane wave lenses using elastic shells

5.3.1 Unit cell design

In order to design a GRIN lens for $\phi = \pi/3$, we discretize the triangular region into 91 hexagons as shown in Fig. 5.5. The distance between two opposite edges of each hexagon is 2.2 cm, so that the unit cell size is similar to the square lens by [34]. The material properties (ρ' and K') in each hexagon are considered to be uniform and has the value at its center. Because of the symmetry, the unit hexagons are classified into 18 different types based on the distance to the center. The hexagon at the center of the lens is reserved for placing the monopole source.

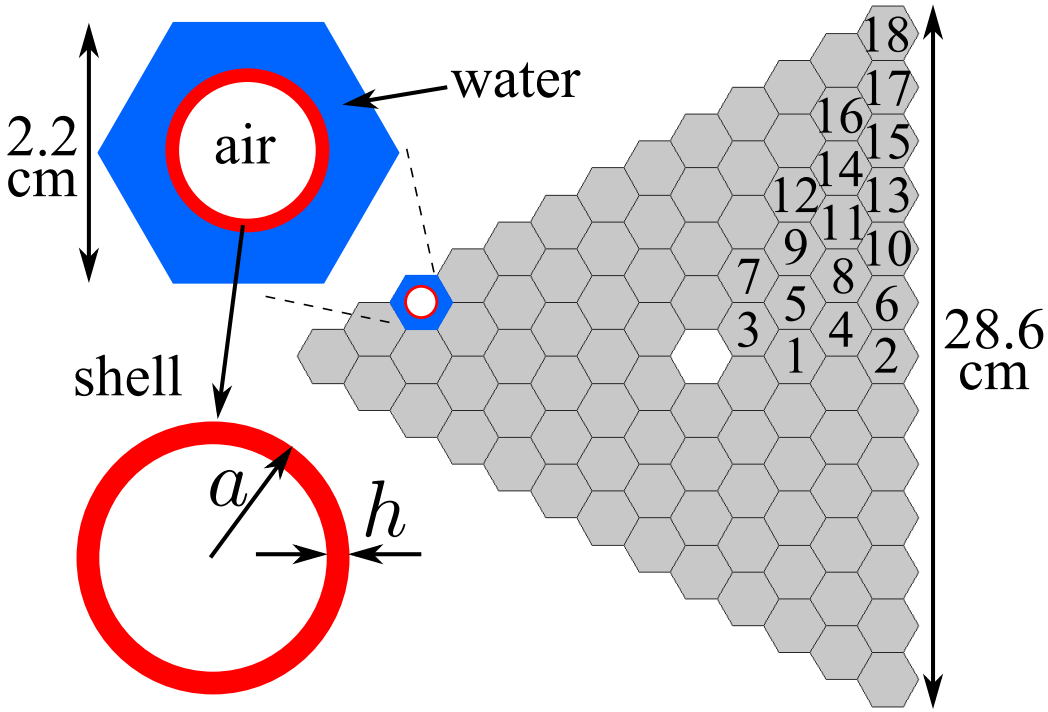

Figure 5.5: Discretization of the transformed domain ($\phi = \pi/3$).

To mimic the acoustic behavior of the discretized domain, water saturated elastic shells are introduced to match the material properties. The cylindrical shell has thickness h and outer radius a. The density of the shell material is denoted by ρ_s, shear modulus by μ_s and Poisson's ratio by ν_s. The effective bulk modulus of the empty shell can be easily extracted by solving the problem of uniform pressure loaded shell under plane strain condition [108],

while the effective density is simply an average of the total mass over the circular area. The effective properties of the shell are expressed as [34]

$$\begin{aligned} \rho_{\text{eff}} &= \big(2h/a - (h/a)^2\big)\rho_s, \\ K_{\text{eff}} &= \mu_s/\big(2(1-\nu_s)\rho_s/\rho_{\text{eff}} - 1\big). \end{aligned} \tag{5.8}$$

Consider the Ashby chart, see Fig. 5.6, which plots the range of effective properties for shells of different thickness to outer radius ratio h/a and various materials. In our GRIN lens

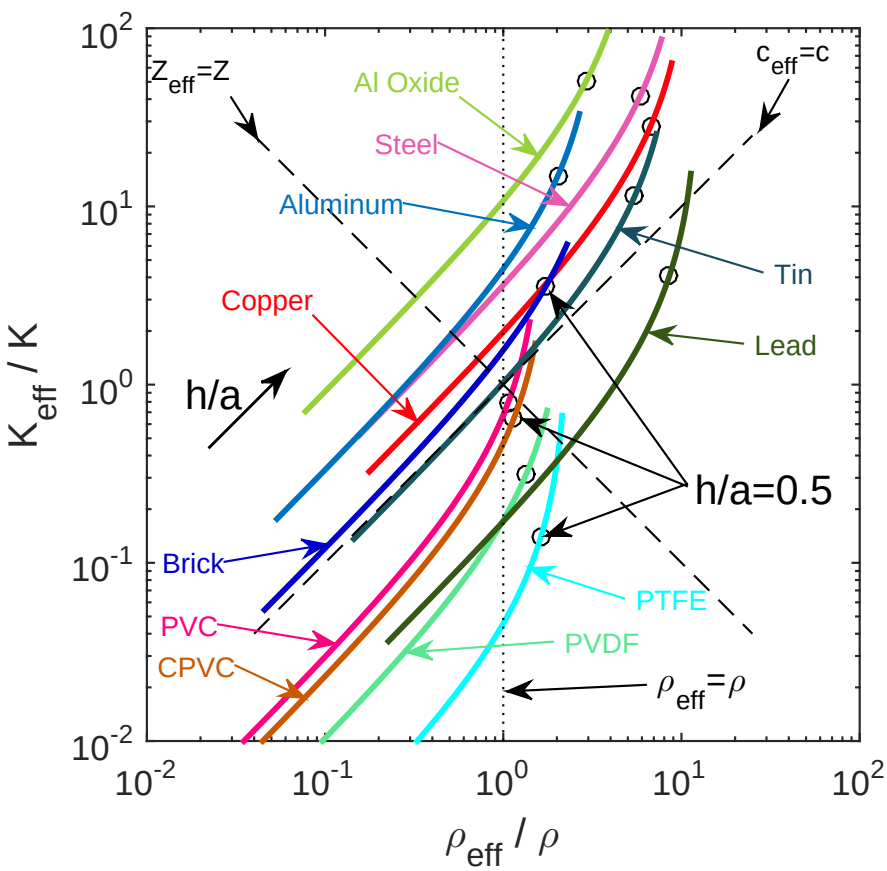

Figure 5.6: Effective properties normalized to water for shells using different materials. Each curve represents the effective properties as a function of the ratio h/a from small to large.

design, the transformed density is constant so that we need to pick materials and choose the ratio h/a along the vertical dotted line, which indicates $\rho_{\text{eff}} = \rho$. Eight different materials and the specific values of h/a for matching density to water are selected and listed in Table. 5.1.

Table 5.1: Selected materials for elastic shells. The values h/a are for matching effective density to water.

Material	ρ_s (kg/m^3)	E_s (GPa)	ν_s	K_{eff} (GPa)	h/a
PVC	1420	3.00	0.4	1.52	0.456
PVDF	1780	1.40	0.345	0.39	0.338
CPVC	1525	2.55	0.386	1.05	0.413
Tin	7300	54	0.33	2.31	0.071
Copper	8900	128	0.34	4.44	0.058
Steel	7800	210	0.3	8.14	0.061
Aluminum	2700	70	0.33	10.05	0.207
Al Oxide	3900	300	0.222	24.22	0.138

Then we fix the ratio h/a but change the outer radius a to change the filling fraction, so that the equivalent bulk modulus is changed and matched to the transformed material properties. The equivalent density ρ_{eq} and bulk modulus K_{eq} of the fluid-saturated shell are related to the shell volume fraction f as

$$\begin{aligned} \rho_{\text{eq}} &= (1-f)\rho + f\rho_{\text{eff}}, \\ K_{\text{eq}} &= \left((1-f)K^{-1} + fK_{\text{eff}}^{-1}\right)^{-1}. \end{aligned} \tag{5.9}$$

Note that the equivalent properties of the water saturated shells are the values to match the parameter distribution in the discretized triangle, i.e. ρ' and K'. In this case, h/a is chosen such that the effective and equivalent density are both the same as the density of water. Based on the selected materials from Table. 5.1, the material and geometric parameters of each shell corresponding to each discretized unit in Fig. 5.5 are calculated using Eq. (5.9) and listed in Table. 5.2.

5.3.2 Cylindrical-to-plane wave lens ($\phi = \pi/3$)

Here we report the full wave simulation results to demonstrate the collimation effects of the GRIN lens. This lens is comprised of 91 polymer and metal tubes from Table. 5.2. The shells are distributed in a hexagonal manner and form an triangular shape. The distance between the center of two adjacent tubes is 2.2 cm. All the tubes are surrounded by water with air filled in them. A monopole source is located at the center of the lens to radiate in all directions. Figure 5.7 shows the simulated pressure distribution of the triangular lens at three different frequencies within the *quasi-static* regime. The results clearly show that the

Table 5.2: Selected elastic shells for the GRIN lens ($\phi = \pi/3$). The labels correspond to the numbering in Fig. 5.5.

Material	h/a	a (mm)	f	K_{eq} (GPa)	label
CPVC	0.413	6.91	0.358	1.60	1
PVDF	0.338	6.61	0.327	0.88	2
PVC	0.456	9.04	0.613	1.74	3
CPVC	0.413	8.86	0.588	1.35	4
PVC	0.456	9.04	0.613	1.74	5
PVDF	0.338	5.66	0.240	1.05	6
PVC	0.456	7.17	0.385	1.90	7
PVC	0.456	9.04	0.613	1.74	8
Tin	0.071	8.00	0.480	2.25	9
PVC	0.456	9.04	0.613	1.74	10
Copper	0.058	7.74	0.449	2.89	11
Steel	0.061	8.01	0.481	3.45	12
Aluminum	0.207	8.50	0.541	3.88	13
Aluminum	0.207	10.47	0.821	6.20	14
Al Oxide	0.138	10.33	0.800	8.20	15 -18

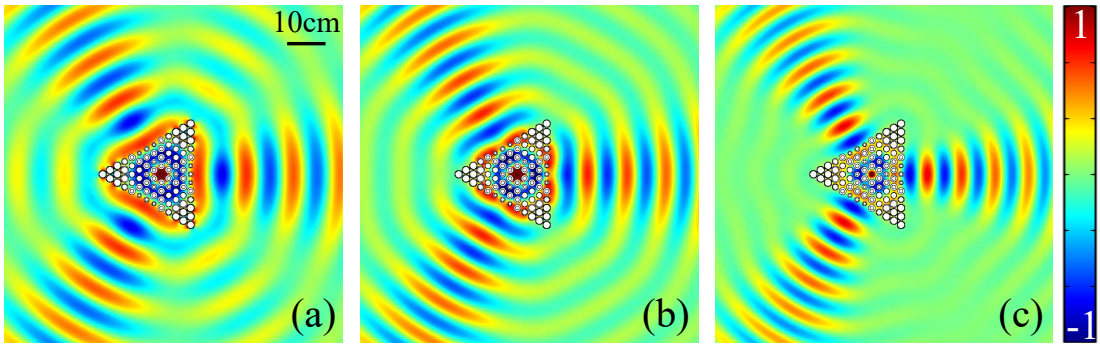

Figure 5.7: Simulated pressure at (a) 12.5 kHz, (b) 15 kHz and (c) 17.5 kHz.

cylindrical wavefront has been collimated into three identical lobes and radiate to the far field in the form of plane wave beams in different directions. This GRIN lens works over a broad range of frequency (10 kHz to 20 kHz) as long as the wavelength is greater than the unit cell size.

5.3.3 Bend more energy into one direction ($\phi = \pi/2$)

In practice, we may want to send more energy into one direction. The TA mapping derived in this chapter provides a way to manipulate the index distribution such that more energy comes out from one of the three faces. This can be simply done by choosing a larger value of

ϕ. Here we design another GRIN lens ($\phi = \pi/2$) using polymer and metal shells. The unit cell sizes are the same as the previous design, but more shells are added to provide smoother change of the index in a small area. The position of the monopole source is calculated by scaling the mapping to fit the new triangular region and finding the corresponding position of $t = 0.2351$. The design procedure follows Sec. 5.3.1. The simulated pressure distribution, see Fig. 5.8, confirms the idea that more energy radiates across the right side. A drawback

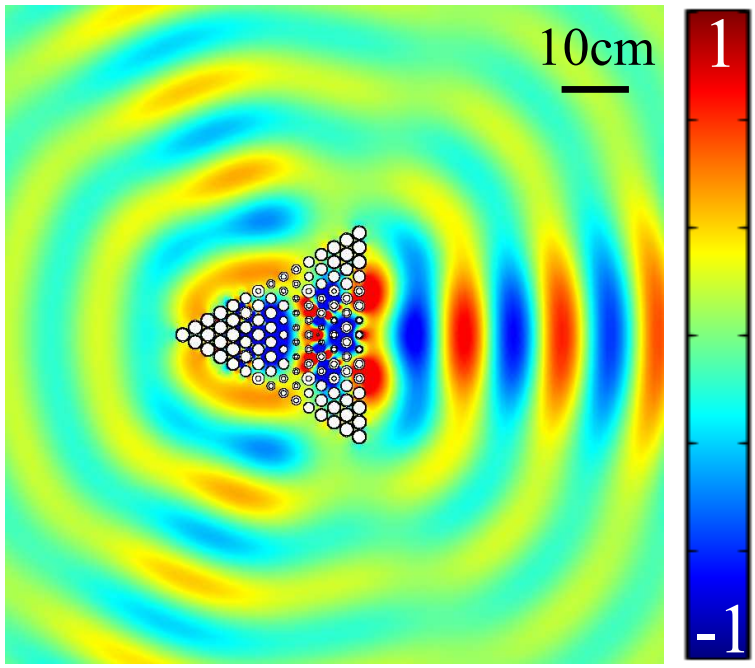

Figure 5.8: Simulated pressure at 10.5 kHz.

of this kind of shell based metamaterial is that the resonances of multiple shells might affect the performance near those frequencies. In the present case of $\phi = \pi/2$, the bandwidth is reduced because various types of shells are involved, which brings more resonances. This issue can be resolved by introducing internal substructures to suppress the low frequency resonances [34].

5.4 Discussion

We have introduced a new TA mapping from a circle to a triangle and designed two GRIN lenses for directional collimation. The TA mapping considered here is conformal such that the transformed material properties are isotropic. By choosing a for unchanged area and

setting the upper limit of bulk modulus to $3.65K$, we restricted the bulk modulus to an achievable range which makes it possible to design the devices. Taking advantage of the water saturated elastic tubes we designed two GRIN lenses, and demonstrated the broadband collimation effect using full wave simulations. The results clearly show that the first lens equally divides energy into three lobes, whereas the second one sends half of the energy to the AB face. In summary, the idea of leaving ϕ adjustable in the TA mapping provides a novel method to make cylindrical-to-plane wave lenses more directional.

Chapter 6

Bulk elastic wave control using metamaterials with aligned parallel plates

This chapter focuses on the design of GRIN lens, refractive and asymmetric transmission devices for elastic waves. The physics behind elastodynamic waves is more complicated because of the coupling of different types of waves, but brings into play more interesting phenomena. Climente *et al.* [109] designed a GRIN lens for flexural wave based on the local variation of the plate thickness. Morvan *et al.* [110] experimentally demonstrated negative refraction of transverse waves with a 2D PC of a square lattice of cylindrical cavities. Later, Pierre *et al.* [111] achieved negative refraction for antisymmetric Lamb waves with a similar design. The focusing of bending waves in perforated thin plates was realized by Farhat *et al.* [51] and Dubois *et al.* [52], respectively. Zhu *et al.* [112] experimentally demonstrated the negative refraction of longitudinal waves by an elastic metamaterial with chiral microstructure fabricated in a steel plate. Chang *et al.* [113] used a soft hyperelastic material to split longitudinal and shear waves. Zhu *et al.* [114] proposed a 1D PC with anti-symmetric and symmetric unit cells that shows one-way Lamb wave transmission for both A and S modes. Most of these articles are concerned with flexural or Lamb waves, while only a few of them discuss bulk waves in elastic bodies, namely, P-, SV- and SH-waves.

We model a solid with aligned parallel gaps as depicted in Fig. 6.1. The effect of the gaps is to make the solid material between them act like thin plates. Our approach to focusing, refraction and asymmetric transmission of elastic waves is based on the wave bearing properties of the plates. Broadband high transmission for refraction of elastic waves and multi-band high efficiency for asymmetric transmission are achieved. Similar to the idea of applying pre-compression differentially on granular chains to achieve phase delay [115], we vary the thickness of the plates but keep the lengths constant to achieve a

focusing effect. The properties of the plates also lead to the idea of splitting P-wave and SV-wave in an elastic body by using an array of aligned parallel gaps. Our approach to asymmetric P-wave transmission uses the combination of the free boundary of a half-space and an array of aligned parallel gaps to achieve high and low energy transmission in opposite propagation directions. The models are simple and can be formulated analytically using thin plate theory. The transmission and reflection coefficients are derived in closed form, which helps improve the performance of the metamaterial devices.

This chapter includes all of the results presented in our paper [2]. This chapter is organized as follows. The analytical model for predicting the transmission and reflection of normally incident P- and SV-waves are developed in Sec. 6.1. The analytical results are compared with the simulation, and modified by introducing a empirical factor. In Sec. 6.2, we designed a metamaterial device for asymmetric transmission by employing mode conversion at a free boundary. In Sec. 6.3, we show a GRIN device for focusing SV-wave. The elastic prism for splitting SV- and P-waves is demonstrated in Sec. 6.4. Conclusions are presented in Sec. 6.5.

6.1 Transmission and reflection at normal incidence

6.1.1 Governing equations

We consider the configuration of Fig. 6.1a, in which an array of plates are connected to and separate two half-spaces. The configuration can be viewed as a homogenous solid with aligned thin gaps or cracks. At each of the junctions, the SV-wave in the half-space couples with the flexural wave on the plates, and the P-wave in the half-space couples with the compressional wave. In other words, an incident SV-wave (or P-wave) from the left side travels through the plate in the form of a flexural wave (or longitudinal wave), then transmits into the right side as SV-wave (or P-wave). To model and calculate the SV-wave (or P-wave) transmission and reflection coefficients, we only need to consider a single plate element connected between two half-spaces, as shown in the boxed region in Fig. 6.1b, because of the periodicity in the vertical direction. We model and formulate the problem using Kirchhoff plate theory which holds for long-wavelength flexural waves on thin plates.

In this chapter we focus on the frequency range in which the thin plate assumption is valid. Together with the boundary conditions: displacement, (rotation angle) and force continuity at the two ends, we can establish six (or four) equations with six (or four) unknowns to solve for the transmission and reflection coefficients.

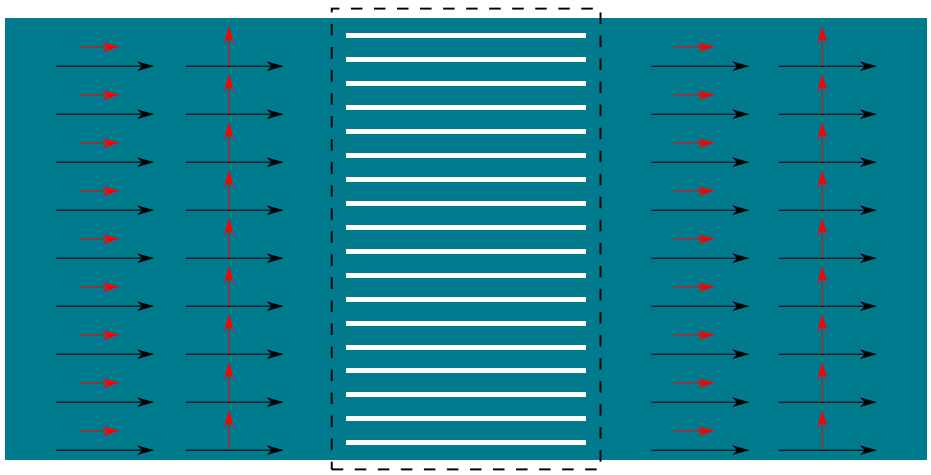

(a)

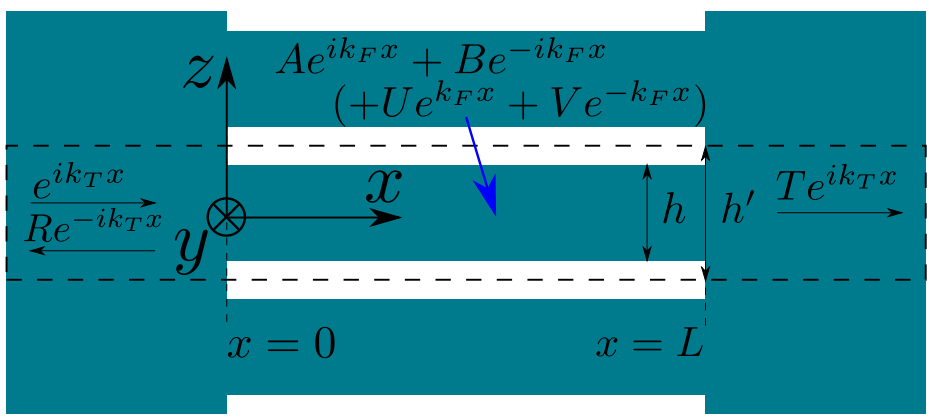

(b)

Figure 6.1: Two-dimensional schematic of aligned parallel gaps. (a) P- and SV-waves transmit through aligned parallel plates. The black arrows represent the direction of propagation, the red arrows represent the direction of particle motion. (b) The geometric parameters and multiple wave types on the plates.

The density of the material is denoted by ρ, the Young's modulus by E, the shear modulus by μ, and the Poisson's ratio by ν. We also define the Cartesian coordinate system as shown in Fig. 6.1b, where x is along the lateral direction of the plate, y is into the plane and perpendicular to x, and z is upward. The displacements in each direction

are denoted as u, v and w, respectively. The thickness of the plate is denoted by h, the width of the gap by a ($a \ll h$), and the thickness of the unit structure in the boxed region in Fig. 6.1b is $h' = h + a$. The bending stiffness of the plate is $D = Eh^3/12(1-\nu^2)$. We assume the incident plane wave is independent of y-direction, i.e. there is no y-dependent term. The governing equations for flexural and longitudinal waves in the thin plate are

$$\begin{aligned} D\frac{\partial^4 w}{\partial x^4} - \rho h\omega^2 w = 0, \\ \frac{E}{1-\nu^2}\frac{\partial^2 u}{\partial x^2} + \rho\omega^2 u = 0, \end{aligned} \tag{6.1}$$

where ω is the radial frequency. Time harmonic dependence $e^{-i\omega t}$ is assumed. The phase speeds of flexural and longitudinal waves (c_F, c_L) on the plate, and the phase speeds of SV- and P-waves (c_T, c_P) in the exterior body are

$$\begin{aligned} c_F &= \left(\frac{Eh^2\omega^2}{12\rho(1-\nu^2)}\right)^{1/4}, \\ c_L &= \sqrt{\frac{E}{\rho(1-\nu^2)}}, \\ c_T &= \sqrt{\frac{E}{2\rho(1+\nu)}}, \\ c_P &= \sqrt{\frac{E(1-\nu)}{\rho(1+\nu)(1-2\nu)}}. \end{aligned} \tag{6.2}$$

6.1.2 Transmission and reflection of a normally incident P-wave

To calculate the transmission and reflection coefficients of P-waves, we assume the amplitude of the displacement of the incident wave as 1, reflected wave as R, transmitted wave as T, and the amplitude of displacement on the plate as A and B, the displacements are expressed as

$$u = \begin{cases} e^{ik_P x} + Re^{-ik_P x}, & x < 0, \\ Ae^{ik_L x} + Be^{-ik_L x}, & 0 < x < L, \\ Te^{ik_P(x-L)}, & x > L, \end{cases} \tag{6.3}$$

where $k_P = \omega/c_P$ and $k_L = \omega/c_L$ are the wavenumbers of P-wave in the exterior body and longitudinal wave in the plate. The compressional force in the exterior body is $F_x = h'\sigma_{xx} = Eh'(\partial u/\partial x)$, and the compressional force in the plate is $F_x = Eh(\partial u/\partial x)$. The four

z-averaged boundary conditions are continuity of displacement and compressional force at $x = 0$ and $x = L$, yielding the system of equations:

$$\left.\begin{aligned} 1 + R &= A + B, \\ 1 - R &= \frac{h}{h'}\frac{k_L}{k_P}(A - B), \\ T &= Ae^{ik_L L} + Be^{-ik_L L}, \\ T &= \frac{h}{h'}\frac{k_L}{k_P}(Ae^{ik_L L} - Be^{-ik_L L}). \end{aligned}\right\} \tag{6.4}$$

The transmission and reflection coefficients for the incident P-wave are then

$$T = \frac{4\alpha k_P k_L e^{ik_L L}}{(k_P + \alpha k_L)^2 - (k_P - \alpha k_L)^2 e^{i2k_L L}}, \tag{6.5}$$

$$R = \frac{\left(k_P^2 - \alpha^2 k_L^2\right)(1 - e^{2ik_L L})}{(k_P + \alpha k_L)^2 - (k_P - \alpha k_L)^2 e^{i2k_L L}}, \tag{6.6}$$

which also satisfy $|T|^2 + |R|^2 = 1$. It is easy to show that total transmission, i.e. $|T| = 1$, requires either $k_P - \alpha k_L = 0$ or $e^{i2k_L L} = 1$. The first occurs over all frequency range when $\alpha = k_P/k_L = \sqrt{1 - 2\nu}/(1 - \nu)$ and the others at ω_n, $n = 1, 2 \cdots$, where

$$\omega_n = \frac{n\pi}{L}\sqrt{\frac{E}{\rho(1 - \nu^2)}}, \quad n = 1, 2, 3 \cdots, \tag{6.7}$$

where ω_n is the radial frequency corresponding to each n. However, $\alpha = k_P/k_L$ indicates that total transmission can be achieved by choosing ν, this only works for low Poisson's ratio material since we are only interested in structures with small gap width.

As an example, we consider an infinite aluminum domain ($E = 70$ GPA, $\nu = 0.35$, and $\rho = 2700$ kg/m^3) with an infinite array of aligned equidistant parallel gaps as shown in Fig. 6.1a. The thickness and length of each plate are $h = 0.02$ m and $L = 0.2$ m, respectively. The geometric parameter $h' = 0.021$ m is shown in Fig. 6.1b. From Fig. 6.2, we find that the transmission is close to 1 over all frequencies so that P-wave transmits through these effective plates with high efficiency.

6.1.3 Transmission and reflection of a normally incident SV-wave

To solve for the transmission and reflection coefficients of SV-wave, we assume the amplitude of the displacement of the incident SV-wave as 1, reflected wave as R, transmitted wave as

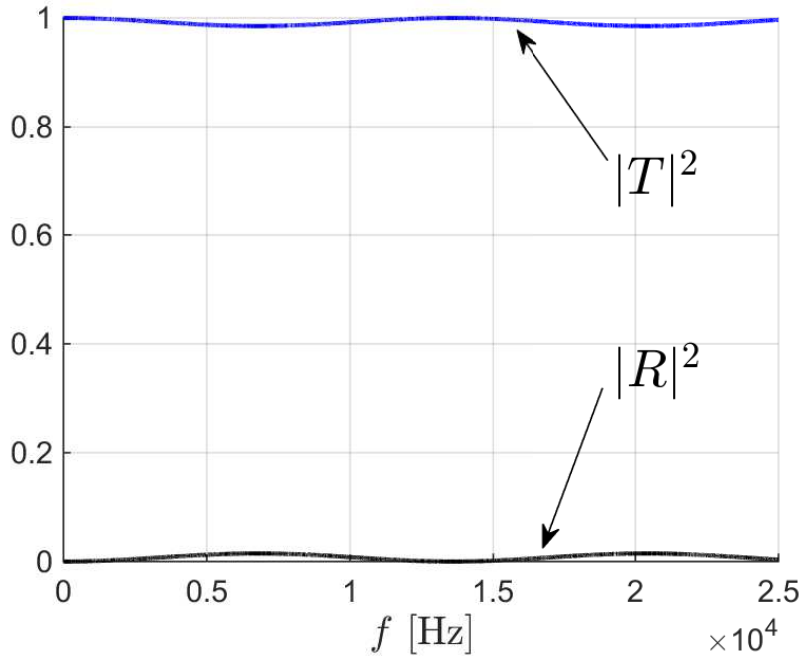

Figure 6.2: Transmission and reflection spectrum for a normally incident P-wave. The blue line indicates the energy transmission coefficient, the black line indicates the energy reflection coefficients.

T, and on the plate as A, B, U and V, see Fig. 6.1b, so that

$$w = \begin{cases} e^{ik_T x} + Re^{-ik_T x}, & x < 0, \\ Ae^{ik_F x} + Be^{-ik_F x} & \\ \qquad + Ue^{k_F x} + Ve^{-k_F x}, & 0 < x < L, \\ Te^{ik_T (x-L)}, & x > L, \end{cases} \tag{6.8}$$

where $k_F = \omega/c_F$ and $k_T = \omega/c_T$ are the flexural and shear wavenumbers. Although σ_{xx} and σ_{yy} exist in the plate, they do not contribute to the force on the plate since $\int_{-h/2}^{h/2} \sigma_{xx} dz = -\int_{-h/2}^{h/2} Ez/(1-\nu^2)(\partial^2 w/\partial x^2) dz = 0$ and $\int_{-h/2}^{h/2} \sigma_{yy} dz = -\int_{-h/2}^{h/2} Ez\nu/(1-\nu^2)(\partial^2 w/\partial x^2) dz = 0$. Since there is no y-dependence in the governing equation the shear force per unit length in y-direction is $Q = \int_{-h/2}^{h/2} \sigma_{xz} dz = -D(\partial^3 w/\partial x^3)$. The shear force in the exterior body is $Q = h'\sigma_{xz} = \mu h'(\partial w/\partial x)$. The six z-averaged boundary conditions are continuity of displacement, rotation angle and shear force at $x = 0$ and $x = L$, which

imply the following system of equations:

$$\left.\begin{aligned}
1+R =& A+B+U+V,\\
1-R =& \frac{k_F}{k_T}(A-B-iU+iV),\\
1-R =& \frac{hk_T}{h'k_F}(A-B+iU-iV),\\
T =& Az^i+Bz^{-i}+Uz+Vz^{-1},\\
T =& \frac{k_F}{k_T}\big(Az^i-Bz^{-i}-iUz+iVz^{-1}\big),\\
T =& \frac{hk_T}{h'k_F}\big(Az^i-Bz^{-i}+iUz-iVz^{-1}\big),
\end{aligned}\right\} \tag{6.9}$$

with $z = e^{k_F L}$ so that $z^{\pm i} = e^{\pm i k_F L}$. This system gives the transmission and reflection coefficients but the explicit expressions are long. We can split the solutions into symmetric and anti-symmetric modes which reduces the system to two 3×3 systems. This leads to

$$T = \frac{1}{2}(R_S - R_A)e^{-ik_T L}, \tag{6.10}$$

$$R = \frac{1}{2}(R_S + R_A)e^{-ik_T L}, \tag{6.11}$$

where the reflection coefficients R_S and R_A are

$$R_S = \frac{\left(\frac{\tau}{\alpha}-\frac{1}{\tau}\right)\frac{1}{t_h}+\left(\frac{\tau}{\alpha}+\frac{1}{\tau}\right)\frac{1}{t}+i2}{\left(\frac{\tau}{\alpha}-\frac{1}{\tau}\right)\frac{1}{t_h}+\left(\frac{\tau}{\alpha}+\frac{1}{\tau}\right)\frac{1}{t}-i2}, \tag{6.12}$$

$$R_A = \frac{\left(\frac{\tau}{\alpha}-\frac{1}{\tau}\right)t_h-\left(\frac{\tau}{\alpha}+\frac{1}{\tau}\right)t+i2}{\left(\frac{\tau}{\alpha}-\frac{1}{\tau}\right)t_h-\left(\frac{\tau}{\alpha}+\frac{1}{\tau}\right)t-i2}, \tag{6.13}$$

with $\tau = k_F/k_T$, $\alpha = h/h'$, $t = \tan(k_F L/2)$ and $t_h = \tanh(k_F L/2)$. Note that R_S and R_A are both of unit magnitude, which implies that the transmission and reflection coefficients satisfy $|T|^2 + |R|^2 = 1$. Total transmission therefore occurs when $R_S + R_A = 0$. For small gap width, i.e. $\alpha \approx 1$, $|T| = 1$ is obtained if $k_F = k_T$ or if either of the following holds

$$\tan(k_F L/2) \pm \tanh(k_F L/2) = 0. \tag{6.14}$$

However, $k_F = k_T$ gives a single high frequency at which Kirchhoff plate theory does not hold. This single frequency is not in the frequency range of interest since we only consider long-wavelength flexural waves, i.e. $\lambda \gg h$. The frequencies satisfying Eq. (6.14) correspond to the symmetric $(+)$ and anti-symmetric $(-)$ modal frequencies for a plate of length L fixed at both ends, i.e. subject to the boundary conditions $w = 0$ and $\partial w/\partial x = 0$.

We use the same structure and material as the example of P-wave transmission. Figure 6.3 shows that flexural waves are quite dispersive on plates, it is also clear that the transmission tends to unity at high frequency.

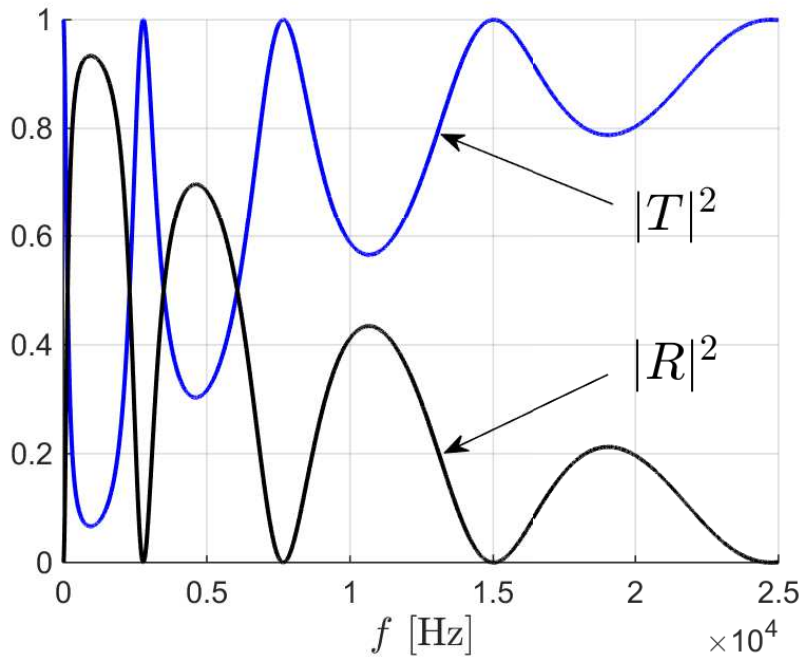

Figure 6.3: Transmission and reflection spectrum for a normally incident SV-wave. The blue line indicates the energy transmission coefficient, the black line indicates the energy reflection coefficients.

6.1.4 Discussion and improved solution for SV-wave

The transmission spectrum for SV- and P-waves obtained using our analytical model and full wave FEM simulations are shown in Fig. 6.4 for comparison. For a normally incident SV-wave, the low frequency behavior of the analytical solution match well with simulation result, this indicates that our boundary condition assumptions are correct. The transmission peaks ($|T| = 1$) shift at higher frequencies, this can be understood as the neck effect at the junction between plate and half space changes the effective length of the plates. On the other hand, the analytical model for P-wave is in good agreement with full FEM simulations, it is obvious that the transmission peaks match well in frequency. The variances of the lowest values of the transmission coefficients can be understood as resulted from the difference between the areas at the junctions. However, this is not of significant importance in this

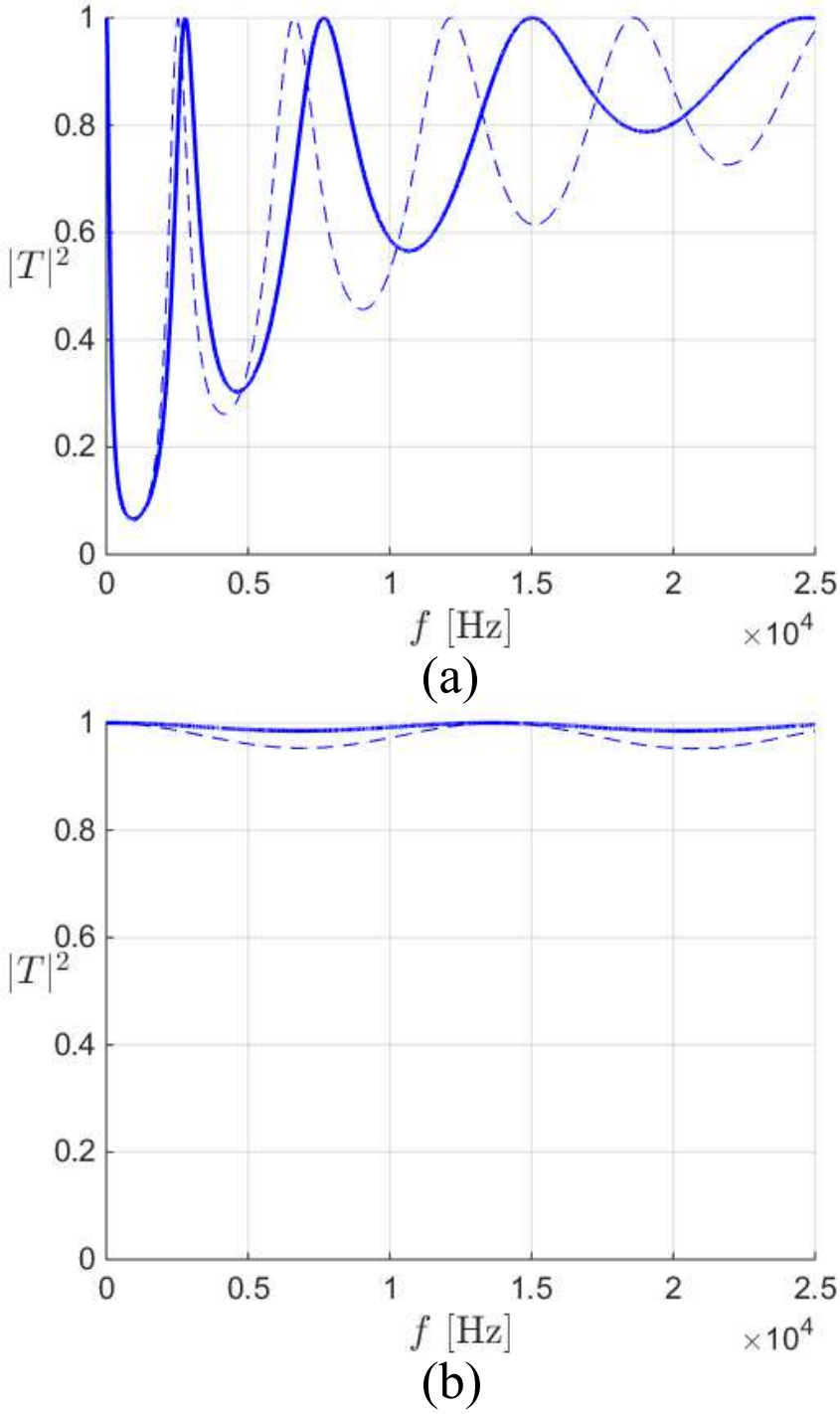

Figure 6.4: Comparison of the analytical solution (solid line) and full FEM simulation results (dashed line) for incident (a) SV-wave and (b) P-wave.

chapter since the transmission of P-wave tends to unity at all frequencies.

Since the analytically calculated P-wave transmission coefficient matches well with simulation results and is always high as long as the gap width a is small, i.e. $h/h' \approx 1$, we only consider an improved analytical solution for SV-wave incidence. We introduce an empirical end-effect term β to represent the effective length of the plate $L' = (1+\beta)L$ and replace the L in our original model. The same geometry and the same material properties as the previous example are used to demonstrate how the modification works. The full wave FEM simulation is done using plate with $h = 0.02$ m and $L = 0.2$ m. Practically, L' is the length of the plate in the analytical model when we design a metamaterial, but L is the length which will be used in FEM simulation. By iterating the value of β, the analytical solution can be matched better to the full FEM solution at higher frequency range. Figure 6.5 shows good agreement by taking $\beta = 0.07$. This value of β only works for the parameters

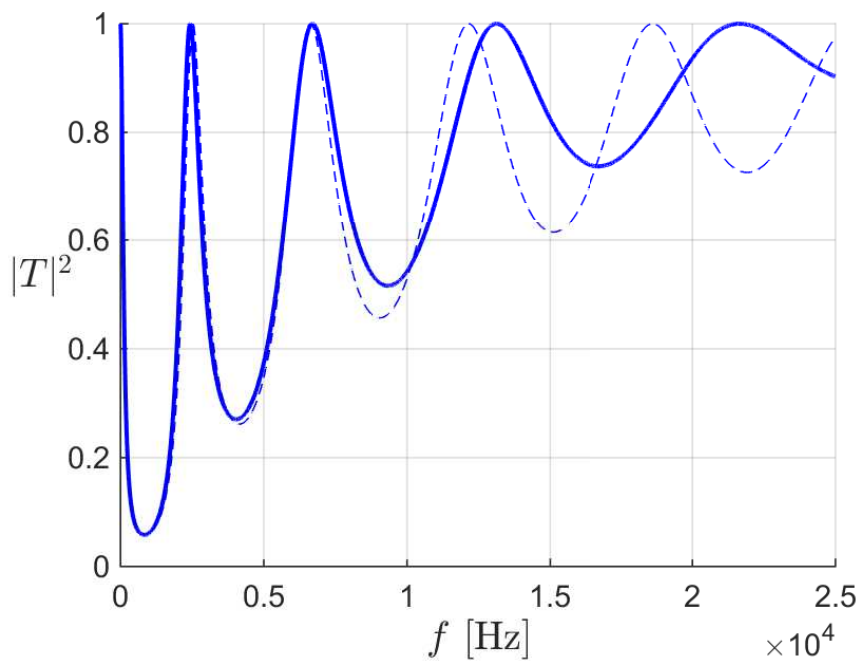

Figure 6.5: Comparison of the improved analytical solution (solid line) and simulation results (dashed line).

used in this example, new FEM simulations are required to find β for other parameter sets. However, the analytical technique is still important since it helps understand the physics behind the model and provides an initial parameter set in our design. Alternatively, we can

seek modification in simulations by changing the length of plates using $L = L'/(1+\beta)$.

6.2 Metamaterial for asymmetric transmission of elastic waves

6.2.1 Mode conversion at free boundary

The asymmetric transmission effect of P-wave is investigated in a solid with a flat free surface. As shown in Fig. 6.6a the energy carried by the incident P-wave from the left side at a specific angle θ_P cannot transmit through the parallel gaps, and therefore will not be detected beyond them. However, if the P-wave is incident from the right side of the white slits at the angle θ'_P as shown in Fig. 6.6b, the energy will transmit to the left side efficiently. This transmission asymmetry can be achieved when the P-wave is incident from the left side at a critical incident angle, at which total conversion to SV-wave occurs. An array of parallel gaps perpendicular to the propagation direction of the reflected SV-wave can stop the SV-wave but will let P-wave incident from the right side travel through. In this section, we show the equations for mode conversion, and find the critical angle for total conversion from P- to SV-wave, which will be used in the design of the asymmetric transmission device.

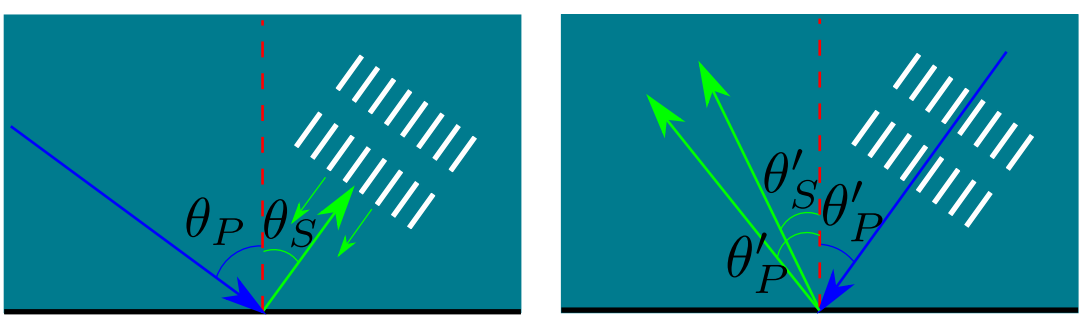

(a) (b)

Figure 6.6: Asymmetric transmission. The horizontal black line represents the free boundary of a half-space, the rectangular white slits represent gaps, lines with arrow indicate the propagation direction.

Assuming an incident P-wave at angle θ_0 with respect to the surface normal and amplitude A_0, the amplitudes of the reflected P- and SV-waves, A_1 and A_2, are given by Eqs.

(5.52) and (5.53) in Ref. [116] as

$$\frac{A_1}{A_0} = \frac{\sin 2\theta_0 \sin 2\theta_2 - \kappa^2 \cos^2 2\theta_2}{\sin 2\theta_0 \sin 2\theta_2 + \kappa^2 \cos^2 2\theta_2}, \tag{6.15}$$

$$\frac{A_2}{A_0} = \frac{2\kappa \sin 2\theta_0 \cos 2\theta_2}{\sin 2\theta_0 \sin 2\theta_2 + \kappa^2 \cos^2 2\theta_2}, \tag{6.16}$$

where $\kappa = c_P/c_T = \sqrt{2(1-\nu)/(1-2\nu)}$ from Eq. (6.2), and θ_2 is the SV-reflection angle: $\sin\theta_2 = \kappa^{-1}\sin\theta_0$. Figure 6.7 shows the P-wave reflection coefficient. Setting $A_1/A_0 = 0$

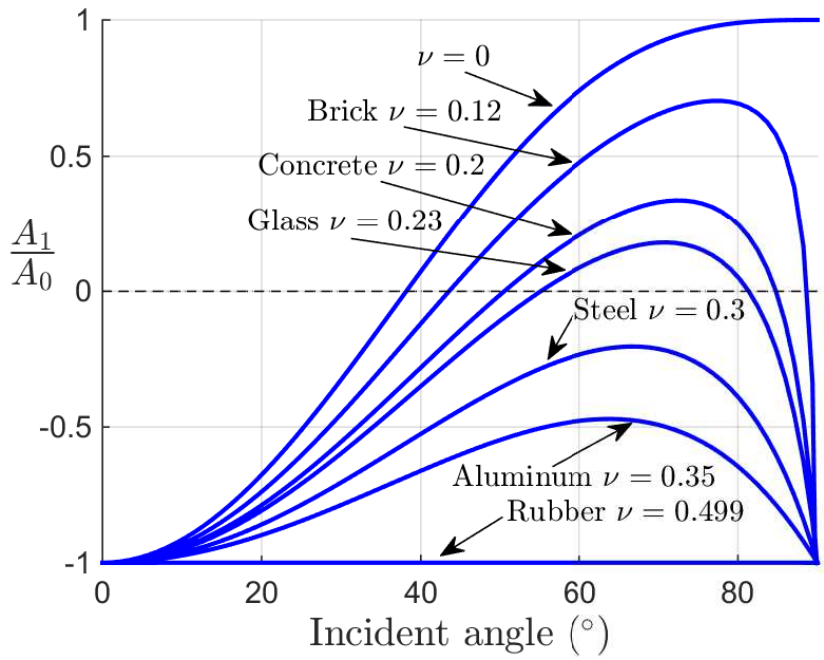

Figure 6.7: Amplitude ratio between incident and reflected P-wave of different materials, from Eq. (6.15).

defines the critical incident angle $\theta_0 = \theta_P$ for total conversion from P-wave to SV-wave.

For example, in a half-space made of material with the properties of brick ($E = 24$ GPa, $\nu = 0.12$ and $\rho = 2300$ kg/m^3), the critical angle for total P-to-SV conversion is $\theta_P = 43.5°$, with SV reflection angle $\theta_S = 26.9°$. The energy plot from full FEM simulation is shown in Fig. 6.8b and matches well with the theoretical prediction.

6.2.2 Simulation of the asymmetric transsmison

Figure 6.8 shows that brick-like material is very promising for the application of asymmetric elastic transmission. The critical angle for total conversion is large, providing enough space

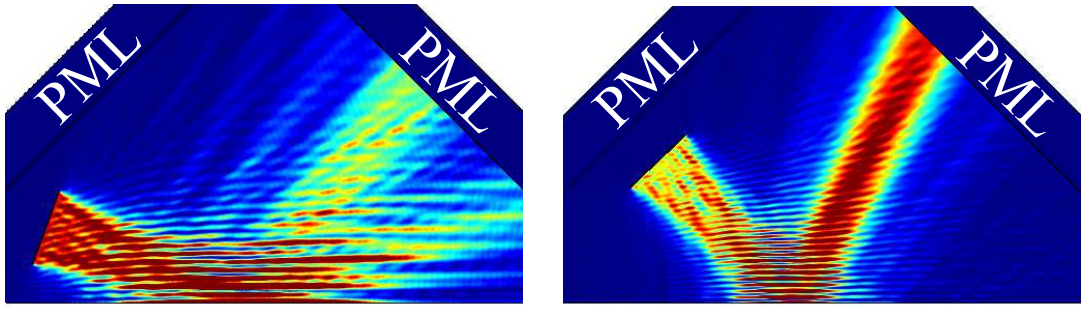

(a) (b)

Figure 6.8: Mode conversion of P-wave at free boundary (bottom of the simulation domain) in brick without slits/gaps. (a) P-wave incidence from left side at non-critical angle $\theta_0 = 70°$. (b) P-wave incidence from left side at critical angle $\theta_0 = \theta_P$ $(= 43.5°)$.

to place an array of rectangular gaps as shown in Fig. 6.6. Using brick as the material, we design an array of plates/gaps to stop SV-wave but let P-wave transmit through. The dimensions of each gap is 0.001 m wide and 0.5 m long, and the thickness of the plate between gaps is 0.005 m. The gaps are aligned so that the angle between the normal of the gap array and the normal of the free boundary is $\theta_S = 26.9°$. The horizontal line at the bottom of the simulation domain is the free boundary of the half-space. Figure 6.9a shows high energy reflection ($|T|^2 < 9\%$) for P-wave incidence from the left side, Fig. 6.9b shows high energy transmission ($|T|^2 > 94\%$) for P-waves incident from the right side.

6.3 Elastic GRIN lens for focusing SV-wave

6.3.1 Diffraction and Huygens-Fresnel principle

We next design a GRIN lens, as depicted in Fig. 6.10a, to focus SV-waves. The white strips are thin gaps, both of the ends are aligned vertically so that the effective plates have the same length. However, the thicknesses of the plates are allowed to vary based on the fact that flexural waves travel faster in thicker plates so that diffraction occurs earlier in thicker plates. Assuming circular wavefront radiating from the right end of each plate, the transmitted SV-wave intersect at the focal point according to Huygens' principle. The physics behind the focusing effect is based on diffraction effect similar to that in the generation of sound bullets [115]. The GRIN lens is designed by first selecting the thickness

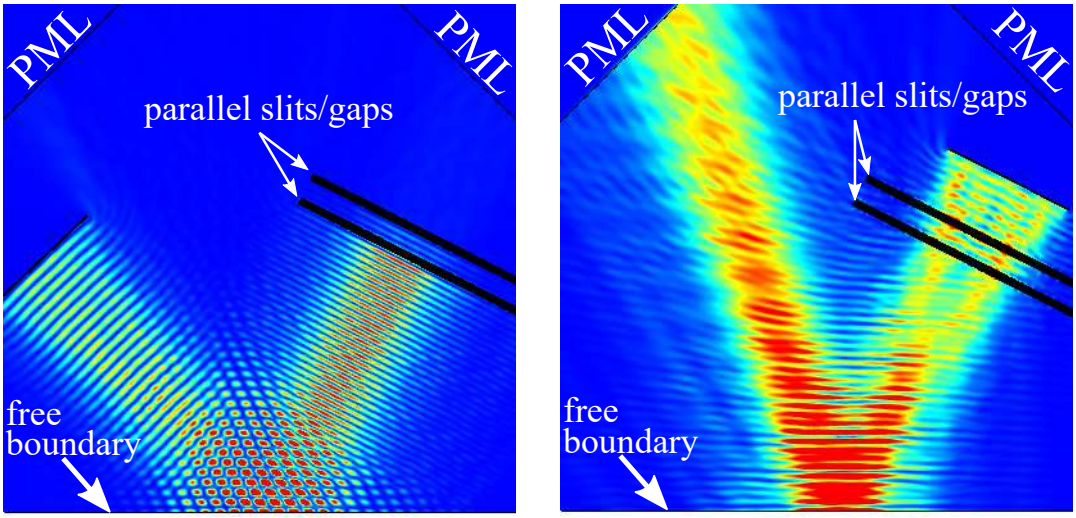

(a) (b)

Figure 6.9: Asymmetric transmission effect at $f = 21.6$ kHz. (a) P-wave incident from the left side with $\theta_0 = \theta_P$ $(= 43.5°)$. (b) SV-wave incident from the right side with $\theta_0 = \theta_S$ $(= 26.9°)$.

h_1 and length L for the center plate, and choosing the distance d from the focal point to the end of the center plate at a particular frequency f. The gap width a is fixed. The total time for a flexural wave traveling from one end of a plate to the other end is $t_F = L/c_F$. As shown in Fig. 6.10b, rays of the incident SV-wave from the left side travel along different paths but arrive at the focal point simultaneously. We formulate the relations between the thickness of the center plate and other plates as

$$\frac{\sqrt{h_{\text{total}}^2 + d^2} - d}{c_T} = \frac{L}{c_{F_1}} - \frac{L}{c_{F_i}}, \tag{6.17}$$

where c_{F_1} is the flexural wave speed in the center plate and depends on h_1, c_{F_i} is the flexural speed in the ith plate and depends on the thickness h_i, h_{total} is the distance from the neutral line of the center plate to the neutral line of the ith plate which is accumulated by adding the thickness of each plate and width of gaps. Note that this type of lens is designed at a certain frequency for a chosen focal point, the focal distance will change if the frequency is changed.

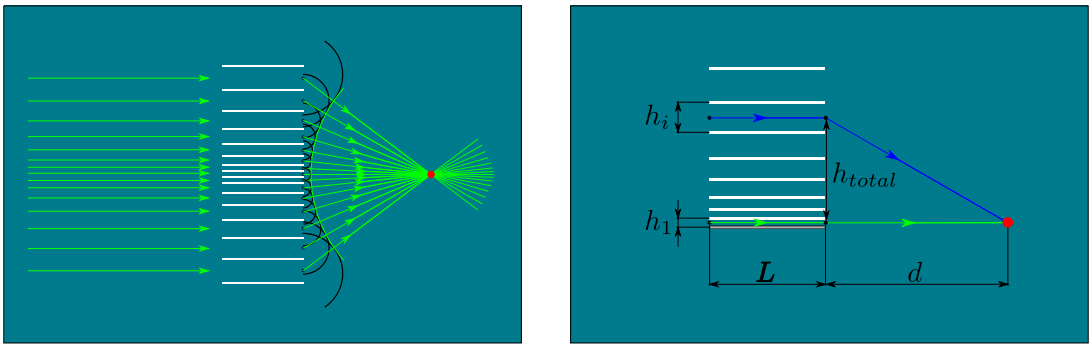

(a) (b)

Figure 6.10: GRIN lens of a solid with parallel gaps. (a) Ray pathes showing the focusing effect. (b) Relations of the geometric parameters.

6.3.2 Simulation of the focusing effect

Aluminum (E = 70 GPA, ν = 0.33, and ρ = 2700 kg/m^3) is used as the background material in our example. The width of each gap is $a = 0.001$ m, the length of each effective plate between gaps is chosen as $L_1 = 0.2$ m, the thickness of the center plate is $h_1 = 0.01$ m. The focal point is designed to be $d = 0.2$ m away from the end of the center plate at 40 kHz. The thicknesses of other plates are calculated using Eq. (6.17). Since the plate thicknesses are varying, the end-effect correction for the effective plate lengths are also different. We take the same value of the modification term β for every plate for convenience, and iterate its value to achieve optimal focusing effect. The focal point in Fig. 6.11(c) is roughly 0.25 m away from the edge of plate array. Figure 6.11 shows that the focal point moves away from the plate array when the frequency increases, this is due to the phase speed of the flexural wave changing with frequency so that the phase gradient of the transmitted SV-wave also changes.

6.4 Elastic prism for splitting SV- and P-waves

6.4.1 Wave speeds and refractive index

In this section, we design refractive devices that steer SV- and P-waves in different directions to split them from each other. The refractive devices are based upon a solid with aligned parallel gaps as shown in Fig. 6.12, in which the thin white strips are thin gaps with left end

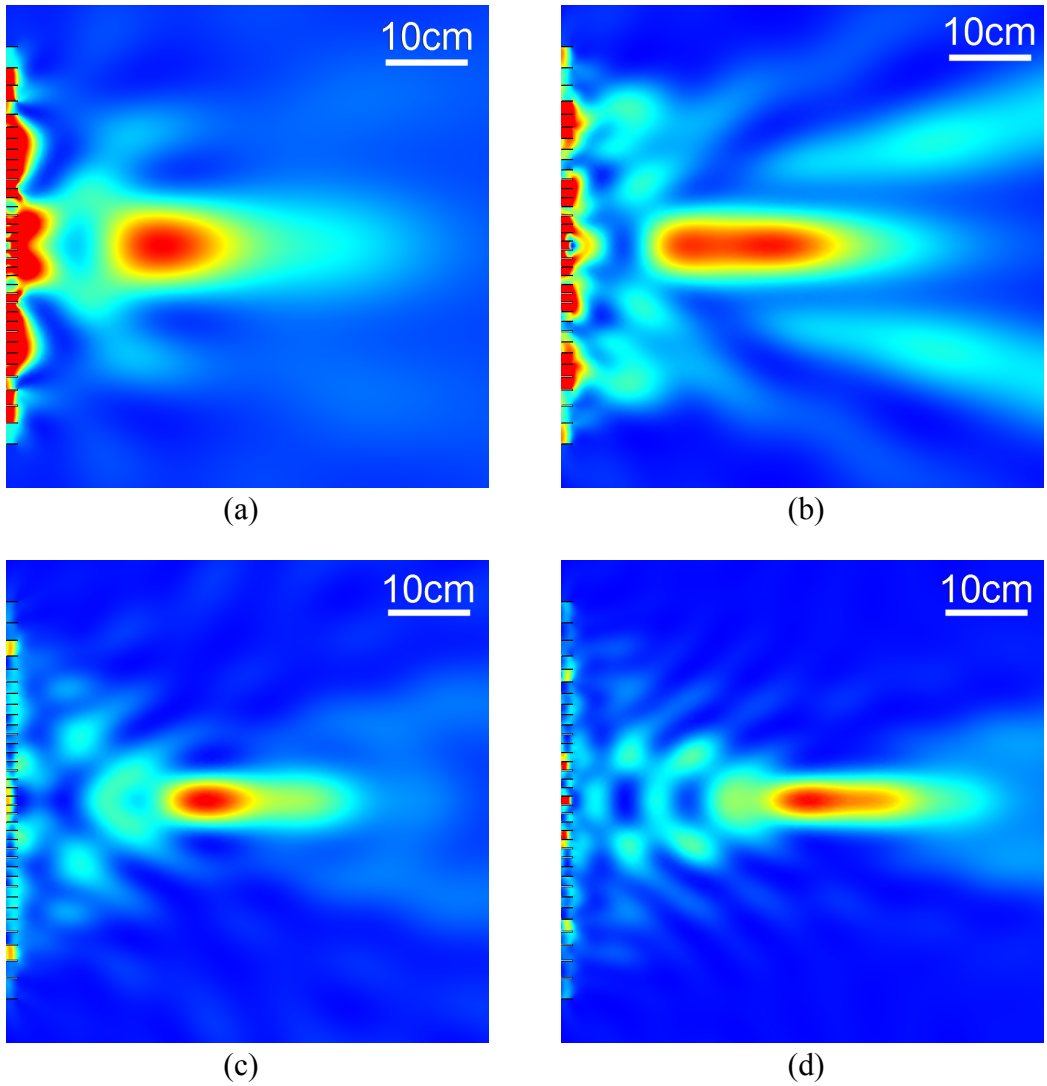

Figure 6.11: Focusing of SV-wave by GRIN lens with $\beta = -0.048$ at (a) 20 kHz, (b) 30 kHz, (c) 40 kHz and (b) 50 kHz.

aligned vertically and the right end aligned with a slope. The effective plates have different lengths and thicknesses. Figure 6.12a illustrates the idea of steering SV- and P-waves in different directions. The long arrows indicate the propagation directions, the short arrows indicate the direction of particle motion, i.e. they are perpendicular to the propagation direction of SV-wave and parallel to the propagation direction of P-wave. Zero-refraction of SV-wave and positive refraction of P-wave are achieved based on the different wave speeds of the two wave and by selecting plate members that have high transmission for both SV- and P-waves.

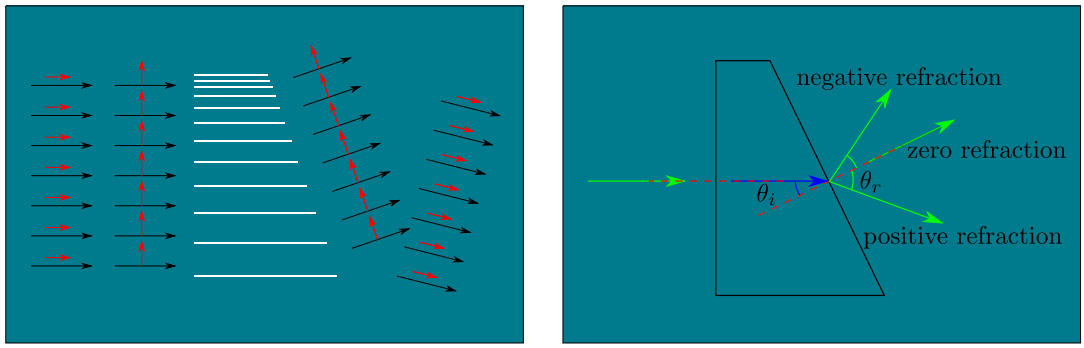

(a) (b)

Figure 6.12: Refraction of elastic waves. (a) Propagation directions of P- and SV- waves through the prism. The black arrows indicate the propagation direction, the red arrows indicate the direction of particle motion. (b) Incident and refracted angles.

The ratio of the length of the plate to the flexural wavelength is

$$\frac{L}{\lambda_F} = \frac{1}{2\pi}\left(\frac{E}{12\rho(1-\nu^2)\omega^2}\right)^{-\frac{1}{4}}\frac{L}{\sqrt{h}}. \tag{6.18}$$

Equation (6.18) and $t_F = L/c_F$ imply that the flexural waves travel through plates of the same $L/\sqrt{h}$ in the same amount of time, and reach the other end with the same phase. Note that total transmission for an incident SV-wave occurs at $\omega = \omega_n$. Using $t_F = L/c_F$ and Eq. (6.18), we have $t_F = n\pi/\omega_n$ and $L/\lambda_F = n/2$, where $n = 1, 2, 3\cdots$. With these properties, we can select desired plate members for the solid structure, as shown in Fig. 6.12a, and achieve zero-refractive index for SV-wave, i.e. $n_{SV} = 0$. As shown in Fig. 6.13a, this zero-refractive effect is independent of frequency since diffraction occurs simultaneously at the right ends of all the plates and forms a new wavefront which is parallel to the inclined edge of plate array, therefore the new SV-wave will propagate in the direction perpendicular to the edge. Notably, a normally incident SV-wave from the left side transmits to the right side keeping its original type, the transmitted P-wave is weak because the coupling mainly comes from the mode in the waveguide/plate. However, in the case of P-wave incidence, the physics of the longitudinal wave on the plate is different since the phase speed does not depend on the thickness of the plate. We consider the plate array as an effective medium in which the longitudinal wave speed in the lateral direction is constant, so that we have the refractive index $n_P = c_P/c_L = (1-\nu)/\sqrt{1-2\nu}$, which only depends on the Poisson's ratio of the material. The refraction of P-wave can also be understood in terms of Huygens'

principle as shown in Fig. 6.13b. In summary, the refractive index for SV- and P-waves are

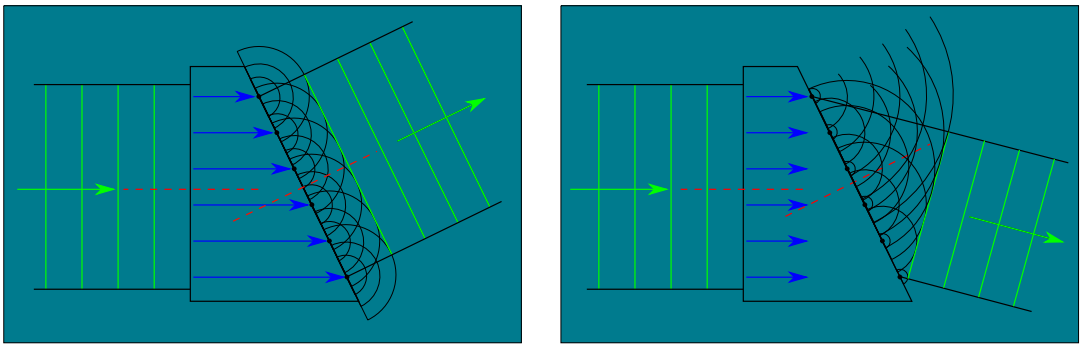

(a) (b)

Figure 6.13: Diffraction and refraction of (a) SV- and (b) P-waves.

$$n_{SV} = \frac{\sin\theta_r}{\sin\theta_i} = 0, \tag{6.19}$$

$$n_P = \frac{\sin\theta_r}{\sin\theta_i} = \frac{1-\nu}{\sqrt{1-2\nu}}, \tag{6.20}$$

respectively.

The refractive device for SV- and P-waves is designed by choosing the thickness h_1 and length L_1 for the plate on the top, the thickness and length of the next plate can be calculated using the relations

$$h_i = \zeta L_i^2, \quad L_{i+1} = L_i - \frac{a+h_i}{s}, \tag{6.21}$$

where the fixed value ζ is chosen for a particular slope, L_i is the length of the plate, and L_{i+1} is the length of the next plate based on the chosen slope s.

We can also design negative-index metamaterial, i.e. $n_{SV} < 0$, by varying the flexural wave travel time in the plates. If the thickness of the plates are the same and we use a similar structure as Fig. 6.12a, then the refractive index is

$$n'_{SV} = \left(\frac{2E(1-\nu)}{\rho(1+\nu)h^2\omega^2}\right)^{\frac{1}{4}}, \tag{6.22}$$

which varies with frequency.

6.4.2 Simulation of the steering effect

Using aluminum as the material, we choose the first plate with the dimensions $h_1 = 0.005$ m, $L_1 = 0.1$ m, and gap width $a = 0.001$ m. We also choose the parameters $s = -3$ and

$\zeta = 0.5$, then the length and thickness of other plates are calculated using Eq. (6.21). In this example, we take the same modification term β for each plate for convenience, the optimal results are obtained when $\beta = 0.15$. Figure 6.14 shows that SV-wave is steered into the direction along the normal of the edge of plate array, i.e. $n_{SV} = 0$. Figure 6.15

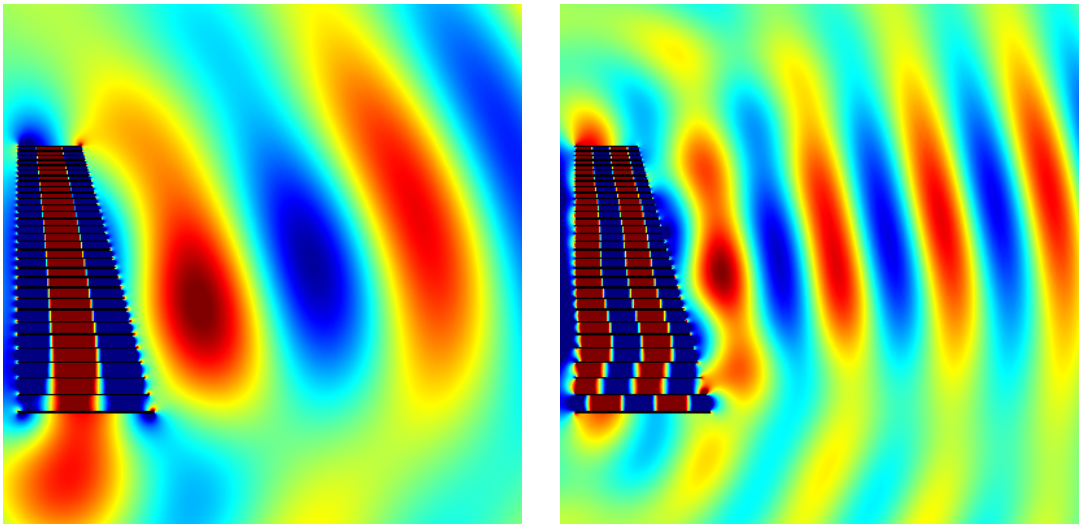

(a) (b)

Figure 6.14: Zero SV-wave refraction at (a) 10 kHz and (b) 20 kHz.

shows the positive refraction of P-wave. In the case of P-wave incidence, β does not play a role but we keep using the same value for better comparison. The simulation results clearly show that the angles of transmitted waves are independent of frequency, because the plate array is designed so that the refractive index for both flexural wave and longitudinal wave are independent of frequency.

6.5 Discussion

We have considered a novel configuration in solids made by parallel gaps that produce arrays of aligned "effective plates". The transmission and reflection coefficients for normally incident SV- and P-waves are calculated using thin plate theory. The GRIN lens is designed by varying the thickness of the plates and demonstrated by full FEM simulations. The refractive device for SV- and P-waves is designed by fixing the ratio between L and $\sqrt{h}$ and choosing the slope of the edge of the plate array. The one-way effect for P-wave is sensitive

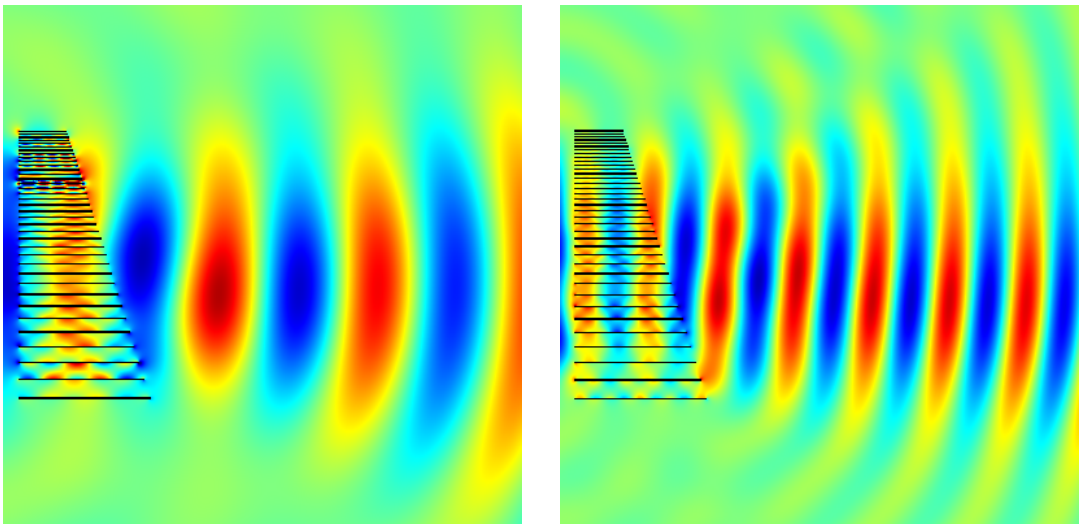

(a) (b)

Figure 6.15: Positive P-wave refraction at (a) 20 kHz and (b) 40 kHz.

to frequency and is, therefore, a multi-band effect. The applications of the aligned parallel plates include but not limited to the designs in this chapter. For example, the plates can be tuned to achieve phase change from 0 to 2π and applied in the metasurface design to guide SV-wave as we discuss in the next chapter.

Chapter 7

Anomalous refraction and asymmetric transmission of SV-wave through elastic metasurfaces

In 2011, Yu *et al.* [117] proposed to engineer the phase discontinuities along the interface according a Generalized Snell's law to redirect light:

$$\frac{\sin\theta_t}{\lambda_t} - \frac{\sin\theta_i}{\lambda_i} = \frac{1}{2\pi}\frac{d\phi}{dy}, \tag{7.1}$$

where the subscripts i and t denote the incident and transmitted waves, respectively. Equation (7.1) implies that the transmitted angle can be designed at will by choosing a proper phase gradient $d\phi/dy$. This idea has been introduced to acoustic metamaterial design to mapnipulate sound fields with sub-wavelength slabs, i.e. metasurfaces. A common method in the design is to use space coiling structures to achieve certain impedance mismatch so that the transmitted phases through each unit cell are different [68, 66, 78, 79, 67]. Many applications are proposed in order to control acoustic waves in an almost arbitrary way. For instance, Xie *et al.* [66] demonstrated anomalous refraction using an acoustic metasurface comprised of labyrinthine unit cells. In addition, they designed a metasurface that turns propagating waves to surface waves. Shen *et al.* [118] used a combination of an gradient index metasurface and a near-zero index metasurface to achieve asymmetric acoustic transmission. However, the metasurface design for elastic waves is still relatively unexplored. The main reason is that mode conversion usually exists at material interface, therefore the phase modulation of a specific wave type is hard to achieve. Recently, Zhu *et al.* [119] demonstrated several metasurfaces for controlling S_0 and A_0 modes on elastic plates by tuning the local resonances of the embedded "acoustic black holes".

The main objective of this chapter is to design sub-wavelength metamaterial slabs to control the propagation direction of SV-wave in bulk solids. The metasurface design usually relies on the phase modulation using local resonances of the unit cell which suffers from

low transmission. Distinguished from the conventional method, the design approach in this chapter do not involve resonant effects. The required phase gradient is engineered by varying plate thickness to tune the phase speed so that a wide range of phase delay can be achieved. The design method requires accurate phase modulation in each unit cell, thus it is essential to establish a more sophisticated model which better matches the phase speed in the unit cells. A metasurface slab is designed according to Eq. (7.1) to split SV- and P-waves into different directions. When paired with another uniform metasurface which has a lower effective speed, spatial asymmetric transmission through the metasurfaces can be achieved.

This chapter is organized as follows. In Sec. 7.1, we review the dispersion relation for the Mindlin plate, and derive the transverse wave speed on the plate as a function of thickness for phase modulation. The metasurface for splitting SV- and P-waves is presented in Sec. 7.2. Section 7.3 illustrates the asymmetric transmission effect through a pair of metasurfaces. Section 7.4 concludes this chapter.

7.1 Phase modulation by thickness variation of plates

7.1.1 Dispersion relation

The unit structure considered in this chapter is the same as the one considered in Chapter 6. The coordinate system and the plate parameters are shown in Fig. 6.1, but the governing equations on the plates are different. The precise phase modulation of transverse wave requires more advanced model to describe the wave propagation on elastic plates. Here we use the well known Mindlin plate theory which takes the shear correction and rotary inertia into account. Neglecting the $y-$dependent terms, the governing equations for transverse waves reduce to

$$\begin{aligned} \kappa\mu\frac{\partial}{\partial x}\Big(\frac{\partial w}{\partial x}-\varphi\Big) &= \rho\frac{\partial^2 w}{\partial t^2}, \\ EI\frac{\partial^2\varphi}{\partial x^2}+\kappa\mu h\Big(\frac{\partial w}{\partial x}-\varphi\Big) &= \rho I\frac{\partial^2\varphi}{\partial t^2}, \end{aligned} \tag{7.2}$$

where κ and φ are the shear correction coefficient and the cross section rotation angle, respectively. These equations are similar to the Timoshenko beam model with cross section area A changed to plate thickness h [120, p. 183]. The shear correction coefficient for

Mindlin plate is usually taken as $\kappa = \pi^2/12$ [116, p. 257].

Now we consider 1D free propagation of time harmonic waves in the infinite plate. The solutions have the general form

$$w = A_1 e^{i(kx-\omega t)}, \quad \varphi = A_2 e^{i(kx-\omega t)}, \tag{7.3}$$

where k is the wavenumber and ω is the circular frequency. Substituting the solutions into Eq. (7.2), we have

$$\begin{pmatrix} \mu h\kappa k^2 - \rho h\omega^2 & i\mu h\kappa k \\ i\mu h\kappa k & -(\mu h\kappa + EIk^2 - \rho I\omega^2) \end{pmatrix} \begin{pmatrix} A_1 \\ A_2 \end{pmatrix} = \begin{pmatrix} 0 \\ 0 \end{pmatrix}. \tag{7.4}$$

The non-trivial solutions require

$$\det \begin{bmatrix} \mu h\kappa k^2 - \rho h\omega^2 & i\mu h\kappa k \\ i\mu h\kappa k & -(\mu h\kappa + EIk^2 - \rho I\omega^2) \end{bmatrix} = 0, \tag{7.5}$$

which yields the dispersion relation

$$\frac{EI}{\rho h}k^4 - \frac{I}{h}\Big(1 + \frac{E}{\mu\kappa}\Big)c^2k^4 - c^2k^2 + \frac{\rho I}{\mu h\kappa}c^4k^4 = 0. \tag{7.6}$$

7.1.2 Phase modulation

Using the identity $\omega = ck$ in Eq. (7.6), the frequency dependent phase speed can be written as

$$c^2 = \frac{\rho I\omega^2\big(E + \mu\kappa\big) \pm \sqrt{\Big(\rho I\omega^2\big(E + \mu\kappa\big)\Big)^2 - 4\Big(\rho^2 I^2 E\mu\kappa\omega^4 - \rho hEI\mu^2\kappa^2\omega^2\Big)}}{2\big(\rho^2 I\omega^2 - \rho h\mu\kappa\big)}, \tag{7.7}$$

where "$\pm$" in the nominator correspond to the phase speeds of traveling and evanescent waves. In the case considered in the following, "$-$" corresponds to the traveling wave while "$+$" corresponds to the evanescent wave. Our objective is to design an array of aligned parallel plates connected to two half-spaces on both ends similar to Fig. 6.1a, the main difference is that the plate thicknesses are not identical. The material of the plates and the half-spaces are aluminum with Young's modulus $E = 70$ GPa, Poisson ratio $\nu = 0.33$ and density $\rho = 2700$ kg/m^3. The plates have uniform length $L = 5$ cm with thickness h varying from 0.2 cm to 1 cm. The plates are equally spacing with gap width $g = 0.5$

mm. Our goal here is to tune the phase delay following Eq. (7.1) to cover a phase change of 2π at 60 kHz, where the wavelength of the SV-wave in the half-space is $\lambda_{SV} = 5.2$ cm ($> L$). The Timoshenko/Mindlin model adopted here is more accurate than the Kirchhoff plate model (c_F in Eq. (6.2)) for thick plates and at high frequency range, this can be easily compared by considering a plate of thickness $h = 1$ cm. The relations between the phase speed and frequency are plotted in Fig. 7.1. Comparing to the FEM results, it is

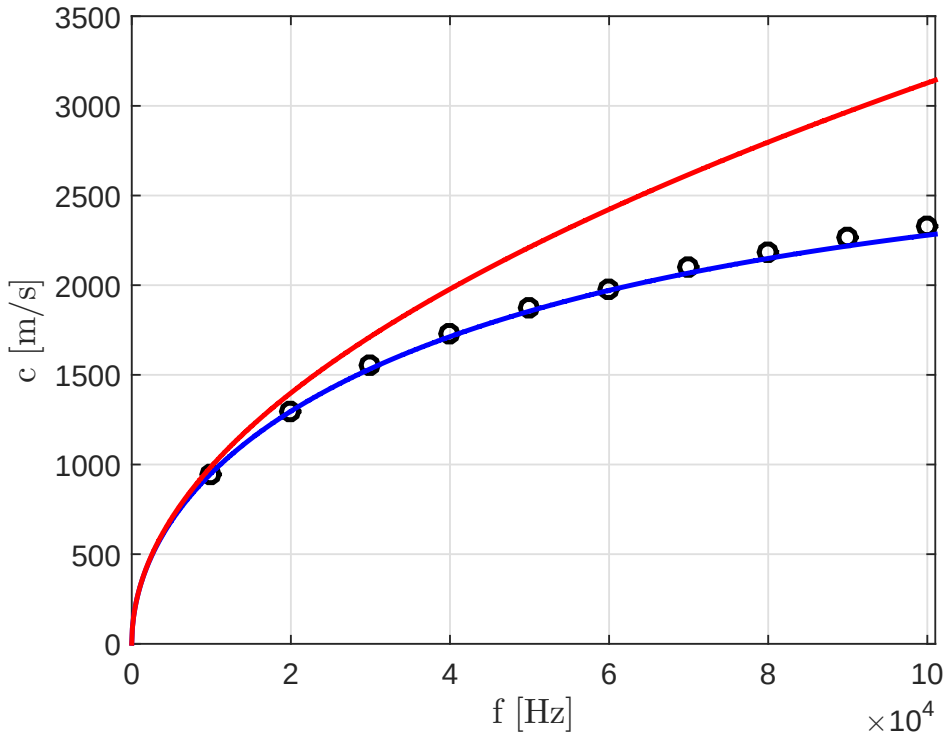

Figure 7.1: Relations between the phase speed and frequency for a 1 cm thick plate. The red curve is calculated using Kirchhoff model, the blue curve is calculated using Timoshenko/Mindlin model, and the black circles are extracted from FEM simulations.

clear that the Timoshenko/Mindlin plate model approximate the speeds very well at all frequency range. The purpose of this chapter is to design metasurface slabs that work at specific frequency, which requires several plates of different thickness. Therefore, it is important that the model is capable of predicting phase speeds accurately for thick plates. Consider transverse wave propagation on plate with different thicknesses from 0.1 cm to 1 cm at 60 kHz, the relations between the speed and the plate thickness are shown in Fig. 7.2. It is obvious that the FEM simulation results agree with the theoretical prediction to

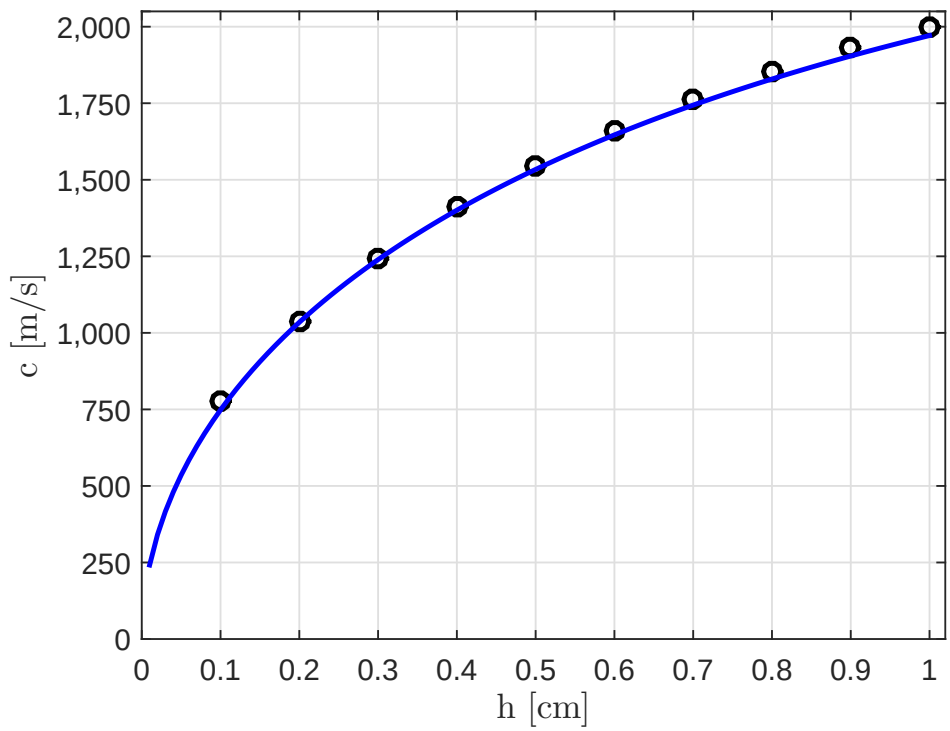

Figure 7.2: Relations between the phase speed and thickness of the plate at 60 kHz. The blue curve is calculated using Timoshenko/Mindlin model, and the black circles are extracted from FEM simulations.

a remarkable degree for thick plates.

Note that a full model to calculate the transmission and reflection coefficients is necessary in order to tune the phase change accurately, this work remains to be done in the future. Here we only consider the transmitted wave in the phase modulation process. According to Eq. (7.1), it is essential to achieve a complete phase delay of 2π in order to design a infinite metasurface slab for anomalous refraction. The phase change through each plate is

$$\Delta\phi = \omega t = \frac{2\pi f L}{c}, \tag{7.8}$$

where c depends on the thickness of the plate. For plate thickness from 0.2 cm to 0.8 cm, we can cover a phase change of 2.6π which is more than sufficient to our metasurface designs.

7.2 Split SV- and P-waves using an elastic metasurface

The anomalous refraction effect by a metasurface is illustrated in Fig. 7.3. The metasurface

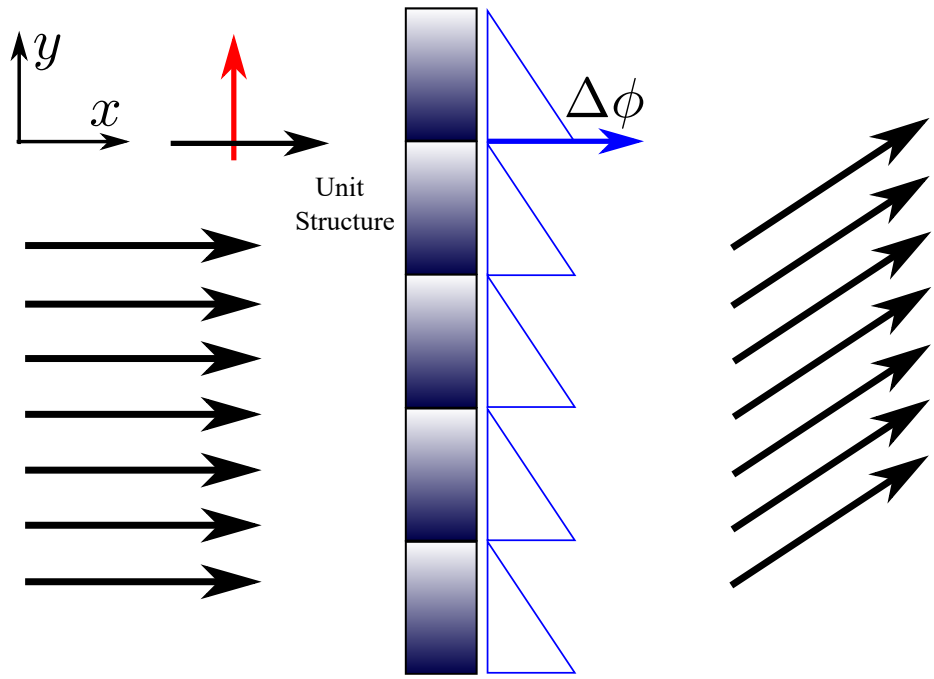

Figure 7.3: Anomalous refraction by a metasurface comprised of several unit structures. The black arrows indicate the propagation direction of the wave, the red arrow indicate the direction of particle motion. The blue lines show the phase gradient in each unit structure.

is designed according to the Generalized Snell's law, Eq. (7.1), with a constant phase gradient $d\phi/dy = 40\pi/\sqrt{3}$ rad/m, which results in a refracted angle $\theta_r = 30°$ for a metasurface of width $L = 5$ cm. The plates have equal length 5 cm and thickness varying from 2.471 mm to 6.836 mm. The plates are equally separated from each other by 0.5 mm-wide cracks. The plates are designed to perfectly match the linear phase gradient at 60 kHz, where $\lambda_{SV} = 5.2$ cm$> L$. The unit structure covering the whole 2π phase change is comprised of a total number of 19 plates, and the metasurface slab is composed of infinite number of the unit structures. With this metasurface, we can easily split SV- and P-waves in elastic solids. The underlying physics here is that the longitudinal wave speed is independent of the plate thickness such that they propagate straight through the metasurface. Full wave FEM simulation results are shown in Fig. 7.4. It is clear that the transmitted SV- and P-waves propagate into different directions indicated by the black arrows. It is notable that the mode conversion induced the by the metasurface is weak, so that the transmitted wave keeps the same type as the incident wave. The refracted angle of the transmitted wave matches well the design to a remarkable degree.

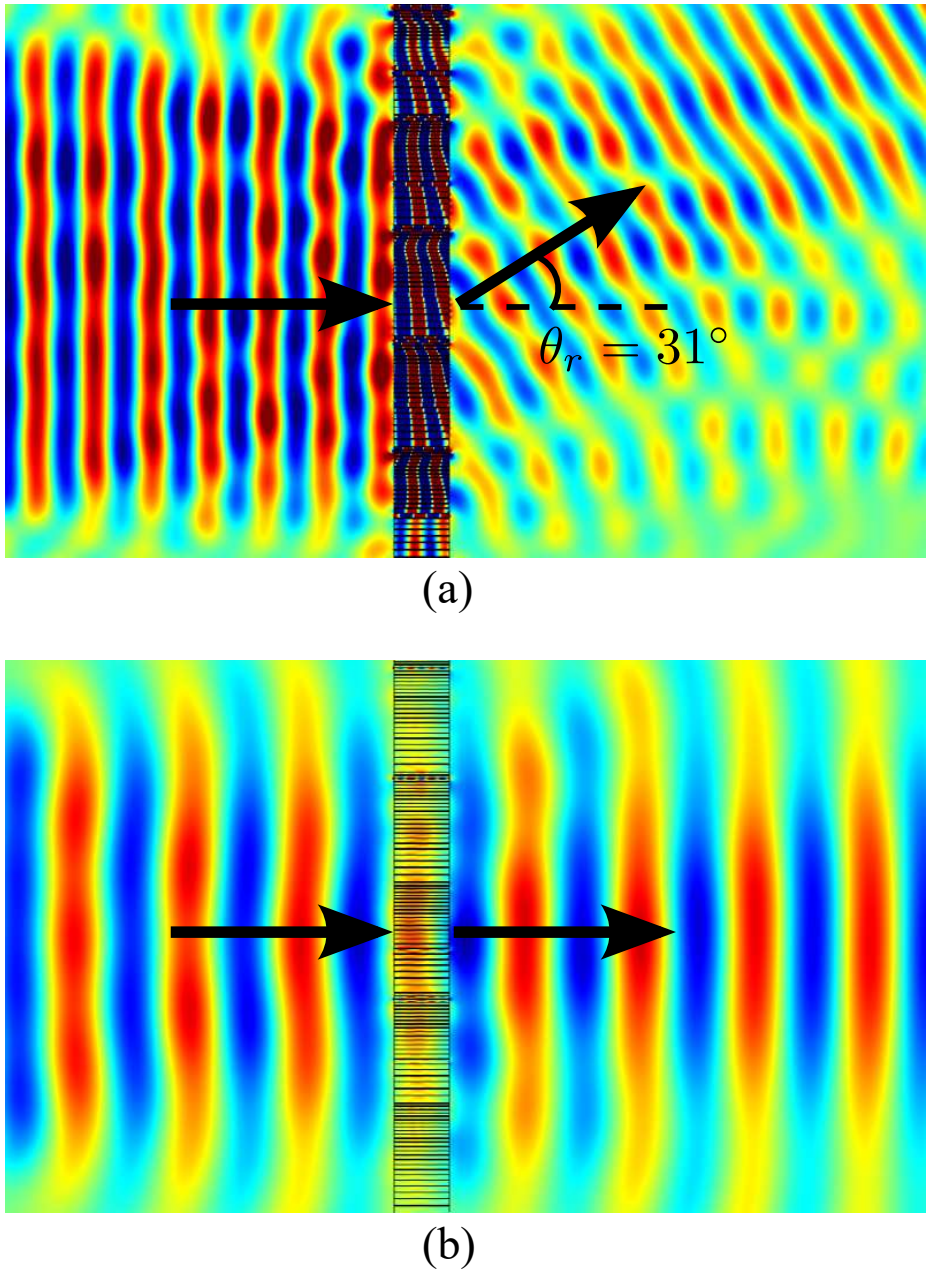

Figure 7.4: SV- and P-wave splitting at 60 kHz. (a) shows the curl of the displacements to represent SV-waves, (b) shows the trace of the strain to represent P-waves. The black arrows indicated the propagation direction of the waves.

7.3 Asymmetric transmission of SV-wave through elastic metasurfaces

The asymmetric transmission device designed in this section is different from the one designed in Sec. 6.2 where the mode conversion at free boundary is the key. Here the asymmetric transmission is achieved by paring the gradient index metasurface with a uniform slow medium. The main underlying physics is the total internal reflection at the uniform metasurface for the refracted wave through the gradient index metasurface. It is known that the critical angle for total internal reflection at material interface is

$$\theta_c = \theta_i = \arcsin\left(\frac{n_2}{n}\right), \tag{7.9}$$

where n is the refractive index of the background medium, and n_2 is the effective refractive index of the uniform slab. According to Eq. (7.9), total reflection occurs when the incident angle, i.e. the refracted angle through the gradient metasurface θ_r, is greater than the critical angle θ_c. We now take advantage of this effect to design the asymmetric transmission device as depicted in Fig. 7.5. When the wave is normally incident from the left side, the gradient metasurface changes the propagation direction of the transmitted wave so that the refracted angle is greater than the critical angle for the uniform metasurface. Then total internal reflection occurs on the interface between the background medium and the uniform slow medium. In this way, the waves cannot travel through the device. However, if the wave is normally incident from the right side, nearly half of the energy carried by the waves pass through the uniform and the gradient metasurfaces.

The asymmetric transmission device is designed by paring the metasurface designed in Sec. 7.2 with a uniform slab. The uniform slab is comprised of equally spacing plates with the same thickness and length. The length of the plate, i.e. the width of slab, is $L = 5$ cm. The constant gap width is 0.5 mm. The thickness of each plate is chosen as 5 mm so that 60 kHz is not a resonant frequency. It is easy to calculate the effective transverse wave speed in the slab using Eq. (7.2), we have $c = 1498.81$ m/s. The wave speed in the background medium is $c_{SV} = \sqrt{\mu/\rho} = 3121.95$ m/s. Using Eq. (7.9), we obtain the critical angle for total internal reflection $\theta_c = 28.69°$, which is smaller than the refracted angle $\theta_r = 31°$ through the gradient metasurface. Full wave FEM simulations were done using COMSOL Multiphysics to demonstrated the asymmetric transmission effect. The results

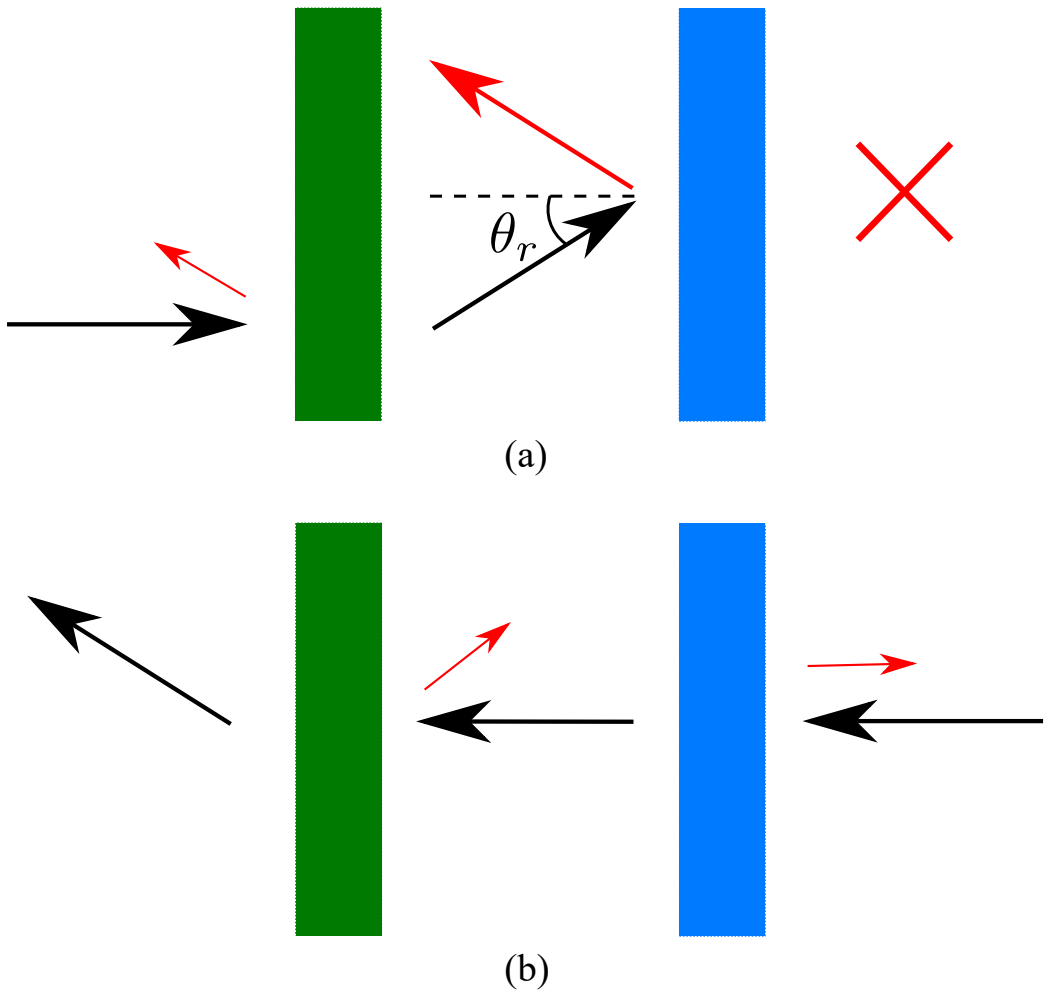

Figure 7.5: Asymmetric elastic transmission through metasurfaces. The green slab is a gradient metasurface for anomalous refraction, the blue slab is a uniform metasurface has lower effective speed. The black and red arrows idicate the propagation direction where the wave is incident from the left side in (a) and is incident from the right side in (b).

are shown in Fig. 7.6. It is easy to see that the transmission is almost zero when the wave is incident from the left side, while a considerable amount of energy transmit through the metasurfaces when the wave is incident from the right side.

7.4 Discussion

To summarize, we have considered the Timoshenko/Mindlin theory to improve our model developed in Chapter 6. The improved phase speed calculation enables us to tune the phase of the transmitted transverse wave through plates, which makes it possible to design metasurfaces by phase modulation. A metasurface slab is designed following Eq. (7.1) with a

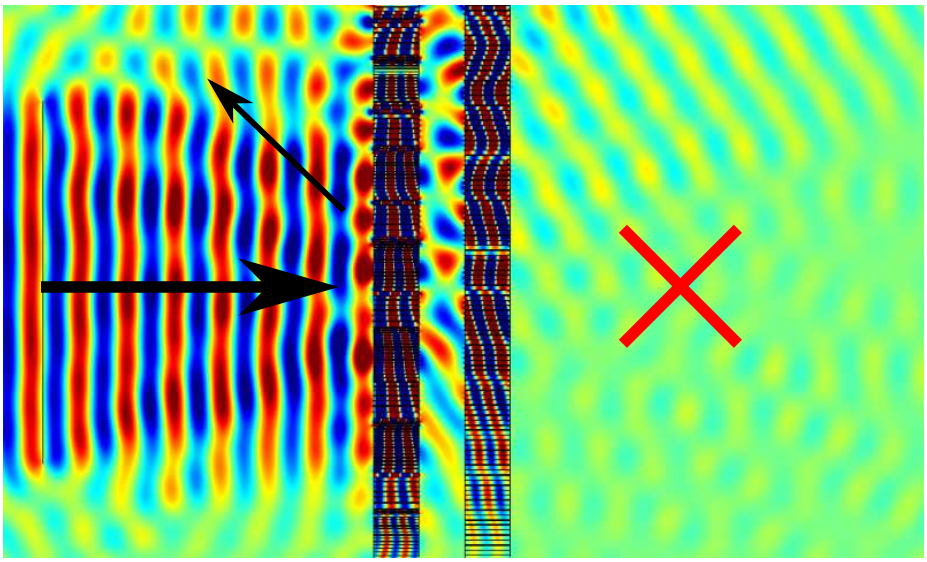

(a)

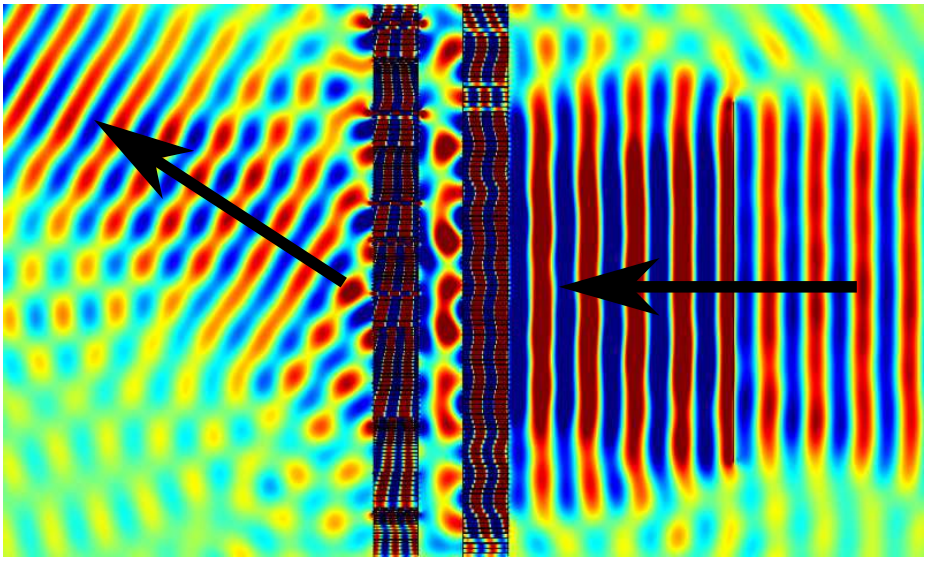

(b)

Figure 7.6: Asymmetric transmission for normally incident SV-waves (a) from the left side, (b) from the right side. The black arrows indicate the propagation direction.

constant phase gradient $d\phi/dy$ to split SV- and P-waves. When paired with a slow medium, the normally incident SV-wave will transmit through the structure from one direction but can not pass through the structure from the other direction. Full wave simulation results are presented to demonstrate the beam splitting and asymmetric transmission effects. The present design method makes it possible to manipulate bulk elastic waves with ultra-thin metamaterial slabs.

Chapter 8

Elastic waves in fluid-saturated cubic double porosity medium

The pioneering work of solid-fluid consolidation theory and elastic wave propagation in fluid-saturated porous solids by Biot [121, 82, 122, 83] inspired much research efforts in this field. Simultaneous existence of fast and slow compressional waves in solid-fluid aggregates is predicted by Biot [82] in 1956. The theory not only has significant applications in petroleum industry but also is important in the material aspects. However, the experimental detection of the slow wave is extremely difficult because it damps out quickly. Plona first observed the slow wave at ultrasonic frequencies [123]. Later on, Johnson *et al.* [124] discovered the relations between the tortuosity and the speed of the slow wave. Many efforts have been paid to generalize the theory to find a second slow wave [125, 126], but the existence of such wave has not been experimentally demonstrated [126].

The porous medium considered in chapter is an anisotropic solid of cubic symmetry with two isolated infinite pores. The pores are separated from each other so that they can be saturated with same or different fluids, thus they need to be treated differently. This study is similar to but different from the cases investigated in Refs. [125, 126]. Berryman *et al.* [125] generalized Biot's theory [82, 83] for application in double-porosity and dual-permeability medium, in which the fluid in the matrix and fracture pores are the same. Beresnev [126] developed a theory to calculate the fast wave speed in a porous medium saturated with two immiscible fluids. Various theories predict a third dilatational wave in fluid-saturated porous solids. Here we propose a solid frame of the gyroid minimal surface type for manipulating a third dilatational wave. We first generalize the theory for low frequency elastic wave propagation in cubic double porosity medium saturated with two distinct fluids, then compare with the wave speeds calculated using FEM simulations. The

results in this chapter may be used to tune the structure to help detect the second slow wave experimentally.

This chapter is structured as follows. We begin with the derivation of equations of motion as well as the wave equations and speeds in Sec. 8.1. In Sec. 8.2, we simplify the equations for isotropic single porosity medium. Examples of fluid-saturated gyroid structures are considered in Sec. 8.3, theoretical results are compared against the FEM simulation results. Section 8.4 concludes this chapter.

8.1 Wave propagation in cubic double porosity media

8.1.1 Constitutive relations of the solid-fluid aggregate

We will use the original notations of Boit [82, 83] as much as possible in the development of the theory. Similar to Beresnev's derivation [126], using notations in Love's book [127, p. 160] the potential energy for the fluids saturated cubic double porosity medium is

$$\begin{aligned} 2V =& P\varepsilon^2 - 2(P-A)(\varepsilon_{xx}\varepsilon_{yy} + \varepsilon_{yy}\varepsilon_{zz} + \varepsilon_{zz}\varepsilon_{xx}) + N(\varepsilon_{xy}^2 + \varepsilon_{yz}^2 + \varepsilon_{zx}^2) \\ &+ 2Q_1\varepsilon\epsilon_1 + 2Q_2\varepsilon\epsilon_2 + R_1\epsilon_1^2 + R_2\epsilon_2^2 + 2R_3\epsilon_1\epsilon_2, \end{aligned} \tag{8.1}$$

where ε_{ij}, ϵ_{1ij} and ϵ_{2ij} are the strain tensors for the solid and two fluids, with

$$\begin{aligned} \varepsilon &= \varepsilon_{xx} + \varepsilon_{yy} + \varepsilon_{zz} = \nabla \cdot \boldsymbol{u}, \\ \epsilon_1 &= \epsilon_{1xx} + \epsilon_{1yy} + \epsilon_{1zz} = \nabla \cdot \boldsymbol{U}_1, \\ \epsilon_2 &= \epsilon_{2xx} + \epsilon_{2yy} + \epsilon_{2zz} = \nabla \cdot \boldsymbol{U}_2, \end{aligned} \tag{8.2}$$

where $\boldsymbol{u}(\boldsymbol{x}, t)$, $\boldsymbol{U}_1(\boldsymbol{x}, t)$ and $\boldsymbol{U}_2(\boldsymbol{x}, t)$ are the displacements in the solid and fluids. Due to the fact that the two fluids are filled in two isolated pores, we assume they do not interact with each other and therefore let $R_3 = 0$. An alternative interpretation is that one fluid interact with the other one through the solid frame, so that the effect of R_3 is already included in Q_1 and Q_2. Following Eq. (8.1) with R_3 terms omitted, the constitutive relations of the aggregate are

$$\begin{aligned} \boldsymbol{\sigma} &= (P-A)\nabla\boldsymbol{u}\boldsymbol{I} + A\nabla\cdot\boldsymbol{u}\boldsymbol{I} + N[\nabla\boldsymbol{u} + (\nabla\boldsymbol{u})^T] + Q_1\nabla\cdot\boldsymbol{U}_1\boldsymbol{I} + Q_2\nabla\cdot\boldsymbol{U}_2\boldsymbol{I}, \\ s_1 &= Q_1\nabla\cdot\boldsymbol{u} + R_1\nabla\cdot\boldsymbol{U}_1, \\ s_2 &= Q_2\nabla\cdot\boldsymbol{u} + R_2\nabla\cdot\boldsymbol{U}_2, \end{aligned} \tag{8.3}$$

where $\boldsymbol{\sigma}$ represents the stress tensor of the solid; s is a scalar proportional to the fluid pressure; and $\boldsymbol{I}$ is a three by three identity matrix. The constants P, A, N, Q_1, Q_2, R_1 and R_2 are unknown. Note that $P = A + 2N$ is only valid for the isotropic case.

8.1.2 Dynamic equations of the solid-fluid aggregate

Taking one additional fluid into account, the kinetic energy of the solid-fluid aggregate is written as [125]

$$\begin{aligned} 2T =& \rho_{11}\frac{\partial^2 \boldsymbol{u}}{\partial t^2} + \rho_{22}\frac{\partial^2 \boldsymbol{U}_1}{\partial t^2} + \rho_{33}\frac{\partial^2 \boldsymbol{U}_2}{\partial t^2} \\ &+ 2\rho_{12}\frac{\partial \boldsymbol{u}}{\partial t}\cdot\frac{\partial \boldsymbol{U}_1}{\partial t} + 2\rho_{13}\frac{\partial \boldsymbol{u}}{\partial t}\cdot\frac{\partial \boldsymbol{U}_2}{\partial t} + 2\rho_{23}\frac{\partial \boldsymbol{U}_1}{\partial t}\cdot\frac{\partial \boldsymbol{U}_2}{\partial t}, \end{aligned} \tag{8.4}$$

where ρ_{ij} are densities related to the inertia of solid and fluid phases. Then the equilibrium equations can be derived using Lagrange's equations. In the absence of dissipation, the equations of motion are

$$\begin{aligned} \rho_{11}\frac{\partial^2 \boldsymbol{u}}{\partial t^2} + \rho_{12}\frac{\partial^2 \boldsymbol{U}_1}{\partial t^2} + \rho_{13}\frac{\partial^2 \boldsymbol{U}_2}{\partial t^2} &= \nabla\cdot\boldsymbol{\sigma}, \\ \rho_{12}\frac{\partial^2 \boldsymbol{u}}{\partial t^2} + \rho_{22}\frac{\partial^2 \boldsymbol{U}_1}{\partial t^2} + \rho_{22}\frac{\partial^2 \boldsymbol{U}_2}{\partial t^2} &= \nabla s_1, \\ \rho_{13}\frac{\partial^2 \boldsymbol{u}}{\partial t^2} + \rho_{23}\frac{\partial^2 \boldsymbol{U}_1}{\partial t^2} + \rho_{33}\frac{\partial^2 \boldsymbol{U}_2}{\partial t^2} &= \nabla s_2. \end{aligned} \tag{8.5}$$

The densities are derived by considering three cases [82, 125]: (1) $\partial\boldsymbol{u}/\partial t = \partial\boldsymbol{U}_1/\partial t$, (2) $\partial\boldsymbol{u}/\partial t = \partial\boldsymbol{U}_2/\partial t$ and (3) $\partial\boldsymbol{U}_1/\partial t = \partial\boldsymbol{U}_2/\partial t$ under the assumption that the mass coupling between different fluids are weak and therefore neglected. Then the six unknown densities are expressed as

$$\begin{aligned} \rho_{11} &= (1-\phi)\rho_s + \gamma\phi\rho_{f1}(\tau_1 - 1) + (1-\gamma)\phi\rho_{f2}(\tau_2 - 1), \\ \rho_{22} &= \gamma\phi\rho_{f1}\tau_1, \\ \rho_{33} &= (1-\gamma)\phi\rho_{f2}\tau_2, \\ \rho_{12} &= -\gamma\phi\rho_{f1}(\tau_1 - 1), \\ \rho_{13} &= -(1-\gamma)\phi\rho_{f2}(\tau_2 - 1), \\ \rho_{23} &= 0, \end{aligned} \tag{8.6}$$

where ρ_s is the density of the solid material, ρ_{f1} and ρ_{f2} are the densities of the two fluids, τ_1 and τ_2 are tortuosities of the two pores, ϕ is the overall porosity of the solid,

and γ is the pore volume fraction occupied by the pore denoted by subscript 1. The term $\rho_{23} = 0$ indicate that there is no mass coupling between two fluids. As a check of the total mass, we may consider the limiting case $\partial \boldsymbol{u}/\partial t = \partial \boldsymbol{U}_1/\partial t = \partial \boldsymbol{U}_2/\partial t$. This leads to $\rho_{11} + \rho_{22} + \rho_{33} + 2\rho_{12} + 2\rho_{13} + 2\rho_{23} = (1-\phi)\rho_s + \gamma\phi\rho_{f1} + (1-\gamma)\phi\rho_{f2}$.

8.1.3 Wave equations and speeds

The wave equations along three principal axises, i.e. (100), (010) and (001), are derived by inserting Eq. (8.3) into the equilibrium Eq. (8.5), we have

$$\begin{aligned}
(P - A - 2N)\nabla\nabla \boldsymbol{u}\boldsymbol{I} + N\nabla^2\boldsymbol{u} + \nabla\nabla\cdot[(A+N)\boldsymbol{u} + Q_1\boldsymbol{U}_1 + Q_2\boldsymbol{U}_2] \\
= \frac{\partial^2}{\partial t^2}(\rho_{11}\boldsymbol{u} + \rho_{12}\boldsymbol{U}_1 + \rho_{13}\boldsymbol{U}_2), \\
\nabla\nabla\cdot(Q_1\boldsymbol{u} + R_1\boldsymbol{U}_1) = \frac{\partial^2}{\partial t^2}(\rho_{12}\boldsymbol{u} + \rho_{22}\boldsymbol{U}_1), \\
\nabla\nabla\cdot(Q_2\boldsymbol{u} + R_2\boldsymbol{U}_2) = \frac{\partial^2}{\partial t^2}(\rho_{13}\boldsymbol{u} + \rho_{33}\boldsymbol{U}_2).
\end{aligned} \tag{8.7}$$

These are the governing equations of the wave propagation in the fluid-saturated porous solid. The displacement fields $\boldsymbol{u}$, $\boldsymbol{U}_1$ and $\boldsymbol{U}_2$ can be decomposed into dilatational and rotational terms as

$$\begin{aligned}
\nabla\cdot\boldsymbol{u} &= \varepsilon, & \nabla\times\boldsymbol{u} &= \omega, \\
\nabla\cdot\boldsymbol{U}_1 &= \epsilon_1, & \nabla\times\boldsymbol{U}_1 &= \Omega_1, \\
\nabla\cdot\boldsymbol{U}_2 &= \epsilon_2, & \nabla\times\boldsymbol{U}_2 &= \Omega_2.
\end{aligned} \tag{8.8}$$

Along similar lines of the development of the compressional and shear wave equations by Biot [82], we apply curl operations to Eq. (8.7) and obtain the following equations

$$\begin{aligned}
\frac{\partial^2}{\partial t^2}(\rho_{11}\omega + \rho_{12}\Omega_1 + \rho_{13}\Omega_2) = N\nabla^2\omega, \\
\frac{\partial^2}{\partial t^2}(\rho_{12}\omega + \rho_{22}\Omega_1) = 0, \\
\frac{\partial^2}{\partial t^2}(\rho_{13}\omega + \rho_{33}\Omega_2) = 0.
\end{aligned} \tag{8.9}$$

These equations can be combined into one equation by eliminating Ω_1 and Ω_2, we have

$$\rho_{11}\left(1 - \frac{\rho_{12}^2}{\rho_{11}\rho_{22}} - \frac{\rho_{13}^2}{\rho_{11}\rho_{33}}\right)\frac{\partial^2\omega}{\partial t^2} = N\nabla^2\omega. \tag{8.10}$$

It is straightforward that there is only one rotational speed in the fluid-saturated double porosity solid. The shear wave velocity is

$$v_s = \sqrt{\frac{N}{\rho_{11}\left(1 - \frac{\rho_{12}^2}{\rho_{11}\rho_{22}} - \frac{\rho_{13}^2}{\rho_{11}\rho_{33}}\right)}}. \tag{8.11}$$

We now apply divergence operations to Eq. (8.7) and write the following system of equations

$$\begin{aligned} \nabla^2(P\varepsilon + Q_1\epsilon_1 + Q_2\epsilon_2) &= \frac{\partial^2}{\partial t^2}(\rho_{11}\varepsilon + \rho_{12}\epsilon_1 + \rho_{13}\epsilon_2), \\ \nabla^2(Q_1\varepsilon + R_1\epsilon_1) &= \frac{\partial^2}{\partial t^2}(\rho_{12}\varepsilon + \rho_{22}\epsilon_1), \\ \nabla^2(Q_2\varepsilon + R_2\epsilon_2) &= \frac{\partial^2}{\partial t^2}(\rho_{13}\varepsilon + \rho_{33}\epsilon_2). \end{aligned} \tag{8.12}$$

We first define a reference velocity as

$$v_c = \sqrt{H/\rho}, \tag{8.13}$$

where $H = P + R_1 + R_2 + 2Q_1 + 2Q_2$, and ρ is the total mass of the solid-fluid aggregate per unit volume. Then we introduce the dimensionless parameters

$$\begin{aligned} &\alpha_{11} = \frac{P}{H}, \quad \alpha_{22} = \frac{R_1}{H}, \quad \alpha_{33} = \frac{R_2}{H}, \quad \alpha_{12} = \frac{Q_1}{H}, \quad \alpha_{13} = \frac{Q_2}{H}, \quad \alpha_{23} = 0, \\ &\beta_{11} = \frac{\rho_{11}}{\rho}, \quad \beta_{22} = \frac{\rho_{22}}{\rho}, \quad \beta_{33} = \frac{\rho_{33}}{\rho}, \quad \beta_{12} = \frac{\rho_{12}}{\rho}, \quad \beta_{13} = \frac{\rho_{13}}{\rho}, \quad \beta_{23} = 0. \end{aligned} \tag{8.14}$$

It is easy to write Eq. (8.12) as

$$\begin{pmatrix} \alpha_{11}z - \beta_{11} & \alpha_{12}z - \beta_{12} & \alpha_{13}z - \beta_{13} \\ \alpha_{12}z - \beta_{12} & \alpha_{22}z - \beta_{22} & 0 \\ \alpha_{13}z - \beta_{13} & 0 & \alpha_{33}z - \beta_{33} \end{pmatrix} \begin{pmatrix} C_1 \\ C_2 \\ C_3 \end{pmatrix} = 0, \tag{8.15}$$

where C_1, C_2 and C_3 are amplitudes of the waves in solid and fluids. The dilatational wave speeds are related to the value of z, which is the solution of Eq. (8.15). To have non-trivial solutions, the determinant of the three by three matrix in Eq. (8.15) must equal to zero. In the most general case where the two different pores have different shapes and filled by different fluids, this equation must have three different roots that corresponding to one fast wave and two slow waves:

$$\begin{aligned} v_1 &= v_c/\sqrt{z_1}, \\ v_2 &= v_c/\sqrt{z_2}, \\ v_3 &= v_c/\sqrt{z_3}. \end{aligned} \tag{8.16}$$

The parameters P, Q_1, Q_2, R_1, R_2 and N are unknown, and can be determined by comparing Eq. (8.16) with the effective speeds extracted from FEM simulations.

Equation (8.15) also predicts a third dilatational wave if the pores have different volume fractions or tortuosities even they are filled by the same fluid. However, there is one exceptional case in which the third solution is trivial. If the two pore geometries are identical and filled by the same fluid, the third solution of Eq. (8.15) becomes $z_3 = \beta_{22}/\alpha_{22} = \beta_{33}/\alpha_{33}$ which leads to $(\alpha_{12}z_3 - \beta_{12})C_1 = 0$. The parameters α_{12}, α_{22} and β_{22} are all positive, whereas β_{12} is negative. As a result, this solution yields $C_1 = C_2 = C_3 = 0$ which means the aggregate is at rest.

8.2 Isotropic single porosity

8.2.1 Elastic constants and densities

As discussed in the last section, Eq. (8.15) only has two non-trivial solutions when the two identical pores are filled with the same fluid. This indicates that we can treat this kind of structure as single porosity material and reduce the system to a two by two one. The simplification results in a set of equations the same as the original Biot theory [82]. The fluid-saturated gyroid structure considered in this chapter is weakly anisotropic, therefore we can simply apply the Biot theory in our analysis. Here we summarize the main results and parameters for later use. The elastic constants P, Q and R can be related to porosity ϕ, bulk modulus of the solid material K_s, bulk modulus of the fluid K_f, bulk modulus of the porous "drained" solid frame K_b and the shear modulus N of the dry solid frame via three "Gedanken experiments" [128]. We have the following three equations

$$\begin{aligned}
\frac{1}{K_s} &= \frac{(1-\phi)R - \phi Q}{(P - \frac{4}{3}N)R - Q^2}, \\
\frac{1}{K_f} &= \frac{\phi(P - \frac{4}{3}N) - (1-\phi)Q}{(P - \frac{4}{3}N)R - Q^2}, \\
\frac{1}{K_b} &= \frac{R}{(P - \frac{4}{3}N)R - Q^2},
\end{aligned} \tag{8.17}$$

where K_s and K_f are known; K_b and N are the properties to be measured by the "Gedanken experiments"; P, Q, R are the unknown parameters. Rearranging these equations, the

unknown coefficients P, Q and R can be written as [129]

$$
\begin{aligned}
P &= \frac{(1-\phi)(1-\phi-\frac{K_b}{K_s})K_s + \phi\frac{K_s}{K_f}K_b}{1-\phi-\frac{K_b}{K_s}+\phi\frac{K_s}{K_f}} + \frac{4}{3}N, \\
Q &= \frac{(1-\phi-\frac{K_b}{K_s})\phi K_s}{1-\phi-\frac{K_b}{K_s}+\phi\frac{K_s}{K_f}}, \\
R &= \frac{\phi^2 K_s}{1-\phi-\frac{K_b}{K_s}+\phi\frac{K_s}{K_f}}.
\end{aligned}
\tag{8.18}
$$

The compressional and shear wave speeds (v_P and v_T) of the dry sample can be easily obtained from the dispersion curves calculated using COMSOL Multiphysics. Then we can calculate K_b and N using the following equations

$$
\begin{aligned}
v_P &= \sqrt{\frac{K_b + \frac{4}{3}N}{(1-\phi)\rho_s}}, \\
v_T &= \sqrt{\frac{N}{(1-\phi)\rho_s}}.
\end{aligned}
\tag{8.19}
$$

The densities ρ_{ij} related to the inertia of the solid and fluid phases are

$$
\begin{aligned}
\rho_{11} &= \rho_1 + \rho_a, \\
\rho_{22} &= \rho_2 + \rho_a, \\
\rho_{12} &= -\rho_a,
\end{aligned}
\tag{8.20}
$$

where

$$
\begin{aligned}
\rho_1 &= (1-\phi)\rho_s, \\
\rho_2 &= \phi\rho_f
\end{aligned}
\tag{8.21}
$$

are the mass of solid per unit volume and the mass of fluid per unit volume, respectively. The parameter ρ_a represents the mass coupling between solid and fluid phases and can be written as

$$
\rho_a = \phi\rho_f(\tau - 1), \tag{8.22}
$$

where $\tau > 1$ is the tortuosity coefficient which only depends on the pore geometry [124]. The densities satisfy the following relation

$$
\rho = \rho_{11} + 2\rho_{12} + \rho_{22} = \rho_1 + \rho_2 = \rho_s + \phi(\rho_f - \rho_s), \tag{8.23}
$$

where ρ is the total mass of the solid-fluid composite per unit volume.

8.2.2 Biot wave speeds

There is only one rotational wave speed in fluid-saturated isotropic single porosity solid. The velocity of this wave is

$$v_s = \sqrt{\frac{N}{\rho_{11}(1 - \frac{\rho_{12}^2}{\rho_{11}\rho_{22}})}}. \tag{8.24}$$

There are two dilatational waves in the fluid-solid aggregates. The velocities of these waves are

$$\begin{aligned} v_1 &= v_c/\sqrt{z_1}, \\ v_2 &= v_c/\sqrt{z_2}, \end{aligned} \tag{8.25}$$

where v_c is a reference speed defined as

$$v_c = \sqrt{H/\rho}, \tag{8.26}$$

with

$$H = P + R + 2Q. \tag{8.27}$$

The parameters $z_1 > z_2$ are obtained by solving the following equation

$$(\alpha_{11}\alpha_{22} - \alpha_{12}^2)z^2 - (\alpha_{11}\beta_{22} + \alpha_{22}\beta_{11} - 2\alpha_{12}\beta_{12})z + (\beta_{11}\beta_{22} - \beta_{12}^2) = 0, \tag{8.28}$$

where the parameters α_{ij} and β_{ij} are

$$\begin{aligned} \alpha_{11} &= P/H, \quad \alpha_{22} = R/H, \quad \alpha_{12} = Q/H, \\ \beta_{11} &= \rho_{11}/\rho, \quad \beta_{22} = \rho_{22}/\rho, \quad \beta_{12} = \rho_{12}/\rho. \end{aligned} \tag{8.29}$$

The first dilatational wave v_1 is the fast wave in which the amplitudes of waves are in phase, while the second wave v_2 is the slow wave in which the amplitudes are of the opposite phase.

8.3 Wave speeds in fluid-saturated gyroid structures

8.3.1 Effective properties of the empty gyroid structure

In this section, we compare the theoretical results with FEM simulations. The gyroid structure considered here is a self-assembled minimal surface without self-intersection first introduced by Schoen [130] in 1970. It can be trigonometrically approximated by

$$\sin(x)\cos(y) + \sin(y)\cos(z) + \sin(z)\cos(x) = 0. \tag{8.30}$$

Now we assume the porous solid has the shape of the gyroid minimal surface type but with a certain thickness as shown in Fig. 8.1a. The wall has uniform thickness and separates the

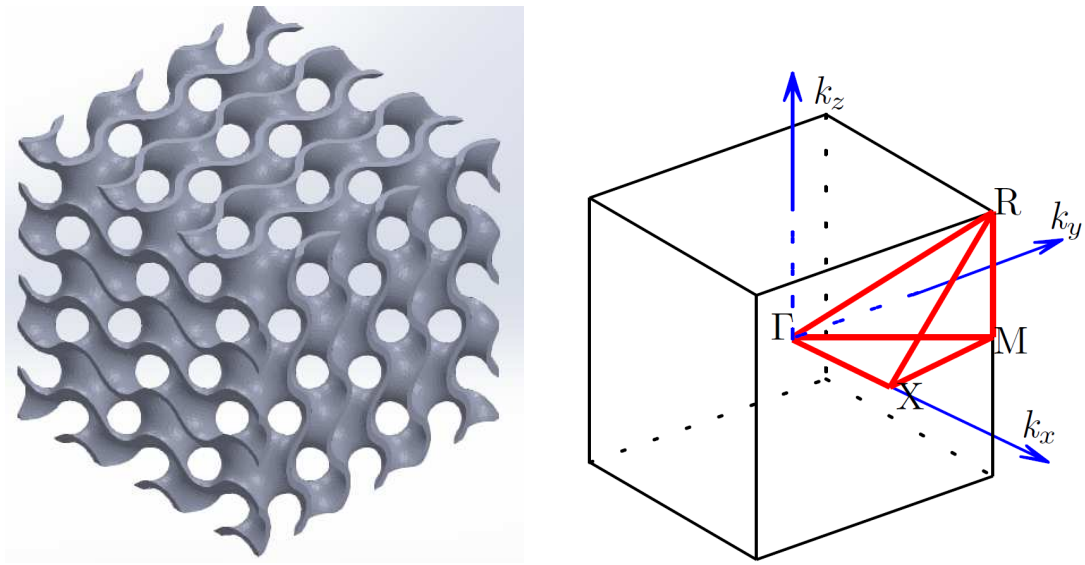

(a) (b)

Figure 8.1: Gyroid structures. (a) A cube comprised of 6×6 unit cells, (b) the Irreducible Brillouin Zone of the structure.

whole space into two identical parts, such that the fluids in the two channels are isolated from each other. This feature provides a easy way to design a porous material with double porosity, and hence introduce a second slow wave by adding two distinct fluids into the pores according to the findings in Sec. 8.2.

The unit cell (cube) of the gyroid structure used in our numerical example has edge length $L = 3.14$ cm and porosity $\phi = 0.668811$. The material of the solid frame is aluminum with Young's modulus $E_s = 70$ GPa, Poisson's ratio $\nu_s = 0.33$ and density $\rho_s = 2700$ kg/m^3. Before calculating the wave speeds in the fluid-saturated gyroid structrue, we shall evaluate the effective properties of the dry structure. The effective density is the average of the mass over volume of the unit cube, we have

$$\rho_{\text{eff}} = \rho_1 = (1 - \phi)\rho_s. \tag{8.31}$$

It is easy to calculate the effective density $\rho_{\text{eff}} = 894.21$ kg/m^3. Then the key to the evaluation of elastic parameters is the calculation of the speeds. From Fig. 8.1a we find that the gyroid structrue has rotational symmetry about the body diagonals by $\pi/3$ and

$2\pi/3$, therefore it has cubic symmetry. The gyroid structure is usually assumed to be isotropic because the anisotropy is weak when the volume fraction is low. This allows us to evaluate the effective elastic constants of the dry sample from the compressional and shear wave speeds using Eq. (8.19).

The wave speeds in the dry structure are calculated using COMSOL Multiphysics. By imposing Bloch-Floquet periodic conditions on the cubic faces, we can compute eigenfrequencies corresponding to each wave vector along the boundary of the IBZ, as shown in Fig. 8.1b, and evaluate the effective wave speeds at low frequency range. The dispersion curves along the $\Gamma - X$ path of the empty gyroid structure considered in this chapter is shown in Fig. 8.2. The two curves starting from $f = 0$ Hz correspond to the shear mode

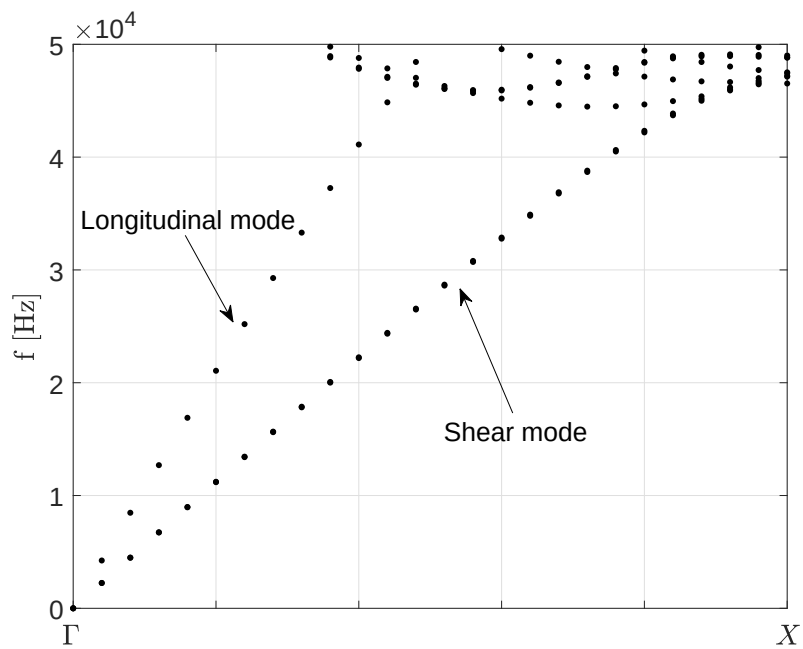

Figure 8.2: Dispersion curves along the $\Gamma - X$ path of the IBZ for the gyroid structure without fluid.

(lower curve) and longitudinal mode (higher curve), respectively. Taking the slop of each dispersion curve, the speeds of the longitudinal and transverse waves are $v_P = 3840$ m/s and $v_T = 2080$ m/s, respectively. Using Eq. (8.19), we have the effective elastic constants $K_b = 8.027$ GPa and $N = 3.869$ GPa.

8.3.2 Wave speeds in gyroid structure filled by single fluid

Now we assume the two pores of the gyroid structure are saturated by the same fluid. The structure separates the internal channel into two isolated ones, we can still treat them as one because the fluids are the same. In this example, the fluid inside the pores is water with bulk modulus $K_f = 2.25$ GPa and density $\rho_f = 1000$ kg/m^3. Using Eq. (8.21), the mass density of solid per unit volume and the mass of fluid per unit volume are $\rho_1 = 894.21$ kg/m^3 and $\rho_2 = 669.99$ kg/m^3, respectively. The total mass per unit volume from Eq. (8.23) is $\rho = 1564.2$ kg/m^3. Note that the total mass of solid per unit volume is the same as the effective density of the empty gyroid unit structure, i.e. $\rho_s = \rho_{\text{eff}}$. For the gyroid structure, the tortuosity has been studied for other purposes by Chen *et al.* [131] where the values for different wall thicknesses are all close to 1.5. Here we directly insert $\tau = 1.5$ into Eq. (8.22), this leads to the mass coupling coefficient $\rho_a = 334.41$ kg/m^3. Plugging ρ_a into Eq. (8.20), we have $\rho_{11} = 1228.62$ kg/m^3, $\rho_{22} = 1003.22$ kg/m^3 and $\rho_{12} = -334.41$ kg/m^3.

The shear modulus N of the dry frame and the density parameters of the composite are already known. Inserting N and densities into Eq. (8.24), we have the rotational wave speed $v_s = 1860.92$ m/s. The band diagram of the fluid-saturated structure is computed using COMSOL by applying Bloch-Floquet periodic conditions on the solid and fluid phases. Although the relative motion between the solid and fluid phase is not incorporated into the FEM model, we can still use it to extract the wave speeds in the structure. The dispersion curves are shown in Fig. 8.3. An additional longitudinal mode appears in the band diagram due to the presence of the fluid (two curves overlap together). From the mode shapes of each mode, we find that the higher longitudinal mode correspond to the fast wave while the lower one correspond to the slow wave. The shear wave speed extracted from the band structure at the *quasi-static* regime is $v_s = 1871.09$ m/s. The result calculated using Biot's theory is only 0.54% lower than the FEM result where full elastodynamic equations were solved numerically. The dilatational wave speeds are related to the elastic constants P, Q and R. These parameters can be achieved using Eq. (8.18) in which $K_s = E_s/3(1-2\nu_s)$ is the bulk modulus of the solid material. We have $P = 13.338$ GPa, $Q = 0.477$ GPa and $R = 1.489$ GPa, respectively. Then the reference velocity defined in Eq. (8.26) is

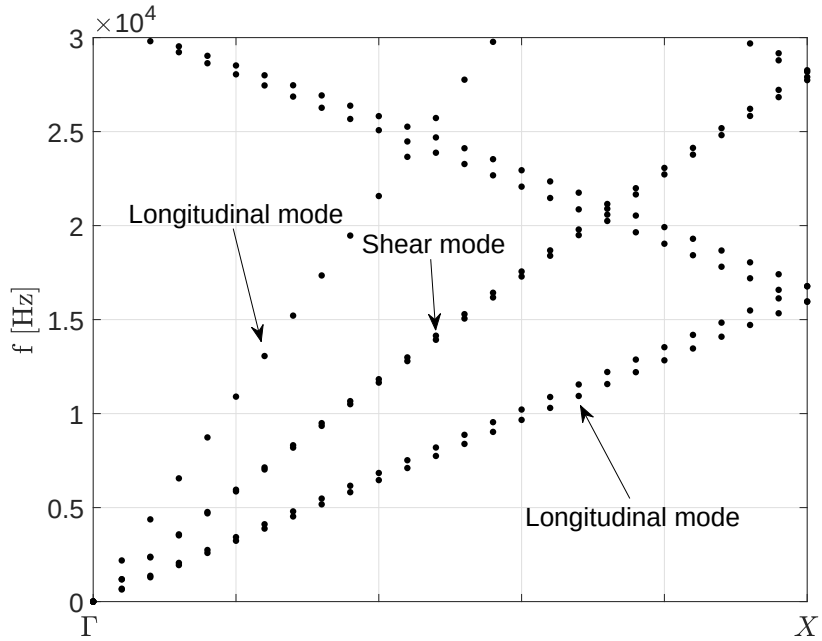

Figure 8.3: Dispersion curves along the $\Gamma - X$ path of the IBZ for the gyroid structure saturated by the same fluid.

$v_c = 3177.55$ m/s. The parameters z_1 and z_2 are calculated by combining Eqs. (8.28) and (8.29) which yields two positive real values, i.e. $z_1 = 0.811$ and $z_2 = 7.175$. Inserting z_1 and z_2 into Eq. (8.25), we obtain the two dilatational wave speeds: $v_1 = 3528.40$ m/s and $v_2 = 1186.30$ m/s. The first one is the fast wave in which the amplitudes of waves are in phase, whereas the second one is the slow wave in which the amplitudes are of the opposite phase. The speeds of the fast and slow dilatational waves calculated using COMSOL are $v_1 = 3452.53$ m/s and $v_2 = 1041.25$ m/s. The results generally agree with the theoretical predictions, the discrepancies might due to the selection of the tortuosity.

8.3.3 Wave speeds in gyroid structure filled by two fluids

It is shown that when the solid frame is saturated by two distinct fluids, a second slow wave exists in the fluid-solid aggregate. In this section, we use the same material for the solid phase and fill one of the two pores with water, while fill the other pore with oil. The densities of the fluid phases are $\rho_{f1} = 1000$ kg/m^3 for water and $\rho_{f2} = 789$ kg/m^3 for oil, respectively. The porosity of the structure is $\phi = 0.668811$ where each of the pore occupies

half of the porosity, i.e. $\gamma = 0.5$. The tortuosity of the two different pores are the same because they have the same shape, we have $\tau_1 = \tau_2 = 1.5$. Using Eq. (8.6), we have the desities $\rho_{11} = 1193.34$ kg/m^3, $\rho_{22} = 501.61$ kg/m^3, $\rho_{33} = 395.77$ kg/m^3, $\rho_{12} = -167.20$ kg/m^3 and $\rho_{13} = -131.92$ kg/m^3.

Plugging the densities and shear modulus N into Eq. (8.11), we have the shear wave speed $v_s = 1880.89$ m/s, which is slightly bigger than the single fluid case. The main reason is that the second fluid has lower density so that the effective density of the aggregate is smaller. The dispersion curves calculated using COMSOL is shown in Fig. 8.4. It clear

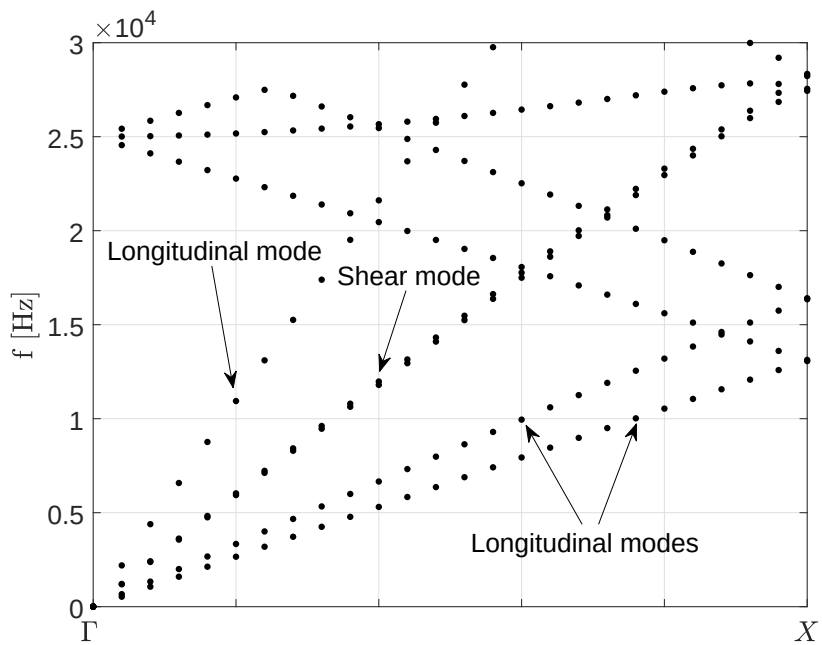

Figure 8.4: Dispersion curves along the $\Gamma - X$ path of the IBZ for the gyroid structure saturated by two distinct fluids.

that the two slow dilatational modes separate from each other due to the difference of the fluid properties. The shear wave speed calculated using COMSOL is $v_s = 1894.62$ m/s. The analytical and FEM results agree very well where the speed calculated using the generalized Biot theory is only 0.72% lower than FEM result. The dilatational wave speeds can also be easily obtained from the band structures, we have $v_1 = 3444.19$ m/s, $v_2 = 1045.80$ m/s and $v_3 = 833.29$ m/s. However, the dilatational wave speeds can not be calculated analytically without the values of P, Q_1, Q_2, R_1 and R_2. We leave this work for the future.

8.4 Discussion

In this section, we generalized the Biot's theory for elastic waves in fluid-saturated solids. It was found that when two identical pores are saturated by different fluids there are two slow longitudinal modes, while when they are filled by the same fluid the slow modes become identical. It was also predicted that when the two pores have different volume fraction or tortuosity, there exist two slow wave modes even if the fluids are the same. Examples showing comparisons between the analytical and numerical results are presented. However, the determination of the elastic constants P, Q_1, Q_2, R_1 and R_2 still needs further investigation. Future work will also include damping in the model, which might be useful in many applications such as underwater sound absorption.

Chapter 9

Concluding remarks

The main objectives of this dissertation are to introduce several types of design elements, and to apply them in metamaterial design. The applications developed in this work aim to achieve full control of the propagation of waves in acoustic medium, solids and fluid-solid aggregates. This chapter concludes the present research and points out the directions of future work.

9.1 Conclusions on the original contributions

The original contributions in this dissertation are covered in Chapters 2 to 8. My research begins with the theoretical derivation of the dispersion relations for 3D elastic lattice structures in Chapter 2. The analytical model embraces all the modes on each beam member, i.e. longitudinal and flexural modes, that lead to the static effective medium. By imposing Bloch-Floquet periodic condition on the boundaries of the unit cell, we derived the equations of motion of the infinite lattice which yield the dispersion relations. The results in this chapter have significant applications in 3D pentamode acoustic metamaterial design as it enables fast computation of band diagrams. To my knowledge, this is the first work seeking analytical dispersion relations using beam theories for 3D elastic lattice networks.

In Chapter 3, we derived the acoustic impedance of slanted gratings and the transmission coefficient. It was found that for slanted gratings oriented with a certain angle, a plane wave incident from the intromission angle $\pm\theta_i$ can propagate through the gratings without reflection. Several frequency domain and time domain examples are discussed in this chapter. The results can be applied in acoustic grating design. Moreover, the analytical results are readily to be used to improve the performance of acoustic Fresnel lenses.

Two metamaterial devices for underwater applications are presented in Chapters 4 and

5. The pentamode GRIN lens reported in Chapter 4 provides a novel approach to reduce aberration and suppress side lobes. The conformal lens designed in Chapter 5 makes it possible to convert cylindrical sources into highly directional plane wave beams. These two metamaterial devices take advantage of the *quasi-static* effective properties of the unit cells so that they are both broadband.

The metamaterial devices for controlling bulk elastic waves are presented in Chapters 6 and 7. The underlying physics are the coupling between the waves in the elastic half-spaces and the waves on the elastic plates. Several novel applications such as beam splitting and focusing are proposed. The main difference between these two chapters is that Chapter 6 uses wide structures while Chapter 7 uses subwavelength slabs. It is notable that unidirectional transmission for SV-wave is achieved in Chapter 7 by breaking the spatial symmetry of the device.

Some new results on the fluid-saturated cubic double porosity medium are covered in Chapter 8. The results derived in this chapter indicate that a second slow wave exists in the fluid-solid aggregate if the two distinct pores have different volume fractions or are filled with different fluids.

9.2 Current and future work

Currently, the structure of the 3D pentamode acoustic metamaterial has been designed. The structural parameters are iterated using Bloch-Floquet analysis in COMSOL Multiphysics to have effective speed and average density equal to water. The undergoing work is to choose a proper thickness of plate to seal the structure so that the overall transmission is high in the frequency range of interest. The structure will then be fabricated using 3D metal printing and be tested in a resonance tube. The objective is to use this type of unit cell to develop 3D metamaterial devices, e.g. GRIN lens.

The design of elastic metasurface still needs a better model to calculate the transmission coefficient to assist with. The transmission and reflection problem will be modeled using Timoshenko/Mindlin theory, and then be applied in the design to tune the phase change more accurately. In the future, we will also investigate the wave radiation from each plate

member. The full problem will be treated as multiple line sources located on a half space, where each line source radiation can be considered as the well known Lamb's problem [132].

The speeds of the fast and two slow waves in fluid-saturated cubic porosity medium are derived Chapter 8 without including the relative motion between the fluid phase and solid phase. However, loss caused by friction between fluid and solid has significant effect on the slow waves so that they damp out quickly. Loss will be incorporated into our model in the future. This research has potential applications in underwater sound absorption.

Appendix A

Coordinate transformation for cubic lattice

There are six beams/rods in a unit cell of cubic lattice as shown in Fig. 2.4. Each beam/rod is oriented in different direction, therefore the local coordinate system is different from the inertial coordinate system. The effective forces on each beam/rod are expressed using its local coordinate system. When formulating the equations of motion, we will need to express all the effective forces in the same coordinate system, i.e. the inertial coordinate system.

Each beam/rod is oriented at certain angle θ with respect to the axes in the inertial coordinate system, thus the local coordinate systems are rotated. When calculating the effective force on each rod, one may need to express them in the inertial coordinate system to establish the equilibrium equations. For this purpose, the local coordinate systems for the six beams/rods are all expressed in terms of the inertial coordinate system in this section. Note that we only need to transform the first three rows for the vectors which denote displacements, and only transform the last three rows for the vectors which denote bending components. The coordinate transformation are provided in detail as follows.

Fod $\mathbf{a}_0 - \mathbf{a}_1$, its coordinate system is the same as the inertial coordinate system, we have

$$R(\theta)_{[1]} = \begin{bmatrix} 1 & 0 & 0 \\ 0 & 1 & 0 \\ 0 & 0 & 1 \end{bmatrix}, \tag{A.1}$$

which lead to $\mathbf{e}_{1[1]} = \mathbf{e}_1$, $\mathbf{e}_{2[1]} = \mathbf{e}_2$, $\mathbf{e}_{3[1]} = \mathbf{e}_3$, $\mathbf{e}^b_{1[1]} = \mathbf{e}^b_1$, $\mathbf{e}^b_{2[1]} = \mathbf{e}^b_2$, $\mathbf{e}^b_{3[1]} = \mathbf{e}^b_3$.

For a beam/rod $\mathbf{a}_0 - \mathbf{a}_2$, the new coordinate system $x\prime - y\prime - z\prime$ can be viewed as rotating counterclockwise with an angle of 180° around z-axis, then rotating with an angle of 270°

around $x\prime$-axis such that

$$R(\theta)_{[2]} = \begin{bmatrix} 1 & 0 & 0 \\ 0 & \cos(\frac{3\pi}{2}) & \sin(\frac{3\pi}{2}) \\ 0 & -\sin(\frac{3\pi}{2}) & \cos(\frac{3\pi}{2}) \end{bmatrix} \begin{bmatrix} \cos(\pi) & \sin(\pi) & 0 \\ -\sin(\pi) & \cos(\pi) & 0 \\ 0 & 0 & 1 \end{bmatrix} = \begin{bmatrix} -1 & 0 & 0 \\ 0 & 0 & -1 \\ 0 & -1 & 0 \end{bmatrix}. \tag{A.2}$$

Applying Eq. A.2 and Eq. 2.2, we obtain $\mathbf{e}_{1[2]} = (-1\ 0\ 0\ 0\ 0\ 0)^T$, $\mathbf{e}_{2[2]} = (0\ 0\ -1\ 0\ 0\ 0)^T$, $\mathbf{e}_{3[2]} = (0\ -1\ 0\ 0\ 0\ 0)^T$, $\mathbf{e}^b_{1[2]} = (0\ 0\ 0\ -1\ 0\ 0)^T$, $\mathbf{e}^b_{2[2]} = (0\ 0\ 0\ 0\ 0\ -1)^T$ and $\mathbf{e}^b_{3[2]} = (0\ 0\ 0\ 0\ -1\ 0)^T$, which can be written as $\mathbf{e}_{1[2]} = -\mathbf{e}_1$, $\mathbf{e}_{2[2]} = -\mathbf{e}_3$, $\mathbf{e}_{3[2]} = -\mathbf{e}_2$, $\mathbf{e}^b_{1[2]} = -\mathbf{e}^b_1$, $\mathbf{e}^b_{2[2]} = -\mathbf{e}^b_3$ and $\mathbf{e}^b_{3[2]} = -\mathbf{e}^b_2$ for convenience. Note that for beams/rods in the same direction, the forces should be balanced.

The derivation of the remaining transformations follow similar procedures. For a beam/rod $\mathbf{a}_0 - \mathbf{a}_3$, we have

$$R(\theta)_{[3]} = \begin{bmatrix} \cos(\frac{\pi}{2}) & \sin(\frac{\pi}{2}) & 0 \\ -\sin(\frac{\pi}{2}) & \cos(\frac{\pi}{2}) & 0 \\ 0 & 0 & 1 \end{bmatrix} = \begin{bmatrix} 0 & 1 & 0 \\ -1 & 0 & 0 \\ 0 & 0 & 1 \end{bmatrix}, \tag{A.3}$$

thus $\mathbf{e}_{1[3]} = \mathbf{e}_2$, $\mathbf{e}_{2[3]} = -\mathbf{e}_1$, $\mathbf{e}_{3[3]} = \mathbf{e}_3$, $\mathbf{e}^b_{1[3]} = \mathbf{e}^b_2$, $\mathbf{e}^b_{2[3]} = -\mathbf{e}^b_1$ and $\mathbf{e}^b_{3[3]} = \mathbf{e}^b_3$.

For rod $\mathbf{a}_0 - \mathbf{a}_4$, we have

$$R(\theta)_{[4]} = \begin{bmatrix} 1 & 0 & 0 \\ 0 & \cos(\frac{3\pi}{2}) & \sin(\frac{3\pi}{2}) \\ 0 & -\sin(\frac{3\pi}{2}) & \cos(\frac{3\pi}{2}) \end{bmatrix} \begin{bmatrix} \cos(\frac{3\pi}{2}) & \sin(\frac{3\pi}{2}) & 0 \\ -\sin(\frac{3\pi}{2}) & \cos(\frac{3\pi}{2}) & 0 \\ 0 & 0 & 1 \end{bmatrix} = \begin{bmatrix} 0 & -1 & 0 \\ 0 & 0 & -1 \\ 1 & 0 & 0 \end{bmatrix}, \tag{A.4}$$

thus $\mathbf{e}_{1[4]} = -\mathbf{e}_2$, $\mathbf{e}_{2[4]} = -\mathbf{e}_3$, $\mathbf{e}_{3[4]} = \mathbf{e}_1$, $\mathbf{e}^b_{1[4]} = -\mathbf{e}^b_2$, $\mathbf{e}^b_{2[4]} = -\mathbf{e}^b_3$ and $\mathbf{e}^b_{3[4]} = \mathbf{e}^b_1$.

For rod $\mathbf{a}_0 - \mathbf{a}_5$, we have

$$R(\theta)_{[5]} = \begin{bmatrix} \cos(\frac{3\pi}{2}) & 0 & -\sin(\frac{3\pi}{2}) \\ 0 & 1 & 0 \\ \sin(\frac{3\pi}{2}) & 0 & \cos(\frac{3\pi}{2}) \end{bmatrix} = \begin{bmatrix} 0 & 0 & 1 \\ 0 & 1 & 0 \\ -1 & 0 & 0 \end{bmatrix}, \tag{A.5}$$

thus $\mathbf{e}_{1[5]} = \mathbf{e}_3$, $\mathbf{e}_{2[5]} = \mathbf{e}_2$, $\mathbf{e}_{3[5]} = -\mathbf{e}_1$, $\mathbf{e}^b_{1[5]} = \mathbf{e}^b_3$, $\mathbf{e}^b_{2[5]} = \mathbf{e}^b_2$ and $\mathbf{e}^b_{3[5]} = -\mathbf{e}^b_1$.

For rod $\mathbf{a}_0 - \mathbf{a}_6$, we have

$$R(\theta)_{[6]} = \begin{bmatrix} 1 & 0 & 0 \\ 0 & \cos(\frac{\pi}{2}) & \sin(\frac{\pi}{2}) \\ 0 & -\sin(\frac{\pi}{2}) & \cos(\frac{\pi}{2}) \end{bmatrix} \begin{bmatrix} \cos(\frac{\pi}{2}) & 0 & -\sin(\frac{\pi}{2}) \\ 0 & 1 & 0 \\ \sin(\frac{\pi}{2}) & 0 & \cos(\frac{\pi}{2}) \end{bmatrix} = \begin{bmatrix} 0 & 0 & -1 \\ 1 & 0 & 0 \\ 0 & -1 & 0 \end{bmatrix}, \tag{A.6}$$

thus $\mathbf{e}_{1[6]} = -\mathbf{e}_3$, $\mathbf{e}_{2[6]} = \mathbf{e}_1$, $\mathbf{e}_{3[6]} = -\mathbf{e}_2$, $\mathbf{e}^b_{1[6]} = -\mathbf{e}^b_3$, $\mathbf{e}^b_{2[6]} = \mathbf{e}^b_1$ and $\mathbf{e}^b_{3[6]} = -\mathbf{e}^b_2$.

These coordinate systems shall be applied in Eq. (2.30) in the derivation of effective forces on the beams/rods. Then the equations motion can be formulated and rewrote using matrices $\mathbf{J}$ and $\mathbf{L}$ as given below:

$$\mathbf{J}_j = \mathbf{e}_k \mathbf{e}_k^T, \quad k = \begin{cases} \dfrac{j+1}{2} & \text{if j is odd,} \\ \dfrac{j}{2} & \text{if j is even,} \end{cases} \tag{A.7}$$

$$\mathbf{L}_1 = \sum_{m=1,2,3,\ \ m\neq k} \mathbf{e}_m \mathbf{e}_m^T, \quad k = \begin{cases} \dfrac{j+1}{2} & \text{if j is odd,} \\ \dfrac{j}{2} & \text{if j is even,} \end{cases} \tag{A.8}$$

$$\mathbf{L}_2 = \sum_{m=4,5,6,\ \ m\neq k} \mathbf{e}_m \mathbf{e}_m^T, \quad k = \begin{cases} \dfrac{j+7}{2} & \text{if j is odd,} \\ \dfrac{j+6}{2} & \text{if j is even.} \end{cases} \tag{A.9}$$

$$\mathbf{L}_k = (-1)^j \times \begin{cases} -\mathbf{e}_2\mathbf{e}_6^T + \mathbf{e}_3\mathbf{e}_5^T + (-1)^{k+1}(\mathbf{e}_5\mathbf{e}_3^T - \mathbf{e}_6\mathbf{e}_2^T), & \text{j=1,2,} \\ \mathbf{e}_1\mathbf{e}_6^T - \mathbf{e}_3\mathbf{e}_4^T - (-1)^{k+1}(\mathbf{e}_4\mathbf{e}_3^T + \mathbf{e}_6\mathbf{e}_1^T), & \text{j=3,4, k=3,4,} \\ -\mathbf{e}_1\mathbf{e}_5^T + \mathbf{e}_2\mathbf{e}_4^T + (-1)^{k+1}(\mathbf{e}_4\mathbf{e}_2^T - \mathbf{e}_5\mathbf{e}_1^T), & \text{j=5,6.} \end{cases} \tag{A.10}$$

Appendix B

Unit circle to triangle mapping

Our objective here is to derive a transformation from the plane of a unit circle to the plane of the mapped triangle as shown in Fig. 5.1. The conjugate points $A = e^{-i\phi}$ and $B = e^{i\phi}$, $0 < \phi < \pi$, on the circle are symmetric with respect to the horizontal axis, but could be anywhere along the circumference.

We first map the interior of the unit circle to the upper half plane of the variable γ using a bilinear transformation

$$\gamma = i\Big(\frac{1-z}{1+z}\Big)\cot\frac{\phi}{2}. \tag{B.1}$$

Thus, the boundary of the circle is mapped to the real axis: $z = e^{i\theta} \Rightarrow \gamma = \tan(\theta/2)\cot(\phi/2)$, with the conjugate points A and B mapped to -1 and $+1$, respectively. The conformal mapping that takes the upper half of the γ-plane to the interior of the equilateral triangle in the t-plane such that the points A and B, of the original unit circle are mapped onto the vertices A and B is

$$t = P + Q\int_0^\gamma \frac{dx}{(1-x^2)^{2/3}} = P + Q\,G(\gamma) \tag{B.2}$$

where

$$G(\gamma) = {}_2F_1\big(\frac{1}{2}, \frac{2}{3}; \frac{3}{2}; \gamma^2\big)\,\gamma \tag{B.3}$$

and ${}_2F_1$ is the hypergeometric function. Placing the vertices A and B of the equilateral triangle at $(1 \pm i\sqrt{3})a/2$ yields the unknowns P and Q, so that

$$t = \Big(1 + i\sqrt{3}\frac{G(\gamma)}{G(1)}\Big)\frac{a}{2}. \tag{B.4}$$

Note that $G(1) = \frac{1}{2}\sqrt{\pi}\,\Gamma(\frac{1}{3})/\Gamma(\frac{5}{6}) = 2.10327\ldots$. The full mapping $z \to t(z)$ follows by combining Eqs. (B.1), (B.3) and (B.4).

References

[1] A. N. Norris and X. Su. Enhanced acoustic transmission through a slanted grating. *Comptes Rendus Mécanique*, 343(12):622–634, 2015.

[2] X. Su and A. N. Norris. Focusing, refraction, and asymmetric transmission of elastic waves in solid metamaterials with aligned parallel gaps. *J. Acoust. Soc. Am.*, 139(6):3386–3394, 2016.

[3] A. A. Kutsenko, A. J. Nagy, X. Su, A. L. Shuvalov, and A. N. Norris. Wave propagation and homogenization in 2D and 3D lattices: a semi-analytical approach. *Q. J. Mech. Appl. Math.* (to be published) arXiv:1703.03495.

[4] R. M. Walser. Metamaterials: What are they? what are they good for? In *APS, Annual March Meeting, March 20-24, 2000 Minneapolis, MN*, 2000.

[5] V. G. Veselago. The electrodynamics of substances with simultaneous negative values of ε and μ. *Soviet Physics Uspekhi*, 10:509–514, 1968.

[6] D. R. Smith, W. J. Padilla, D. C. Vier, S. C. Nemat-Nasser, and S. Schultz. Composite medium with simultaneously negative permeability and permittivity. *Phys. Rev. Lett.*, 84(18):4184–4187, 2000.

[7] R. A. Shelby. Experimental verification of a negative index of refraction. *Science*, 292(5514):77–79, 2001.

[8] J. B. Pendry. Negative refraction makes a perfect lens. *Phys. Rev. Lett.*, 85(18):3966–3969, 2000.

[9] J. Sánchez-Pérez, D. Caballero, R. Mártinez-Sala, C. Rubio, J. Sánchez-Dehesa, F. Meseguer, J. Llinares, and F. Gálvez. Sound attenuation by a two-dimensional array of rigid cylinders. *Phys. Rev. Lett.*, 80(24):5325–5328, 1998.

[10] Z. Liu, Z. Zhang, Y. Mao, Y. Y. Zhu, Z. Yang, C. T. Chan, and P. Sheng. Locally resonant sonic materials. *Science*, 289(5485):1734–1736, 2000.

[11] X. Zhang and Z. Liu. Negative refraction of acoustic waves in two-dimensional phononic crystals. *Appl. Phys. Lett.*, 85(2):341, 2004.

[12] L. Feng, X.-P. Liu, M.-H. Lu, Y.-B. Chen, Y.-W. Mao Y.-F. Chen, J. Zi, Y.-Y. Zhu, S.-N. Zhu, and N.-B. Ming. Refraction control of acoustic waves in a square-rod-constructed tunable sonic crystal. *Phys. Rev. B*, 73:193101, 2006.

[13] M. Ke, Z. Liu, P. Pang, C. Qiu, D. Zhao, S. Peng, J. Shi, and W. Wen. Experimental demonstration of directional acoustic radiation based on two-dimensional phononic crystal band edge states. *Appl. Phys. Lett.*, 90(8):083509, 2007.

[14] S.-C. S. Lin, T. J. Huang, J.-H. Sun, and T.-T. Wu. Gradient-index phononic crystals. *Phys. Rev. B*, 79:094302, 2009.

[15] X. Li, X. Ni, L. Feng, M. Lu, C. He, and Y. Chen. Tunable unidirectional sound propagation through a sonic-crystal-based acoustic diode. *Phys. Rev. Lett.*, 106(8), 2011.

[16] A.-C. Hladky-Hennion, J. O. Vasseur, G. Haw, C. Croënne, L. Haumesser, and A. N. Norris. Negative refraction of acoustic waves using a foam-like metallic structure. *Appl. Phys. Lett.*, 102(14):144103, 2013.

[17] N. Fang, D. Xi, J. Xu, M. Ambati, W. Srituravanich, C. Sun, and X. Zhang. Ultrasonic metamaterials with negative modulus. *Nat. Mater.*, 5(6):452–456, 2006.

[18] Z. Yang, J. Mei, M. Yang, N. H. Chan, and P. Sheng. Membrane-type acoustic metamaterial with negative dynamic mass. *Phys. Rev. Lett.*, 101(20), 2008.

[19] S. H. Lee, C. M. Park, Y. M. Seo, Z. G. Wang, and C. K. Kim. Acoustic metamaterial with negative modulus. *J. Phys.: Condens. Matter*, 21(17):175704, 2009.

[20] S. Hy. Lee, C. M. Park, Y. M. Seo, Z. G. Wang, and C. K. Kim. Composite acoustic medium with simultaneously negative density and modulus. *Phys. Rev. Lett.*, 104(5), 2010.

[21] J. Christensen, Z. Liang, and M. Willatzen. Metadevices for the confinement of sound and broadband double-negativity behavior. *Phys. Rev. B*, 88(10), 2013.

[22] J. B. Pendry, D. Schurig, and D. R. Smith. Controlling electromagnetic fields. *Science*, 312(5781):1780–1782, 2006.

[23] M. Schmiele, V. S. Varma, C. Rockstuhl, and F. Lederer. Designing optical elements from isotropic materials by using transformation optics. *Phys. Rev. A.*, 81:033837, 2010.

[24] H. Chen and C. T. Chan. Transformation media that rotate electromagnetic fields. *Appl. Phys. Lett.*, 90(24), 2007.

[25] M. Rahm, D. Schurig, D. A. Roberts, S. A. Cummer, D. R. Smith, and J. B. Pendry. Design of electromagnetic cloaks and concentrators using form-invariant coordinate transformations of Maxwell's equations. In *Photonics and Nanostructures - Fundamentals and Applications*, volume 6, pages 87–95, 2008. The Seventh International Symposium on Photonic and Electromagnetic Crystal Structures PECS-VII.

[26] M.Rahm, S. A. Cummer, D. Schurig, J. B. Pendry, and D. R. Smith. Optical design of reflectionless complex media by finite embedded coordinate transformations. *Phys. Rev. Lett.*, 100:063903, 2008.

[27] S. A. Cummer and D. Schurig. One path to acoustic cloaking. *New J. Phys.*, 9(3):45, 2007.

[28] H. Chen and C. T. Chan. Acoustic cloaking in three dimensions using acoustic metamaterials. *Appl. Phys. Lett.*, 91(18):183518, 2007.

[29] A. N. Norris. Acoustic cloaking theory. *Proc. R. Soc. A*, 464:2411–2434, 2008.

[30] G. W. Milton and A. V. Cherkaev. Which elasticity tensors are realizable? *J. Eng. Mat. Tech.*, 117(4):483–493, 1995.

[31] R. Liu, C. Ji, J. J. Mock, J. Y. Chin, T. J. Cui, and D. R. Smith. Broadband ground-plane cloak. *Science*, 323(5912):366–369, 2009.

[32] B. I. Popa, L. Zigoneanu, and S. A. Cummer. Experimental acoustic ground cloak in air. *Phys. Rev. Lett.*, 106:253901, 2011.

[33] C. N. Layman, T. P. Martin, K. M. Moore, D. C. Calvo, and G. J. Orris. Designing acoustic transformation devices using fluid homogenization of an elastic substructure. *Appl. Phys. Lett.*, 99:163503, 2011.

[34] A. S. Titovich, A.N. Norris, and M. R. Haberman. A high transmission broadband gradient index lens using elastic shell acoustic metamaterial elements. *J. Acoust. Soc. Am.*, 139:3357–3364, 2016.

[35] Y. Li, J. Tu, B. Liang, X. Guo, D. Zhang, and J. Cheng. Unidirectional acoustic transmission based on source pattern reconstruction. *J. Appl. Phys.*, 112(6):064504, 2012.

[36] Y. Li, B. Liang, Z. Gu, X. Zou, and J. Cheng. Unidirectional acoustic transmission through a prism with near-zero refractive index. *Appl. Phys. Lett.*, 103(5):053505, 2013.

[37] Y. Zhu, X. Zou, B. Liang, and J. Cheng. Broadband unidirectional transmission of sound in unblocked channel. *Appl. Phys. Lett.*, 106(17):173508, 2015.

[38] B.-I. Popa and S. A. Cummer. Non-reciprocal and highly nonlinear active acoustic metamaterials. *Nat. Comm.*, 5, 2014.

[39] R. Fleury, D. L. Sounas, C. F. Sieck, M. R. Haberman, and A. Alù. Sound isolation and giant linear nonreciprocity in a compact acoustic circulator. *Science*, 343(6170):516–519, 2014.

[40] R. Fleury, D. Sounas, M. R. Haberman, and A. Alù. Nonreciprocal acoustics. *Acoustics Today*, 11(3):14–21, 2015.

[41] C. L. Kane and T. C. Lubensky. Topological boundary modes in isostatic lattices. *Nat. Phys.*, 10(1):39–45, 2013.

[42] Z. Yang, F. Gao, X. Shi, X. Lin, Z. Gao, Y. Chong, and B. Zhang. Topological acoustics. *Phys. Rev. Lett.*, 114(11), 2015.

[43] A. B. Khanikaev, R. Fleury, S. H. Mousavi, and A. Alù. Topologically robust sound propagation in an angular-momentum-biased graphene-like resonator lattice. *Nat. Comm.*, 6:8260, 2015.

[44] S. Hossein Mousavi, Alexander B. Khanikaev, and Zheng Wang. Topologically protected elastic waves in phononic metamaterials. *Nat. Comm.*, 6:8682, 2015.

[45] Z. Yang, H. Dai, N. Chan, G. Ma, and P. Sheng. Acoustic metamaterial panels for sound attenuation in the 50-1000 Hz regime. *Appl. Phys. Lett.*, 96(4):041906, 2010.

[46] J. Mei, G. Ma, M. Yang, Z. Yang, W. Wen, and P. Sheng. Dark acoustic metamaterials as super absorbers for low-frequency sound. *Nat. Comm.*, 3:756, 2012.

[47] G. Ma, M. Yang, S. Xiao, Z. Yang, and P. Sheng. Acoustic metasurface with hybrid resonances. *Nat. Mater.*, 13(9):873–878, 2014.

[48] A. Climente, D. Torrent, and J. Sanchez-Dehesa. Sound focusing by gradient index sonic lenses. *Appl. Phys. Lett.*, 97(10):104103, 2010.

[49] M. Farhat, S. Guenneau, and S. Enoch. Ultrabroadband elastic cloaking in thin plates. *Phys. Rev. Lett.*, 103(2):024301, 2009.

[50] N. Stenger, M. Wilhelm, and M. Wegener. Experiments on elastic cloaking in thin plates. *Phys. Rev. Lett.*, 108(1):014301, 2012.

[51] M. Farhat, S. Guenneau, S. Enoch, A. B. Movchan, and G. G. Petursson. Focussing bending waves via negative refraction in perforated thin plates. *Appl. Phys. Lett.*, 96(8):081909, 2010.

[52] M. Dubois, M. Farhat, E. Bossy, S. Enoch, S. Guenneau, and P. Sebbah. Flat lens for pulse focusing of elastic waves in thin plates. *Appl. Phys. Lett.*, 103(7):071915, 2013.

[53] M. Farhat, P.-Y. Chen, H. Bagci, S. Enoch, S. Guenneau, and A. Alù. Platonic scattering cancellation for bending waves in a thin plate. *Sci. Rep.*, 4:4644, 2014.

[54] P. G. Martinsson and A. B. Movchan. Vibrations of lattice structures and phononic band gaps. *Q. J. Mech. Appl. Math.*, 56(1):45–64, 2003.

[55] A. S. Phani, J. Woodhouse, and N. A. Fleck. Wave propagation in two-dimensional periodic lattices. *J. Acoust. Soc. Am.*, 119(4):1995–2005, 2006.

[56] S. Gonella and M. Ruzzene. Analysis of in-plane wave propagation in hexagonal and re-entrant lattices. *J. Sound. Vib.*, 312(1-2):125–139, 2008.

[57] A. Spadoni, M. Ruzzene, S. Gonella, and F. Scarpa. Phononic properties of hexagonal chiral lattices. *Wave Motion*, 46(7):435–450, 2009.

[58] M. J. Leamy. Exact wave-based Bloch analysis procedure for investigating wave propagation in two-dimensional periodic lattices. *J. Sound. Vib.*, 331(7):1580–1596, 2012.

[59] P. G. Martinsson and I. Babuška. Homogenization of materials with periodic truss or frame micro-structures. *Math. Models Methods Appl. Sci.*, 17(5):805–832, 2007.

[60] S. Gonella and M. Ruzzene. Homogenization and equivalent in-plane properties of two-dimensional periodic lattices. *Int. J. Solids Struct.*, 45(10):2897–2915, 2008.

[61] D. J. Colquitt, I. S. Jones, N. V. Movchan, and A. B. Movchan. Dispersion and localization of elastic waves in materials with microstructure. *Proc. R. Soc. A*, 467(2134):2874–2895, 2011.

[62] D. J. Colquitt, M. J. Nieves, I. S. Jones, N. V. Movchan, and A. B. Movchan. Localisation for a line defect in an infinite square lattice. *Proc. R. Soc. A*, 469(2150):20120579, 2013.

[63] M. J. P. Musgrave. *Crystal Acoustics*. Acoustical Society of America, New York, 2003.

[64] W. E. Warren and A. M. Kraynik. The linear elastic properties of open-cell foams. *J. Appl. Mech. ASME*, 55(2):341–346, 1988.

[65] A. N. Norris. Mechanics of elastic networks. *Proc. R. Soc. A*, 470:20140522, 2014.

[66] Y. Xie, W. Wang, H. Chen, A. Konneker, B.-I. Popa, and S. A. Cummer. Wavefront modulation and subwavelength diffractive acoustics with an acoustic metasurface. *Nat. Comm.*, 5:5553, 2014.

[67] Y. Li, X. Jiang, B. Liang, J. Cheng, and L. Zhang. Metascreen-based acoustic passive phased array. *Phys. Rev. Appl*, 4(2), 2015.

[68] Y. Li, B. Liang, X. Tao, X. Zhu, X. Zou, and J. Cheng. Acoustic focusing by coiling up space. *Appl. Phys. Lett.*, 101(23):233508, 2012.

[69] K. Tang, C. Qiu, J. Lu, M. Ke, and Z. Liu. Focusing and directional beaming effects of airborne sound through a planar lens with zigzag slits. *J. Appl. Phys.*, 117(2):024503, 2015.

[70] M. Moleron, M. Serra-Garcia, and C. Daraio. Acoustic fresnel lenses with extraordinary transmission. *Appl. Phys. Lett.*, 105(11):114109, 2014.

[71] Y. Xie, B.-I. Popa, L. Zigoneanu, and S. A. Cummer. Measurement of a broadband negative index with space-coiling acoustic metamaterials. *Phys. Rev. Lett.*, 110(17), 2013.

[72] M. Lu, X. Liu, L. Feng, J. Li, C. Huang, Y. Chen, Y. Zhu, S. Zhu, and N. Ming. Extraordinary acoustic transmission through a 1d grating with very narrow apertures. *Phys. Rev. Lett.*, 99(17):174301, 2007.

[73] A. Alù, G. D'Aguanno, N. Mattiucci, and M. J. Bloemer. Plasmonic brewster angle: Broadband extraordinary transmission through optical gratings. *Phys. Rev. Lett.*, 106(12), 2011.

[74] C. Argyropoulos, G. D'Aguanno, N. Mattiucci, N. Akozbek, M. J. Bloemer, and A. Alù. Matching and funneling light at the plasmonic brewster angle. *Phys. Rev. B*, 85(2), 2012.

[75] G. D'Aguanno, K. Q. Le, R. Trimm, A. Alù, N. Mattiucci, A. D. Mathias, N. Aközbek, and M. J. Bloemer. Broadband metamaterial for nonresonant matching of acoustic waves. *Sci. Rep.*, 2, March 2012.

[76] A. Maurel, S. Félix, and J.F. Mercier. Enhanced transmission through gratings: Structural and geometrical effects. *Phys. Rev. B*, 88(11), 2013.

[77] A. N. Norris and A. L. Shuvalov. Wave impedance matrices for cylindrically anisotropic radially inhomogeneous elastic materials. *Q. J. Mech. Appl. Math.*, 63:1–35, 2010.

[78] Y. Li, G. Yu, B. Liang, X. Zou, G. Li, S. Cheng, and J. Cheng. Three-dimensional ultrathin planar lenses by acoustic metamaterials. *Sci. Rep.*, 4:6830, 2014.

[79] W. Wang, Y. Xie, A. Konneker, B.-I. Popa, and S. A. Cummer. Design and demonstration of broadband thin planar diffractive acoustic lenses. *Appl. Phys. Lett.*, 105(10):101904, 2014.

[80] N. M. Estakhri and A. Alù. Wave-front transformation with gradient metasurfaces. *Phys. Rev. X*, 6(4), 2016.

[81] Y. Li, S. Qi, and M. B. Assouar. Theory of metascreen-based acoustic passive phased array. *New J. Phys.*, 18(4):043024, 2016.

[82] M. A. Biot. Theory of propagation of elastic waves in a fluid-saturated porous solid. I. low-frequency range. *J. Acoust. Soc. Am.*, 28(2):168, 1956.

[83] M. A. Biot. Mechanics of deformation and acoustic propagation in porous media. *J. Appl. Phys.*, 33(4):1482, 1962.

[84] C. Gomez-Reino, M. V. Perez, and C. Bao. *Gradient-Index Optics: Fundamentals and Applications*. Springer, New York, 2002.

[85] L. Zigoneanu, B.-I. Popa, and S. A. Cummer. Design and measurements of a broadband two-dimensional acoustic lens. *Phys. Rev. B*, 84(2), 2011.

[86] V. Romero-García, A. Cebrecos, R. Picó, V. J. Sánchez-Morcillo, L. M. Garcia-Raffi, and J. V. Sánchez-Pérez. Wave focusing using symmetry matching in axisymmetric acoustic gradient index lenses. *Appl. Phys. Lett.*, 103(26):264106, 2013.

[87] C. M. Park, C. H. Kim, H. T. Park, and S. H. Lee. Acoustic gradient-index lens using orifice-type metamaterial unit cells. *Appl. Phys. Lett.*, 108(12):124101, 2016.

[88] T.P. Martin, M. Nicholas, G. J. Orris, L-W Cai, and D. Torrent. Sonic gradient index lens for aqueous applications. *Appl. Phys. Lett.*, 97:113503, 2010.

[89] T. P. Martin, C. J. Naify, E. A. Skerritt, C. N. Layman, M. Nicholas, D. C. Calvo, G. J. Orris, D. Torrent, and J. Sanchez-Dehesa. Transparent gradient-index lens for underwater sound based on phase advance. *Phys. Rev. Appl.*, 4(3), 2015.

[90] A.N. Norris and A.J. Nagy. Metal Water: A metamaterial for acoustic cloaking. In *Proceedings of Phononics 2011, Santa Fe, NM, USA, May 29-June 2*, pages 112–113, Paper Phononics–2011–0037, 2011.

[91] C. N. Layman, C. J. Naify, T. P. Martin, D. C. Calvo, and G. J. Orris. Highly-anisotropic elements for acoustic pentamode applications. *Phys. Rev. Lett.*, 111:024302–024306, 2013.

[92] Y. Chen, X. Liu, and G. Hu. Latticed pentamode acoustic cloak. *Sci. Rep.*, 5:15745, 2015.

[93] B. Hassani and E. Hinton. A review of homogenization and topology optimization I-homogenization theory for media with periodic structure. *Comp. Struct.*, 69(6):707–717, 1998.

[94] A. N. Norris. Mechanics of elastic networks. *Proc. R. Soc. A*, 470(2172):20140522, 2014.

[95] H. S. Kim and S. T. S. Al-Hassani. A morphological elastic model of general hexagonal columnar structures. *Int. J. Mech. Sc.*, 43(4):1027–1060, 2001.

[96] X. Cai, L. Wang, Z. Zhao, A. Zhao, X. Zhang, T. Wu, and H. Chen. The mechanical and acoustic properties of two-dimensional pentamode metamaterials with different structural parameters. *Appl. Phys. Lett.*, 109(13):131904, 2016.

[97] R. Fleury and A. Alù. Cloaking and invisibility: A review. *Forum for Electromagnetic Research Methods and Application Technologies (FERMAT)*, 2013.

[98] A. N. Norris. Acoustic cloaking. *Acoustics Today*, 11(1):38–46, 2015.

[99] C. Ren, Z. Xiang, and Z. Cen. Design of acoustic devices with isotropic material via conformal transformation. *Appl. Phys. Lett.*, 97(4):044101, 2010.

[100] A. S. Titovich and A. N. Norris. Tunable cylindrical shell as an element in acoustic metamaterial. *J. Acoust. Soc. Am.*, 136(4):1601–1609, 2014.

[101] T. Bückmann, M. Thiel, M. Kadic, R. Schittny, and M. Wegener. An elasto-mechanical unfeelability cloak made of pentamode metamaterials. *Nat. Comm.*, 5:4130, 2014.

[102] A. S. Titovich and A. N. Norris. Acoustic scattering from an infinitely long cylindrical shell with an internal mass attached by multiple axisymmetrically distributed stiffeners. *J. Sound. Vib.*, 228:134–153, 2015.

[103] T. P. Martin, C. N. Layman, K. M. Moore, and G. J. Orris. Elastic shells with high-contrast material properties as acoustic metamaterial components. *Phys. Rev. B*, 85(16):161103, 2012.

[104] X. Zhou, M. B. Assouar, and M. Oudich. Acoustic superfocusing by solid phononic crystals. *Appl. Phys. Lett.*, 105(23):233506, 2014.

[105] C. A. Rohde, T. P. Martin, M. D. Guild, C. N. Layman, C. J. Naify, M. Nicholas, A. L. Thangawng, D. C. Calvo, and G. J. Orris. Experimental demonstration of underwater acoustic scattering cancellation. *Sci. Rep.*, 5:13175, 2015.

[106] A. N. Norris. Comment on "Design of acoustic devices with isotropic material via conformal transformation" [Appl. Phys. Lett. 97, 044101 (2010)]. *Appl. Phys. Lett.*, 100:066101, 2012.

[107] G. S. Kino. *Acoustic Waves: Devices, Imaging, and Analog Signal Processing.* Prentice Hall, 1987.

[108] A. S. Titovich. *Acoustic and elastic waves in metamaterials for underwater applications.* PhD thesis, Rutgers University, 2015.

[109] A. Climente, D. Torrent, and J. Sanchez-Dehesa. Gradient index lenses for flexural waves based on thickness variations. *Appl. Phys. Lett.*, 105(6):064101, 2014.

[110] B. Morvan, A. Tinel, A.-C. Hladky-Hennion, J. Vasseur, and B. Dubus. Experimental demonstration of the negative refraction of a transverse elastic wave in a two-dimensional solid phononic crystal. *Appl. Phys. Lett.*, 96(10):101905, 2010.

[111] J. Pierre, O. Boyko, L. Belliard, J. O. Vasseur, and B. Bonello. Negative refraction of zero order flexural lamb waves through a two-dimensional phononic crystal. *Appl. Phys. Lett.*, 97(12):121919, 2010.

[112] R. Zhu, X. N. Liu, G. K. Hu, C. T. Sun, and G. L. Huang. Negative refraction of elastic waves at the deep-subwavelength scale in a single-phase metamaterial. *Nat. Comm.*, 5:5510, 2014.

[113] Z. Chang, H. Guo, B. Li, and X. Feng. Disentangling longitudinal and shear elastic waves by neo-hookean soft devices. *Appl. Phys. Lett.*, 106(16):161903, 2015.

[114] X. Zhu, X. Zou, B. Liang, and J. Cheng. One-way mode transmission in one-dimensional phononic crystal plates. *J. Appl. Phys.*, 108(12):124909, 2010.

[115] A. Spadoni and C. Daraio. Generation and control of sound bullets with a nonlinear acoustic lens. *Proc. Nat. Acad. Sci.*, 107(16):7230–7234, 2010.

[116] J. D. Achenbach. *Wave Propagation in Elastic Solids.* North Holland, 1987.

[117] N. Yu, P. Genevet, M. A. Kats, F. Aieta, J.-P. Tetienne, F. Capasso, and Z. Gaburro. Light propagation with phase discontinuities: Generalized laws of reflection and refraction. *Science*, 334(6054):333–337, 2011.

[118] C. Shen, Y. Xie, J. Li, S. A. Cummer, and Y. Jing. Asymmetric acoustic transmission through near-zero-index and gradient-index metasurfaces. *Appl. Phys. Lett.*, 108(22):223502, 2016.

[119] H. Zhu and F. Semperlotti. Anomalous refraction of acoustic guided waves in solids with geometrically tapered metasurfaces. *Phys. Rev. Lett.*, 117(3), 2016.

[120] K. F. Graff. *Wave Motion in Elastic Solids.* Dover, New York, 1991.

[121] M. A. Biot. Theory of elasticity and consolidation for a porous anisotropic solid. *J. Appl. Phys.*, 26(2):182–185, 1955.

[122] M. A. Biot. Theory of propagation of elastic waves in a fluid-saturated porous solid. II. higher frequency range. *J. Acoust. Soc. Am.*, 28(2):179–191, 1956.

[123] T. J. Plona. Observation of a second bulk compressional wave in a porous medium at ultrasonic frequencies. *Appl. Phys. Lett.*, 36(4):259–261, 1980.

[124] D. L. Johnson, T. J. Plona, C. Scala, F. Pasierb, and H. Kojima. Tortuosity and acoustic slow waves. *Phys. Rev. Lett.*, 49(25):1840–1844, 1982.

[125] J.G. Berryman and H.F. Wang. Elastic wave propagation and attenuation in a double-porosity dual-permeability medium. *Int. J. Rock Mech. Min. Sci.*, 37(1-2):63–78, 2000.

[126] I. A. Beresnev. Compressional-wave propagation in porous media saturated with two fluids. *Geophysics*, 79(1):L1–L11, 2014.

[127] A. E. H. Love. *Treatise on the Mathematical Theory of Elasticity.* Dover, New York, 1944.

[128] M. A. Biot and D. G. Willis. The elastic coefficients of the theory of consolidation. *J. Appl. Mech., ASME*, (24):594–601, 1957.

[129] S. Feng and D. L. Johnson. High-frequency acoustic properties of a fluid/porous solid interface. I. new surface mode. *J. Acoust. Soc. Am.*, 74(3):906–914, 1983.

[130] A. H. Schoen. Infinite periodic minimal surfaces without self-intersections. Technical Report TN D-5541, NASA, 1970.

[131] H.-Y. Chen, Y. Kwon, and K. Thornton. Multifunctionality of three-dimensional self-assembled composite structure. *Scr. Mater.*, 61(1):52–55, 2009.

[132] H. Lamb. On the propagation of tremors over the surface of an elastic solid. *Philosophical Transactions of the Royal Society A: Mathematical, Physical and Engineering Sciences*, 203(359-371):1–42, 1904.